

ISSN en trámite



Geofísica Internacional

Revista Trimestral Publicada por el Instituto de Geofísica de la
Universidad Nacional Autónoma de México



México

Volume 61 Number 1
January - March
2022

— Geofísica Internacional —

Dr. José Luis Macías Vázquez
Director of Instituto de Geofísica

Dr. Arturo Iglesias Mendoza
President of Unión Geofísica Mexicana

Editor Chief

Dr. Servando De la Cruz-Reyna
Instituto de Geofísica, UNAM
sdelacrr@geofisica.unam.mx

Technical Editor

Mtra. Andrea Rostan Robledo
Instituto de Geofísica, UNAM
arostan@igeofisica.unam.mx

Editorial Board

Donald Bruce Dingwell
Earth and Environment
Ludwig Maximilian University of Munich,
Germany

Eric Desmond Barton
Departamento de Oceanografía
Instituto de Investigaciones Marinas, Spain

Jorge Clavero
Amawta Consultores, Chile

Gerhardt Jentzsch
Institut für Geowissenschaften
Friedrich-Schiller-Universität Jena, Germany

Peter Malischewsky
Institut für Geowissenschaften
Friedrich-Schiller-Universität Jena, Germany

François Michaud
Géosciences Azur
Université Pierre et Marie Curie, France

Olga Borisovna Popovicheva
Scobeltzine Institute of Nuclear Physics
Moscow State University, Rusia

Jaime Pous
Facultad de Geología
Universidad de Barcelona, Spain

Joaquín Rui
UA Science
University of Arizona, United States

Angelos Vourlidas
Solar Physics Branch
NASA Goddard Space Flight Center, United States

Théophile Ndougsa Mbarga
Department of Physics
University of Yaounde I, Cameroon

Associate Editors
José Agustín García Reynoso
Atmospheric Science Centro de Ciencias de la
Atmósfera UNAM, Mexico

Tereza Cavazos
Atmospheric Science
Departamento de Oceanografía Física CICESE,
Mexico

Dante Jaime Morán-Zenteno
Geochemistry
Instituto de Geología, UNAM, Mexico

Margarita López
Geochemistry
Instituto de Geología UNAM, Mexico

Avto Gogichaisvili
Geomagnetism And Paleomagnetism
Instituto de Geofísica UNAM, Mexico

Jaime Urrutia-Fucugauchi
Geomagnetism And Paleomagnetism
Instituto de Geofísica, UNAM, Mexico

Felipe I. Arreguín Cortés
Hydrology
Instituto Mexicano de Tecnología del Agua IMTA,
Mexico

William Lee Bandy
Marine Geology And Geophysics
Instituto de Geofísica UNAM, Mexico

Fabian García-Nocetti
Mathematical And Computational
Modeling
Instituto de Investigaciones en Matemáticas
Aplicadas y en Sistemas UNAM, Mexico

Graciela Herrera-Zamarrón
Mathematical Modeling
Instituto de Geofísica, UNAM, Mexico

Ismael Herrera Revilla
Mathematical And Computational
Modeling
Instituto de Geofísica UNAM, Mexico

Rene Chávez Segura
Near-Surface Geophysics
Instituto de Geofísica UNAM, Mexico

Juan García-Abdeslem
Near-Surface Geophysics
División de Ciencias de la Tierra CICESE, Mexico

Alec Torres-Freyermuth
Oceanography
Instituto de Ingeniería, UNAM, Mexico

Jorge Zavala Hidalgo
Oceanography
Centro de Ciencias de la Atmósfera UNAM,
Mexico

Shri Krishna Singh
Seismology
Instituto de Geofísica, UNAM, Mexico

Xyoli Pérez-Campos
Seismology
Servicio Sismológico Nacional, UNAM, Mexico

Blanca Mendoza Ortega
Space Physics
Centro de Ciencias de la Atmósfera, UNAM,
Mexico

Inez Staciari Batista
Space Physics
Pesquisador Senior Instituto Nacional de Pesquisas
Espaciais, Brazil

Roberto Carniel
Volcanology
Laboratorio di misure e trattamento dei segnali
DPIA - Università di Udine, Italy

Miguel Moctezuma-Flores
Satellite Geophysics
Facultad de Ingeniería, UNAM, Mexico

Assistance

Elizabeth Morales Hernández,
Management
eliedit@igeofisica.unam.mx



GEOFÍSICA INTERNACIONAL, Año 61, Vol. 61, Núm. 1, enero - marzo de 2022 es una publicación trimestral, editada por la Universidad Nacional Autónoma de México, Ciudad Universitaria, Alcaldía Coyoacán, C.P. 04150, Ciudad de México, a través del Instituto de Geofísica, Circuito de la Investigación Científica s/n, Ciudad Universitaria, Alcaldía Coyoacán, C.P. 04150, Ciudad de México, Tel. (55)56 22 41 15. URL: <http://revistagi.geofisica.unam.mx>, correo electrónico: revistagi@igeofisica.unam.mx. Editora responsable: Andrea Rostan Robledo. Certificado de Reserva de Derechos al uso Exclusivo del Título: 04-2022-081610251200-102, ISSN: en trámite, otorgados por el Instituto Nacional del Derecho de Autor (INDAUTOR). Responsable de la última actualización Saúl Armendáriz Sánchez, Editor Técnico. Fecha de la última modificación: 31 de diciembre 2021, Circuito de la Investigación Científica s/n, Ciudad Universitaria, Alcaldía Coyoacán, C.P. 04150, Ciudad de México.

El contenido de los artículos es responsabilidad de los autores y no refleja el punto de vista de los árbitros, del Editor o de la UNAM. Se autoriza la reproducción total o parcial de los textos siempre y cuando se cite la fuente completa y la dirección electrónica de la publicación.



Esta obra está bajo una Licencia Creative Commons Atribución-NoComercial-SinDerivadas 4.0 Internacional.

Contents

The 1815 Tambora eruption: Its significance to the understanding of large-explosion caldera formations

Izumi Yokoyama

5

Radioactive heat production characterization of Ar-Rassafeh Badyieh area (area-2), Syria by using aerial gamma ray spectrometric and fractal modeling techniques

Jamal Asfahani

20

Mineral lithotype identification on the andrill AND-2A drillcore, antarctica by using ternary mineral rock physics templates built from a self-consistent approach: Identificación de litotipos minerales

Jaime Meléndez Martínez, Rubén Nicolás López, Oscar C Valdiviezo

40

Complejación de metales por sustancias húmicas acuáticas como proceso natural, tomando como caso de estudio el Lago de Xochimilco, Ciudad de México, México

María de Jesús González-Guadarrama, Silvia Elena Castillo-Blum, María Aurora Armienta

55

Projection of land use to 2030 and its impacts on water availability in a brazilian sub-basin: A LCM and SWAT approach

Adriana Paulo de Sousa Oliveira, Rafaela Ribeiro Gracelli, Arthur Amaral e Silva, Vitor Justo dos Santos, Jackeline de Siqueira Castro, Maria Lúcia Calijuri

66

<https://doi.org/10.22201/igeof.00167169p.2022.61.1.2204>

THE 1815 TAMBORA ERUPTION: ITS SIGNIFICANCE TO THE UNDERSTANDING OF LARGE-EXPLOSION CALDERA FORMATIONS

Izumi Yokoyama^{1*}

Received: August 6, 2021; accepted: December 13, 2021; published on-line: January 1, 2022.

RESUMEN

Las calderas volcánicas, abundantes tanto en la Tierra como en la Luna, son de gran interés para los vulcanólogos, principalmente por sus grandes dimensiones y por los grandes volúmenes que emiten. En el presente trabajo se considera la dinámica de la formación de calderas por erupciones de muy alta explosividad por medio del análisis de como se produce el fracturamiento de la superficie terrestre por causa de actividad ígnea violenta. Esto lleva a la definición de la “*típica caldera de explosión*”, que es un prototipo de varias calderas formadas recientemente, en la escala histórica de tiempo. Existen tres ejemplos de ese tipo de calderas: Tambora (Sumbawa), Krakatau (Estrecho de Sunda) y Novarupta (Alaska). La caldera de Tambora es el mejor ejemplo bien documentado del origen de una típica caldera de explosión y que no ha producido erupciones importantes subsecuentes a su formación. La estructura subyacente a la caldera Tambora se discute y se compara con la de la caldera de Krakatau formada en 1883, la segunda erupción más grande en el tiempo histórico. De allí, en contraste con las calderas típicamente basálticas del “*tipo colapso*”, se define el “*tipo Tambora*” de caldera como una del “*tipo explosión*” de gran tamaño, que puede alcanzar diámetros de hasta 10 km. Este concepto de caldera tipo Tambora resulta útil para comprender y caracterizar la estructura y las componentes de otras grandes calderas del mundo. Grandes calderas de explosión completamente desarrolladas, tales como las calderas Aso y Aira en Kyushu, Japón se discuten y se interpretan a partir de datos geofísicos como calderas compuestas: En esas calderas se han producido grandes erupciones adyacentes produciendo emisiones masivas de productos piroclásticos y causando que sus estructuras originales alcanzaran anchuras en exceso de 10 km.

PALABRAS CLAVE: La erupción de Tambora de 1815, grandes erupciones explosivas, formación de calderas, grandes volúmenes emitidos, definición de caldera tipo Tambora, calderas compuestas, Calderas Aso y Aira.

*Corresponding author at iyokoyama@joy.ocn.ne.jp

The Japan Academy, Ueno Park, Tokyo, 110-0007, Japan.

ABSTRACT

Volcanic calderas, plentiful on the Earth and the moon, have been of much interest to volcanologists because of their large dimensions and extensive volumes of ejecta. Here, we consider the dynamics of caldera-forming by major explosive eruptions, examining how the breakdown of the earth's surface is caused by violent igneous activity. This leads to the definition of “*typical explosion caldera*”, which is a prototype of several newly-formed calderas in the historical timescale. There are three examples of such calderas: Tambora (Sumbawa), Krakatau (Sunda Straits), and Novarupta (Alaska). Tambora Caldera is the best example of a well-documented, recently formed typical explosion caldera, with no significant subsequent eruptions occurring after its formation. The subsurface structure of Tambora Caldera is discussed and compared to the 1883 eruption of Krakatau, the second largest eruption in historical times. Then, contrasting with the typically basaltic “*collapse-type*” calderas, a “*Tambora-caldera type*” is defined as a large “*explosion-type*” caldera, that may reach up to 10 km in diameter. The Tambora-type caldera concept is useful to qualify and understand the structure and components of other major calderas in the world. Fully developed larger explosion calderas such as Aso and Aira Calderas in Kyushu, Japan are discussed and explained as composite calderas based on geophysical data. Those calderas have repeatedly ejected massive pyroclastic products causing their original structures to grow wider than 10 km.

KEY WORDS: The 1815 Tambora eruption, Explosive eruption, Caldera formation, Large ejected volumes, Definition of Tambora-type calderas, Composite calderas and Aso and Aira calderas.

INTRODUCTION

1. IMPORTANCE OF THE TAMBORA 1815 ERUPTION IN THE HISTORY OF VOLCANOLOGY

Many volcanic calderas of different sizes and ages can be identified on Earth. However, their origins and structures may be different. It is thus important to determine the “caldera type” to define models that explains their formations, particularly for those resulting from major explosive eruptions. Calderas formed in the historical timescale are particularly important to understand and explain their complex structures, especially of those with large diameters. There are three explosive eruption calderas formed in historical times: Tambora in 1815; Krakatau in 1883; Novarupta in 1912. Their features have been discussed by Yokoyama (2016). From those, Tambora is the largest in diameter and ejecta volume. The caldera width could have been even larger than the present 6.7 km, but the power of the eruption was probably not sufficient to remove most of the original volcanic edifice overlaying the basement, a very large shield volcano. Moreover, no known calderas elsewhere formed by a single explosion exceed the dimensions of Tambora. Two important features of the Tambora Caldera formation eruption are discussed in the next.

2. THE TAMBORA CALDERA WAS FORMED IN A SINGLE ERUPTION IN 1815 AND NO FURTHER EXPLOSIVE ERUPTIONS HAVE OCCURRED.

It was reported that about 3 years before 1815, a dense cloud was observed near the summit of Tambora Volcano on Sumbawa Island (Fig. 1). Later, on 5 April 1815, thundering explosions were heard as far as Batavia (1250 km away). On 10 and 11 April, the eruption reached its paroxysm, and strong earthquakes were felt through the island of Java. On the night of 10 April, a small tsunami was observed at Sangar (Fig. 1). The activity after the caldera formation has remained at

a low level within the summit caldera as described below. The distribution of the fallout deposits from the paroxysm is shown in Fig. 1. However, a large volume of marine deposits resulted from massive pyroclastic flows. The volume estimations from marine deposits are imprecise and should be carefully reprised.

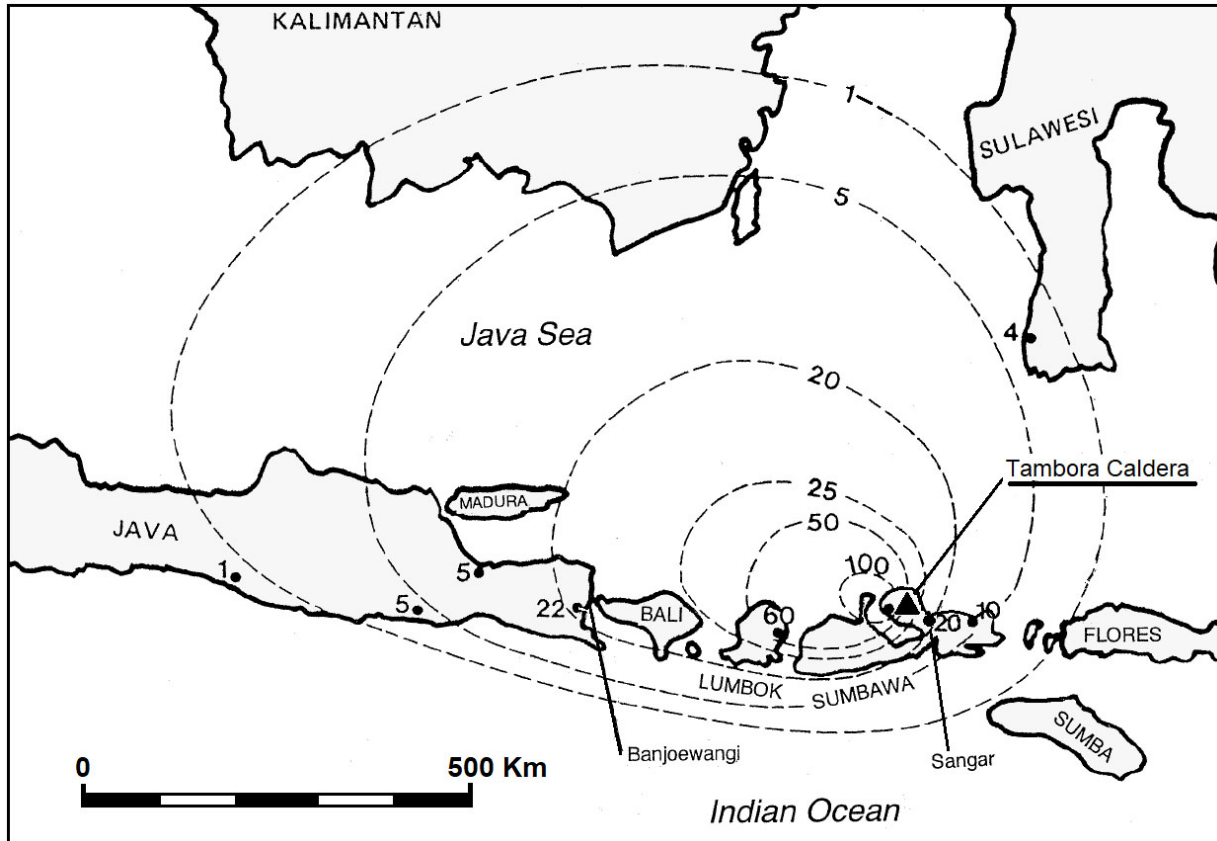


Figure 1. Location of Sumbawa Island and Tambora Volcano. Isopachs of tephra fallout in cm (after Self *et al.* 1984, and Sigurdsson and Carey, 1989)

There are no reports of volcano-related topographic deformations around the 1815 eruptions of Tambora despite its short distance to the sea, which is a suitable reference for leveling. This probably resulted from the lack of adequate measuring devices in the region and the confusion in the area at that time, otherwise, the depth of the magma reservoir could have been estimated. According to Petroschevsky (1949) and Sigurdsson and Carey (1989), in addition to the heard explosions, earthquakes related to the eruption were felt at distances between 400 and 600 km from the volcano. According to Gutenberg and Richter (1956), the maximum distance of seismic perceptibility R (km) is related to the local magnitude M_L as:

$$M_L = 3.8 \log R - 3.0$$

Then, we get a possible M_L magnitude for the largest Tambora earthquake in the range of 6.8 to 7 (Yokoyama, 2001). Such large earthquakes may have not been caused only by volcanic eruptions but

may have been also related to tectonic movements in some areas around Tambora Volcano. During the 1883 eruption of Krakatau in the Sunda Straits, the second largest eruption in historic time after the Tambora eruption, there are no reports of such large earthquakes. This fact also points to the large magnitude of the Tambora eruption.

After the 1815 eruption of Tambora Volcano, several pioneering geologists such as Zollinger (1855) studied this eruption. Afterward, Tambora Volcano has produced only minor activity within the caldera, such as an outflow of lavas (0.002 km^3 in volume) from Doro Api Toi (DAT in Fig. 2), reported by Kusumandinata (1979). In 1947, Petroschevsky (1949) carried out field studies within the caldera and reported that the lava flows were about 60 m high and 350 m long and were issued from a small parasitic scoria cone about 100 m high, formed within the caldera around 1880.

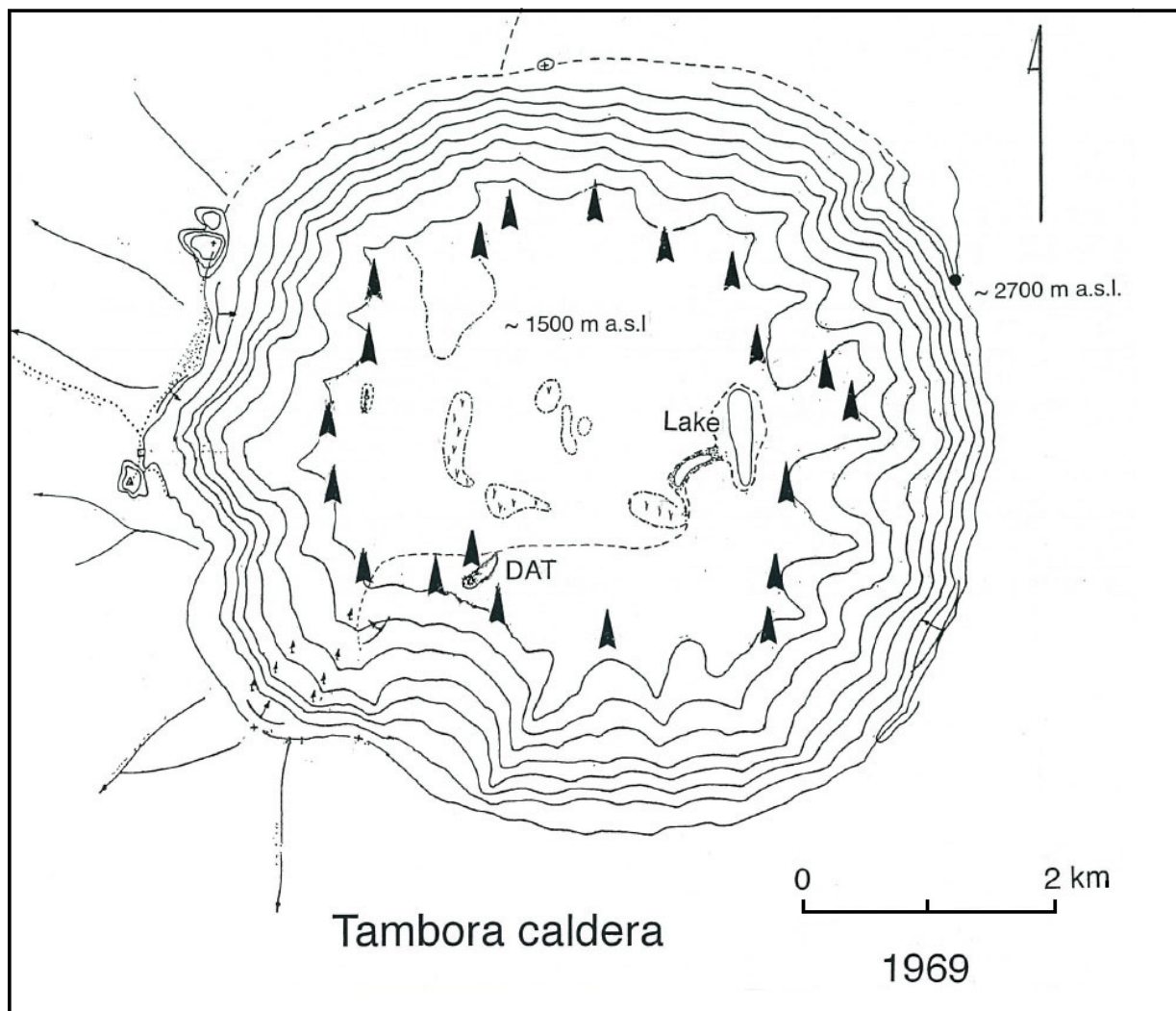


Figure 2. Tambora Caldera. Topographic data from the Volcanological Survey of Indonesia, measured in 1969. The contour intervals are 100 m. "DAT" denotes "Doro Api Toi" which is a small scoria cone with a lava flow. Black triangles denote groups of about 5 fumaroles.

1.3 THE LARGE VOLUME EJECTED BY THE 1815 TAMBORA ERUPTION

For 19th century volcanologists, volume estimation of the Tambora eruption ejecta was an important issue, and fieldwork was possible after the eruptions. Zollinger (1855) estimated the bulk volume of ejecta as 1050 km^3 and later Petroeschovsky (1949) at 100 km^3 . Afterward, Self *et al.* (1984) estimated the bulk volume at 150 km^3 and reappraised that value in Self *et al.* (2004) at 100 km^3 . Those modern studies involve a “dense rock equivalent” (DRE) volume in the range of 30 to 50 km^3 . More recently Kandlbauer and Sparks (2014) reported the most likely volume of ash falls and pyroclastic flows as $41 \pm 4 \text{ km}^3$ DRE. One of the reasons for the wide range of the ejected volume estimations is the location of the volcano in a narrow peninsula surrounded by the sea. Here, we adopt the most recent estimate of Kandlbauer and Sparks, this is, 41 km^3 DRE. A sphere of that volume has a diameter of about 4.3 km. This value may be roughly the diameter of an assumptive spherical magma reservoir. In contrast, for the 1883 Krakatau eruption, Williams (1941) reported 18 km^3 DRE of pyroclastic material ejected, including 5% of old lava fragments.

Lately, Yokoyama (2014) revisited the Krakatau caldera deposits and discussed the negative gravity anomalies in the caldera previously observed by Yokoyama and Hadikusumo (1969) and later surveyed extensively by Deplus *et al.* (1995). Yokoyama (2014) graphically obtained the mass anomaly (deficiency) at the Krakatau caldera as $2 \pm 0.5 \times 10^{12} \text{ Kg}$ from the observed gravity anomaly using a density contrast between the basement and the marine deposits of 150 kg/m^3 , after considering various possible conditions of dry and underwater volcanic deposits and applying the Gauss's theorem. The bulk volume was calculated as the ratio of the mass anomaly to the density contrast: $2 \pm 0.5 \times 10^{12} \text{ Kg} / 150 \text{ kg/m}^3 = 13 \pm 3 \text{ km}^3$ (DRE).

As mentioned above, the deposit volume of Tambora Caldera has been estimated at $41 \pm 4 \text{ km}^3$ DRE which is about 3 times as large as the volume ejected by the 1883 Krakatau eruption. However, it is important to remark that both Tambora and Krakatau volcanoes are located near or surrounded by the sea, and estimations of the ejected volumes are technically difficult and subject to future reappraisals.

DYNAMICS OF THE FORMATION OF CONE-SHEETS AND CALDRON SUBSIDENCE

Volcanic edifices are usually composed of lavas and pyroclastic deposits. Such rocks, commonly have a low shear to compressive strengths ratio, thus breaking more easily under shear stress than under compressive or tensile stresses. This may explain the shape of some volcanic structures. Among the first to address this problem was Anderson (1936, 1937) who discussed "the dynamics of the formation of cone-sheets, ring-dykes, and caldrion-subsidence". Some results of his discussion on the stress field caused by a point dilatation in an elastic medium with a free surface are reproduced in Fig. 3 (Fig. 8 in Anderson, 1936). He showed that opening fractures causing cone-sheet intrusions would follow the fine solid lines in the diagram, stressing the importance of shear fracturing. Afterward, and based on the theory of maximum shearing stress, it was found that the maximum shear stress in such configuration is equal to half the horizontal differential stress and that the shear stress has extreme values at $r = \pm 0.82 D$, where r denotes the horizontal radial distance from the pressure source center and D its depth (De la Cruz-Reyna and Yokoyama 2011; Yokoyama 2013, 2014). In other words, the maximum horizontal differential stress concentrates along a line from the pressure source to the site of potential fracturing at the surface with a dip angle of 51° (red lines in Fig. 3, superimposed

to the stress field calculated by Anderson, 1936). In three dimensions, lines S_1 and S_2 generate an inverted cone or “funnel” with a basal diameter of 1.64 times the depth of the pressure source center at the cone apex.

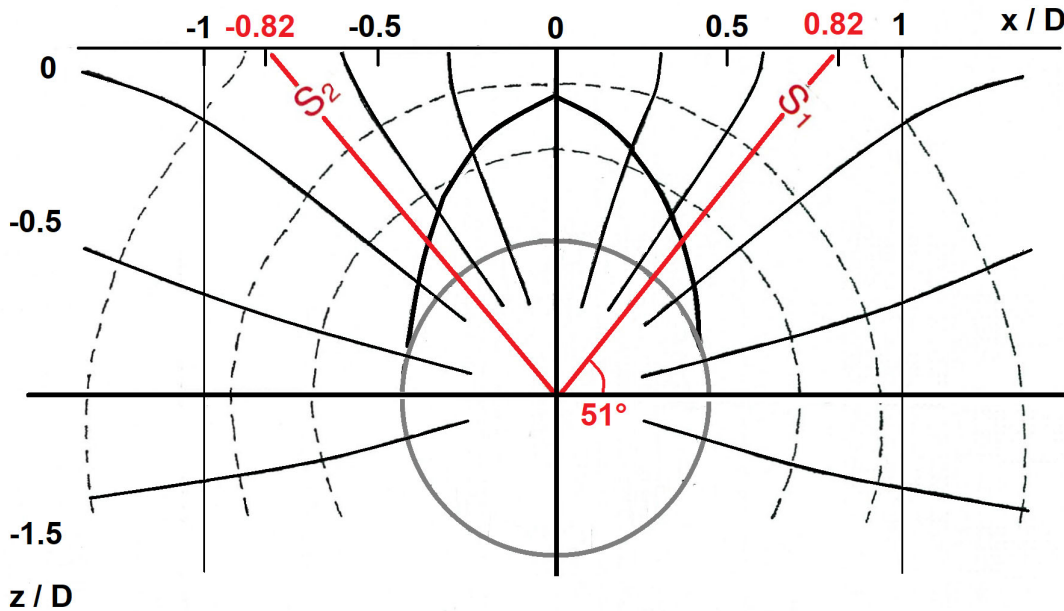


Figure 3. Stress field produced by point dilatation beneath a free surface adapted from Anderson (1936). The red lines S_1 and S_2 were added here to represent the lines of maximum differential horizontal stress (De la Cruz-Reyna and Yokoyama, 2011).

THE SUBSURFACE STRUCTURE OF TAMBORA CALDERA

1. ASSUMPTIVE SUBSURFACE STRUCTURE OF TAMBORA CALDERA INFERRED FROM ITS MORPHOLOGY AND DIMENSIONS

Since its formation, scores of geological data on Tambora Caldera have been published. Recent contributions have provided valuable additional information on the caldera structure (e.g. Self *et al.*, 1984; Foden 1986; Barberi *et al.*, 1987, and Takada *et al.* 2000). In the present paper, a likely subsurface structure of this volcano is discussed, but first, it is important to summarize the basic history of this volcano activity. Barberi *et al.* (1987) showed that the oldest lavas in the 1815 caldera walls are about 55,000 years old and that the previous main event occurred nearly 5000 years before 1815. According to Petroschevsky (1949), the volcano unrest began in 1812. A dense cloud near the summit and rumblings from the shield volcano were reported about 3 years before the 1815 eruption. However, after the 1815 outburst, Tambora Volcano has not produced any significant eruptions, probably because the 1815 eruption volcano exhausted most of its magmatic internal energy. In contrast, Krakatau volcano, which Yokoyama (1957) estimated released about one order of magnitude less energy in its 1883 eruption, has produced repeated smaller eruptions afterward. While Tambora's structure is rather simple, the parasitic activity of Krakatau has been important. This may be caused by their different internal structures.

Fig. 4 illustrates an assumptive E-W vertical cross-section of the Tambora Caldera. There, the profile **S-R₁-C-R₁'** represents the upper part of the pre-caldera shield volcano observed before 1815, with its summit **S** at 4000 m a.s.l., which was demolished by the explosive eruption to an altitude of 2850 m a.s.l. The line from the eastern caldera rim **R₁** at that altitude to the point **P₁** represents the inner caldera slope at a dip angle of 51°, as calculated from the above-mentioned shear fracture model (De la Cruz-Reyna and Yokoyama, 2011). Therefore, one may estimate the depth of the explosion-causing pressure source (**P₁**) at 1.6 km below sea level, which could have been the upper end of a magma conduit connected to deeper magma reservoirs, probably near 5 km b.s.l.

One may have expected that the largest explosive eruption in recorded human history produced a crater bigger than 6.7 km in diameter, as other older calderas around the world are larger. Explaining this is one of the main objectives of this paper and at this stage, it may be argued that this was caused by the relatively shallow depth of the explosion center. Had the explosion source center been deeper and more energetic, say at **P₂** in Fig. 4, at 4 km b.s.l., the expected explosion caldera would have been 10 km wide, with a lower rim altitude. The volume of the deposits within the 6.7 km wide funnel-shaped caldera illustrated in Fig. 4 is estimated at 47 km³, while the assumed 10 km diameter caldera (with its eastern limit located at **R₂**) would have 157 km³ deposited within the funnel.

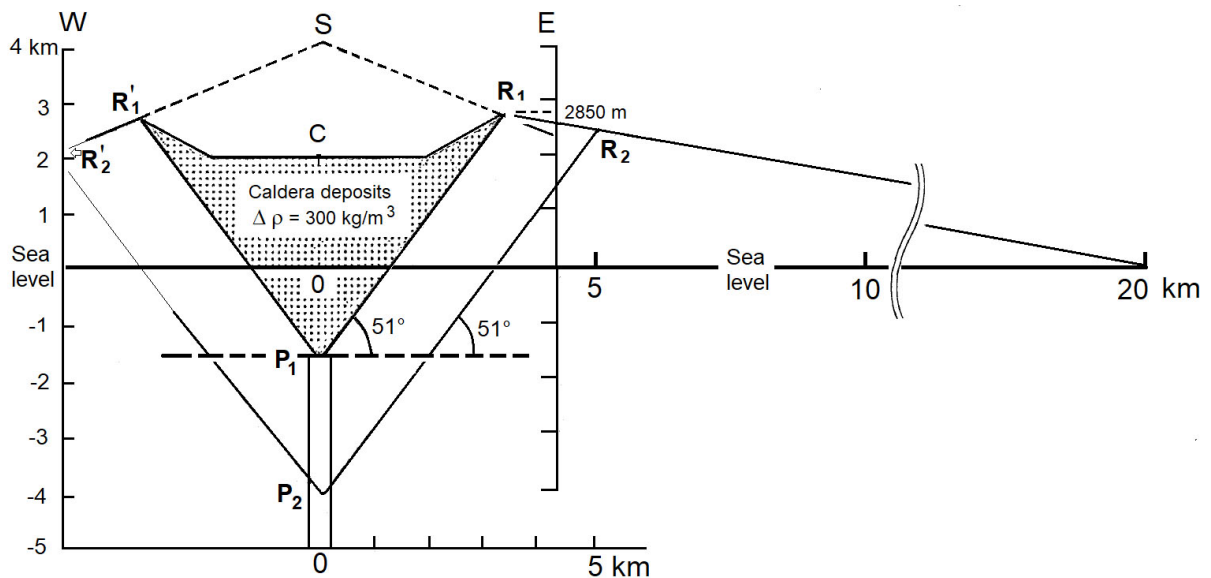


Figure 4. An assumptive E-W section of the 6.7 km diameter Tambora Caldera. Point **S** marks the summit of Tambora Volcano before the 1815 eruption at 4000 m a.s.l. The line from **R₁**, the eastern rim of the caldera to **P₁** represents the caldera slope assumed by the shear fracture model and corresponds to line **S₁** in Fig. 3. Using the same model, a deeper pressure source **P₂** would produce a wider conic caldera with **R₂** as its eastern limit.

2. GRAVITY ANOMALIES RELATED TO THE DEPOSITS IN THE TAMBORA CALDERA

In 1815, Tambora Volcano blew out about 63 km³ of volcanic material, including part of the pre-eruption shield volcano. From this, the caldera deposits amount to about 47 km³ in bulk as discussed in the previous section. The caldera deposits are composed of breccias from the volcanic structure and ejecta fallbacks of relatively low density, around 1.5×10^3 Kg/m³. Then, assuming a density contrast of 3×10^2 Kg/m³, a gravity low around -13 mGal should be expected at the center of the caldera

floor (C in Fig. 4). Thus, Tambora Caldera may be classified as a low-gravity-anomaly-type (LGA-type) which is characterized by thick deposits of fallbacks of ejecta derived from andesitic and dacitic magmas. Another caldera type is the high-gravity-anomaly-type (HGA-type) shall be referred to in the following sections.

“TAMBORA-TYPE” CALDERAS

How large a caldera could be? Can a single eruption like the 1815 Tambora event produce calderas of any size? The diameter of calderas may provide important clues on their origins, but there should be many other conditions needed to answer the question. The historical activity suggests that the 6.7 km width of the Tambora Caldera may be close to such a limit. Here, a diameter of 10 km is assumed to be the maximum theoretical diameter of a single eruption caldera, and such structure is labeled as a “**Tambora-type caldera**”. Based on explosive energy considerations, Steinberg (1974) estimates the same limiting diameter for a crater formed by the single largest possible volcanic explosion. However, it is well known that many calderas exceed a 10 km diameter. In the following sections, the further enlargement of calderas by subsequent eruptions and by other factors like erosion is discussed, but before it is important to point out the differences between two different types of calderas.

As stated above, calderas are classified into two types according to their origins, namely the collapse-type or HGA-type, and the explosion-type or LGA-type. On the Earth, the latter is much more abundant than the former. The *collapse-type calderas* such as Izu-Ooshima (Japan), Kilauea (Hawaii), Fernandina (Galapagos), Batur (Bali), and others are generally formed by the drainage of shallow basaltic magma reservoirs causing stepwise subsidence or collapse of the overlying ground or volcanic structure to fill the voids. This causes local high gravity anomalies as only high-density material is left under that type of caldera floor.

The *explosion-type calderas*, as is the case of the 1815 eruption of Tambora Volcano are globally more numerous than the collapse type. Pyroclastic ejecta derived from siliceous magmas and debris of the overlying structures are deposited on and around the volcano, sometimes forming welded tuffs. Lower-density deposits of such ejecta originate local low-gravity anomalies, this is the LGA-type.

Hitherto, caldera formations were frequently generalized and believed to be “collapse type” assuming or inferring shallow magma reservoirs, and little attention has been given to the explosion-type calderas. Yokoyama (2016) presented a critical discussion on this hypothesis and pointed out that when a relatively deep magma reservoir (at depths around 5-10 km) --which may be formed by complex arrays of dykes and sills-- discharges any amount of magma, those elements should be accordingly compressed by lithostatic pressure, dissipating the stress and leaving little or no space to accept collapsing edifices. Such a process would not form an LGA-type caldera.

Differences between craters and calderas. Craters are usually formed by explosions that keep a conic or funnel shape around a central emission center. Calderas are usually much larger in diameter and are filled with thick layers of fallback pyroclastic and lithic debris deposits, and sometimes cinder cones formed by post-caldera activity. As a result, craters do not show particular gravity anomalies, while calderas exhibit local low or high gravity anomalies depending on the magma type, silicious or basic, and the dynamics of the eruption, explosive or effusive. As mentioned above, the three examples of historical calderas, Tambora, Krakatau, and Novarupta discussed by Yokoyama (2016) were

formed by large-magnitude and strongly explosive eruptions, in which the eruptive energy is released by most of the magma body, and are thus not followed by any major further eruptive activity. The Tambora 1815 eruption is a particularly clear example of an explosion caldera formation and can be used as a reference or standard to describe other calderas in the world.

COMPOSITE CALDERAS FORMED BY MULTIPLE TAMBORA-TYPE ADJACENT ERUPTIONS

In the previous sections, the Tambora-type calderas have been presented as a typical example of newly-born volcanic structures formed by single eruptions and having a limiting diameter of about 10 km. Here, that answer to the question posed and discussed in section 4: how large an LGA caldera may be? leads to a new question: how explosion-type calderas larger than such limiting diameter are formed? An answer is that the known large LGA-type calderas on the earth are composite calderas formed by subsequent Tambora-type adjacent eruptions. To discuss such combined calderas, Aso and Aira calderas in Kyushu, Japan (Fig. 5) are used as examples in the following.

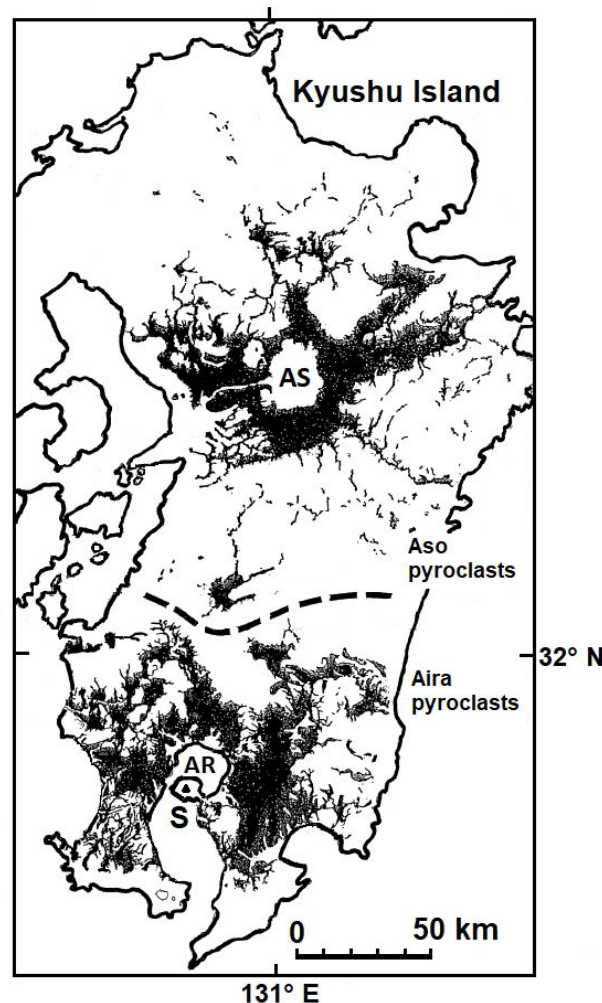


Figure 5. Distribution of pyroclastic ejecta from both the calderas after Matumoto (1943). **AS** Aso Caldera; **AR** Aira Caldera; **S** Sakurajima Volcano. This figure is adapted from the original paper of T. Matumoto (1943), who made important contributions to the geology of the area. In the original figure “Aso lava” and “Aira lava” were corrected as Aso pyroclasts and Aira pyroclasts respectively.

1. ASO CALDERA

Aso Caldera measures $25 \times 17 \text{ km}^2$, second in size only to the Kuccharo Caldera in Hokkaido, measuring $26 \times 20 \text{ km}^2$. The highest altitude at Aso Caldera is the Takadake Cone at 1592 m a.s.l. (**T** in Figure 6) and the caldera rim is on average about 800 m a.s.l. Around the caldera, voluminous deposits of pyroclastic ejecta are distributed as shown in Fig. 5. Geological studies have established that the caldera-forming eruptions at the Aso area continued through $270 - 90 \times 10^3 \text{ YBP}$ and during that period occurred four large pyroclastic flows, named "Aso-1 - 4 Flows". Of those flows, the Aso-4 Flow was the largest, amounting to 400 km^3 in bulk.

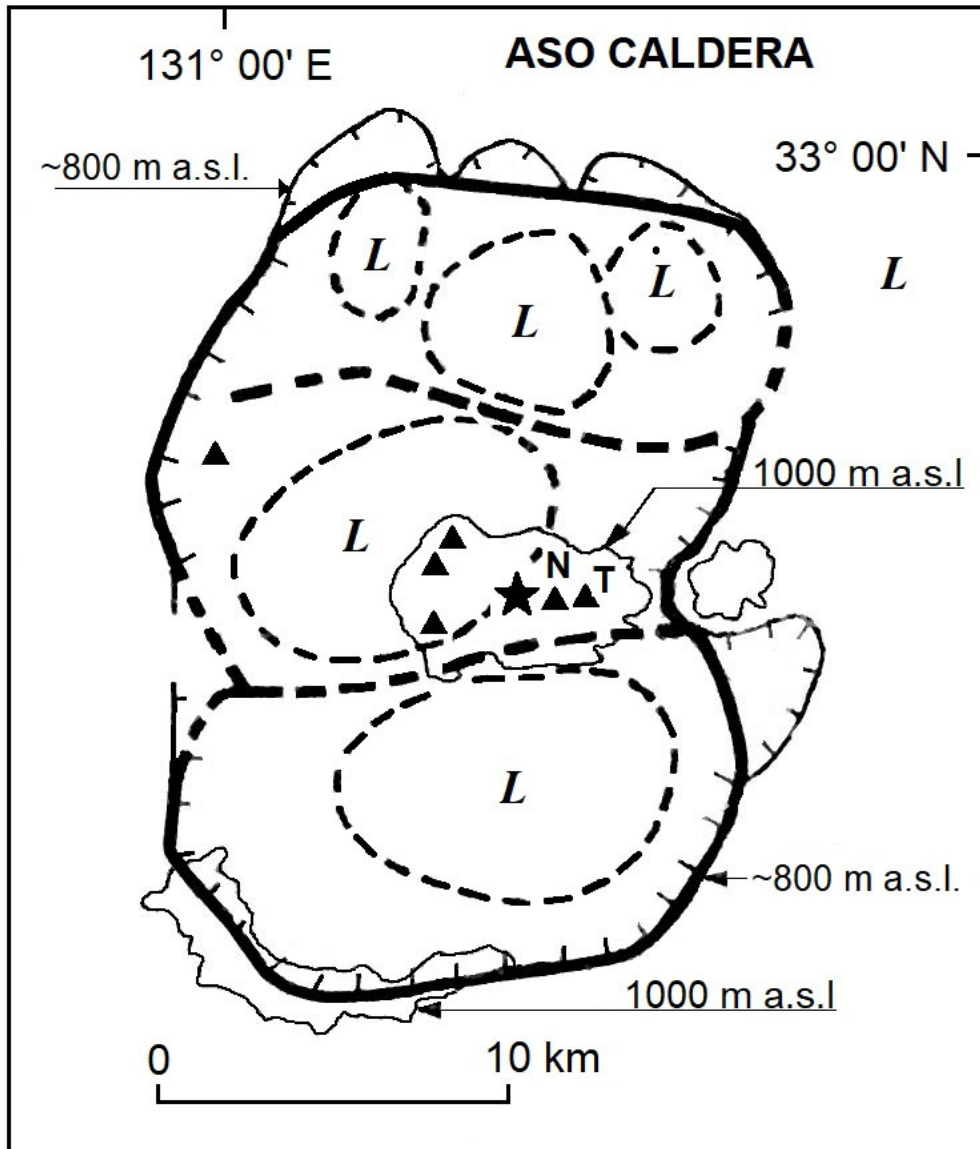


Figure 6. Aso Caldera is composed of three adjacent Tambora-type calderas. Gravimetric data from Komazawa (1995) identify local negative residual gravity anomalies denoted "L". Black triangles in the central part denote post-caldera cones: "T" is the highest one, Takadake Hill (1592 m a.s.l.). The star symbol denotes a group of vents, from which Nakadake Hill (**N**) is currently active.

The large dimensions of Aso caldera are thus explained here as the result of three Tambora-type eruptions developing with a north to south trend. The limits between such calderas, each with dimensions in the order of 10 km, are marked by the thick broken lines in Figure 6. The adjacent Tambora-type eruptions and the erosion on their borders caused the large dimensions of the actual caldera. Geophysical data support this interpretation, Komazawa (1995) carried out detailed gravity surveys and performed 2- and 3-dimensional analyses of the results. He obtained negative residual gravity anomalies for the caldera structure caused by deposits shallower than 5 km. These LGA areas, denoted by “L” in Fig. 6 are somewhat irregular, with the northern part containing 3 components of Tambora-type calderas distinguished by local gravity anomalies. In this area, the 3 components may have separately expanded toward the north as suggested by the topography. The middle part of the caldera may be the last formation and produced 5 post-caldera cones, one of which, Nakadake Hill (N in Fig. 6) near the center of the group holds active vents (star mark), recently erupting in October 2016, January-June 2020 and October 2021. Both the north and south parts are characterized by topographical lows, partially covered with lake sedimentary deposits.

Therefore, according to the Tambora-type nesting of adjacent major eruptions model, it is assumed here that the three Tambora-type calderas forming the composite Aso caldera resulted from three separated magma reservoirs that according to the Komazawa gravity model are located at depths near 5 km. Another major caldera, Aira, with a similar origin is described in the next section.

2. AIRA CALDERA

Aira Caldera, located at the northernmost part of Kagoshima Bay, measures more than 10×20 km² (Fig. 7a). Its morphology is characterized by two depressions that were originally formed on land around 22,000 YBP according to Aramaki (1984). In the following, the actual structure of the caldera is discussed first and from there the original state of the caldera is revised, and its origin reconsidered.

Aira Caldera at present: Currently, the caldera shows two depressions, east, and west. The west depression has a rather flat bottom at around -140 ~ -150 m at the deepest, without active vents or their remains. Apart from the Sakurajima volcano persistent activity, no seismic activity of volcanic origin has been reported in the caldera area (Iguchi, 2007).

The east depression is wider than the west one and it may be a composite structure formed by two 10 km wide Tambora-type calderas aligned in the north-south direction. There are three vents (marked by blank triangles in Fig. 7a), and the northernmost one, “Tagiri” (boiling in Japanese) is still active while the other two are probably extinct.

Within Aira Caldera, there are various Tertiary cones and islands, marked T1, T2, and T3 in Figs. 7a and 7b. In the east caldera, there are two islets, (S1 and S2 in Fig.7a). According to Kuwashiro (1964), these islands appeared in 1780, when Sakurajima Volcano erupted, but they were not derived from the volcano. They were issued from the boundary wall of the east caldera.

Thereafter, but before Sakurajima Volcano was formed at the south of the depressions, around 13,000 YBP, they were flooded by the sea from the south at both west and east sides, forming the Kagoshima Bay. After many centuries, in 1914, the strait between Sakurajima Island and the Oosumi Peninsula was dammed up by lava flows from the erupting Sakurajima Volcano as shown by the present topography.

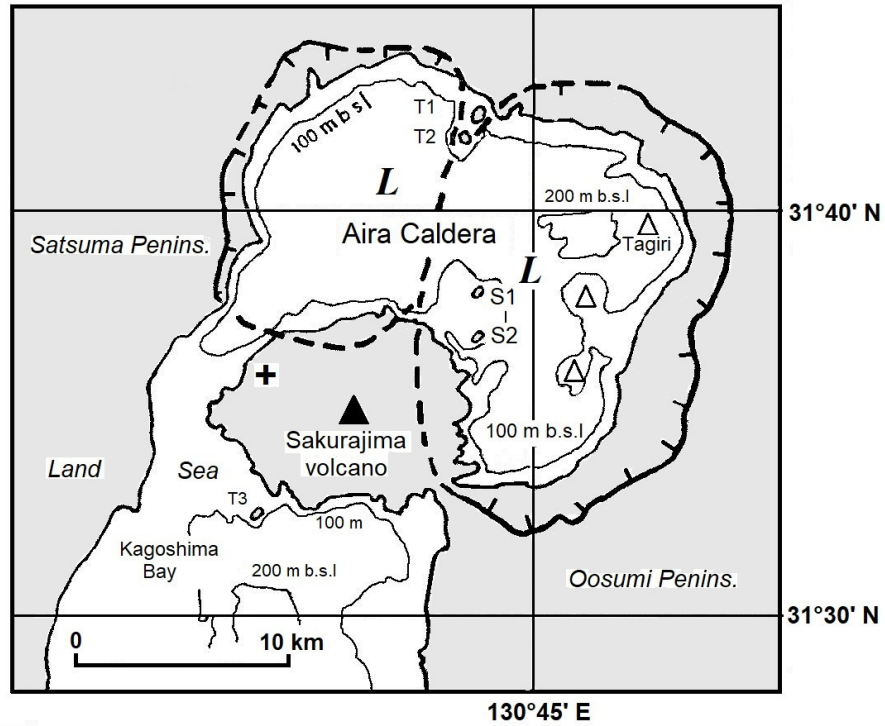


Figure 7a. Aira caldera at present. Only 100 m bathymetric contours are shown. *L* denotes low-gravity anomalies. T1, T2 and T3 are on the Tertiary basement.

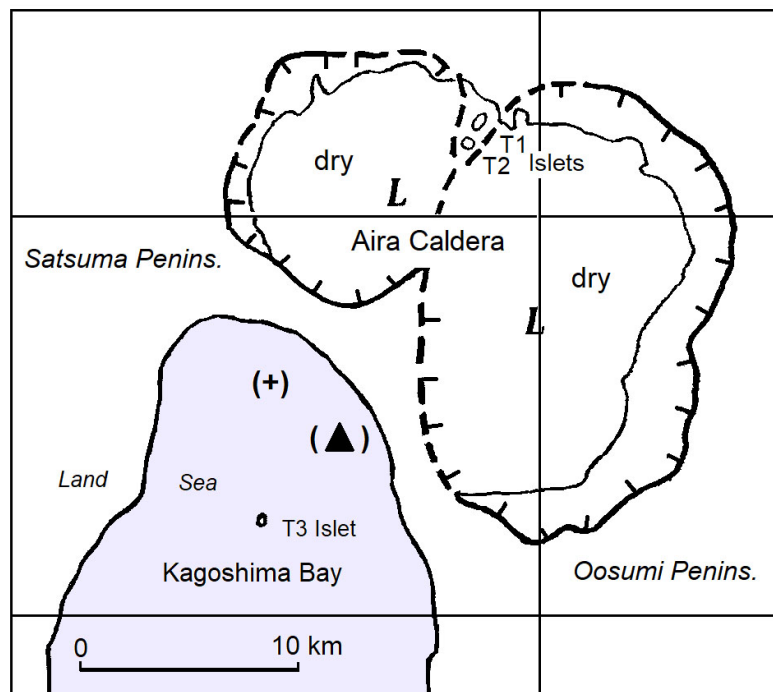


Figure 7b. An assumptive early stage of Aira Caldera at around 22,000 YBP. The caldera boundaries are assumed to be similar to the present ones. The (+) mark denotes the present site of an 800 m deep exploration borehole and (▲) marks the actual summit of Sakurajima Volcano.

The sea surrounding Sakurajima Volcano is for the most part shallow, but there are two deeper areas at -200 m isobaths: one in the eastern caldera and another at the south of Sakurajima Island extending to the Kagoshima Bay. In 1975, Chujo and Murakami (1976) carried out a multi-parametric preliminary geophysical survey on the Kagoshima Bay including the coastal areas. Later, in 2008, Miyamachi *et al.* (2013) carried out seismological surveys to study the seismic wave velocity structure to depths up to 4 km beneath this area, including the active Sakurajima Volcano. Yokoyama and Ohkawa (1986) discussed the subsurface structure around Sakurajima Volcano mostly from the gravity anomaly data. They reported that such anomalies at the center of the caldera are -25 mGal and estimated the depth of the Tertiary basement under Sakurajima Volcano at about 2.5 km b.s.l.

Aira Caldera initial stage: Fig. 7b envisions the initial conditions of Aira Caldera around 22,000 YBP, as composed of two depressions, E, and W, with a boundary that could be a line from the two islets (T1 and T2) on Tertiary basements at the northernmost part, to the south similar islet (T3). The present heights of T1 and T3 isles are 125 m and 38 m above sea level, respectively. At that time, the northernmost part of the Kagoshima Bay was above sea level and the caldera boundaries are hypothetically assumed to be the same as the present ones. The calderas were then formed on land, and Aira Caldera was later flooded by the sea at Kagoshima Bay from S to both W and E. The E depression has kept some post-caldera activity under the sea.

Formation of Sakurajima Volcano: A post-caldera volcano, Sakurajima Island was formed around 13,000 YBP from adjacent lava flows from parasitic vents on its slopes. The island became connected to the Oosumi Peninsula during the 1914 eruption by lava flows. At present, the southern summit-crater is active producing repeated explosive eruptions. At the NW foot of Sakurajima Volcano, the mark (+) in Fig.7b, denotes the position of a borehole about 800 m deep, penetrating under recent Sakurajima deposits and not disturbed by the active volcano (▲ marks its summit). All of the cores from the borehole are of marine origin suggesting that it is located outside the Aira Caldera.

CONCLUSIONS

The formation of cauldron-subsidence calderas has been explained and discussed in the literature using different models. In particular, calderas resulting from major explosive eruptions in silicic volcanoes need interpretations that explain some geophysical features observed in field studies, among which, the local low gravity anomaly and the geometry of the fallback deposits inferred from seismic studies are most important and contrastingly different from the geophysical characteristics of collapse calderas associated to basaltic volcanism. To explain the geophysical characteristics of the low-gravity anomaly calderas, the dynamics of cauldron-subsidence caused by major explosive eruptions is reviewed here in terms of the stress field caused by a center of dilatation in a homogeneous isotropic semi-infinite solid. For relatively shallow magma bodies such stress field vantage the formation of large funnel-shaped craters that can reach up to 10 km in diameter provided the magma body stores sufficient internal energy. The slope of the funnel conical surface is determined by the maximum shear stress induced by the expanding magma body, as illustrated in Fig. 3. The caldera formed by the 1815 Tambora eruption is consistent with this model, and similar structures are thus called Tambora-type calderas.

Some geophysical features, mostly the gravity anomaly distribution on large explosion calderas, like Aso and Aira, exceeding the theoretical 10 km diameter limit, indicate that they were probably

formed by recurrent and adjacent Tambora-type eruptions. For Aso, three roughly aligned in the N-S direction, the central one being the youngest as suggested by the active cones in its interior, and two for Aira, roughly aligned in the E-W direction, although the eastern depression may be formed by two other Tambora-type calderas. Data from the borehole and the three tertiary cones depicted in Fig. 7b suggest that the Aira nested calderas probably formed over 20,000 YBP on dry land, and were eventually flooded, extending the Kagoshima Bay to the north.

ACKNOWLEDGEMENTS

The author owes his knowledge on various aspects of many calderas to innumerable pioneering researchers and wishes to pay his respects to them. Among them, the late Prof. T. Matumoto, who first studied the ignimbrites in Kyushu. His original figure is adapted in Fig. 5. The author gratefully expresses his thanks to Prof. S. De la Cruz-Reyna who kindly contributed to improving the scientific and linguistic quality of this paper. Thanks are also due to Ms. Tomoko-Maki who kindly prepared the figures correctly.

REFERENCES

- Anderson E.M., 1936. Dynamics of the formation of cone-sheets, ring-dykes, and cauldron-subsidences. *Proc. Soc. Edinburgh*, 56, 128-157.
- Anderson E. M., 1937. Cone-sheets and ring-dykes: the dynamical explanation. *Bulletin Volcanologique*, 1(1), 35-40.
- Aramaki S., 1984. Formation of the Aira caldera, southern Kyushu, - 22,000 years ago. *J. Geophys. Res.*, 89, 8485-8501.
- Barberi S., Bigioggero B., Boriani A., Cattaneo M., Cavallin A., Eca C., Cioni R., Gelmini R., Giorgetti F., Iaccarinn S., Innocenti F., Marinelli G., Slejko D., Sudradjat A., 1987. The Island of Sumbawa; a major structural discontinuity in the Indonesian Arc. *Boll. Soc. Geol. It.* 106, 547-620.
- Chujo, J., Murakami F., 1976. The geophysical preliminary surveys of Kagoshima Bay. *Bull. Geol. Surv. Jpn.* 27, 35-55 (in Japanese with English abstract).
- De la Cruz-Reyna, S., Yokoyama I., 2011. A geophysical characterization of monogenetic volcanism. *Geofísica Internacional*, 50, 465-484.
- Deplus C., Bonvalot S., Dahrin D., Diament M., Harjono H., Dubois J., 1995. Inner structure of the Krakatau volcanic complex (Indonesia) from gravity and bathymetry data. *J. Volcanol. Geotherm. Res.*, 64, 23-52.
- Foden, J., 1986. The petrology of Tambora volcano, Indonesia: a model for the 1815 eruption. *J. Volcanol. Geotherm. Res.*, 27, 1-41.
- Gutenberg B., Richter C. F., 1956. Earthquake magnitude, intensity, energy, and acceleration (Second paper). *Bull. Seismol. Soc. Amer.* 46(2), 105-145.
- Iguchi M., 2007. Structure of Sakurajima volcano revealed by geophysical observation and significance of its survey. *J. Geophys. Exp. Soc. Jpn.*, 66, 145- 154 (in Japanese with English abstract).
- Kandlbauer, J., Sparks, R. S. J., 2014. New estimates of the 1815 Tambora eruption volume. *J. Volcanol. Geotherm. Res.*, 286, 93-100.

- Komazawa, M. (1995) Gravimetric analysis of Aso Volcano and its interpretation. *J. Geod. Soc. Jpn.*, 41, 17-45.
- Kusumadinata, K. (editor) (1979). Catalogue of references on Indonesian volcanoes with eruptions in historical time. *Directorate of Volcanology Indonesia*, 820 pp.
- Kuwashiro, I., 1964. On the proto-caldera, the case of the Aira caldera. *J. Geogr.*, 73, 114-120.
- Matumoto, T. (1943) The four gigantic caldera volcanoes of Kyushu. *Jpn. J. Geol. Geogr.*, 19, 57 pp.
- Miyamachi, H. and other 23 authors (2013) Shallow velocity structure beneath the Aira caldera and Sakurajima volcano as inferred from refraction analysis of the seismic experiment in 2008. *Bull. Volcanol. Soc. Jpn.*, 58, 227-237.
- Petroeschevsky W. A., 1949. A contribution to the knowledge of the Gunung Tambora (Sumbawa). *K. Ned. Aardrijksk Genoots Tijds*, 66, 688-703.
- Self, S., Rampino, M. R., Newton, M. S., Wolff, J. A., 1984. Volcanological study of the great Tambora eruption of 1815. *Geology*, 12(11), 659-663.
- Self, S., Gertisser, R., Thordarson, T., Rampino, M. R., and Wolff, J. A., 2004. Magma volume, volatile emissions, and stratospheric aerosols from the 1815 eruption of Tambora. *Geophysical Research Letters*, 31(20), L20608.
- Sigurdsson, H., Carey, S., 1989. Plinian and co-ignimbrite tephra fall from the 1815 eruption of Tambora volcano. *Bull. Volcanol.* 51(4), 243-270.
- Steinberg, G.S., 1974. On explosive caldera formation. *Modern Geology*, 5, 27-30.
- Takada, A., Yamamoto, T., Kartadinata, N., Budianto, A., Munandar, A., Matsumoto, A., Suto, S., Venuti, M.C., 2000. Eruptive history and magma plumbing system of Tambora volcano, Indonesia, Report of International Research and Development Cooperation ITIT Project, 42-79.
- Williams. H., 1941. Calderas and their origin *Bull. Geol. Sci. Dep (U. of Calif.)*, 25, 239-346. (U of Calif), 25, 239-346.
- Yokoyama, I., 1957. Energetics in active volcanoes, 2nd paper. *Bull. Earthq. Res. Inst.*, 35, 75-97.
- Yokoyama I., Hadikusumo D., 1969. A gravity survey on the Krakatau Islands, Indonesia. Volcanological survey of Indonesian volcanoes, part 3. *Bull. Earth. Res. Inst*, 47, 991-1001.
- Yokoyama, I., 2001. The largest magnitudes of earthquakes associated with some historical eruptions and their volcanic significance. *Annali di Geofisica*, 44 (5-6), 1021-1029.
- Yokoyama I., 2013. Parasitic eruptions on Sakurajima volcano. *Bull. Volcanol. Soc. Japan*, 58(1), 91-102
- Yokoyama, I., 2014. Krakatau caldera deposits: revisited and verification by geophysical means. *Annals of Geophysics*, 57(5), S0541; doi:10.4401/ag-6404
- Yokoyama, I., 2016. Origin of calderas: discriminating between collapses and explosions. *Annals of Geophysics*, 59(6), S0650; <https://doi.org/10.4401/ag-7010>

<https://doi.org/10.22201/igeof.00167169p.2022.61.1.2120>

RADIOACTIVE HEAT PRODUCTION CHARACTERIZATION OF AR-RASSAFEH BADYIEH AREA (AREA-2), SYRIA USING AERIAL GAMMA RAY SPECTROMETRIC AND FRACTAL MODELING TECHNIQUES

Jamal Asfahani^{1*}

Received: January 14, 2021; accepted: October 25, 2021; published on-line: January 1, 2022.

RESUMEN

En este estudio se utilizó la técnica de espectrometría de rayos gamma para evaluar la producción de calor radiactivo (HP, por sus siglas en inglés) del área de Ar-Rassafeh Badyieh (Área-2), en Siria. Las nueve unidades establecidas, puntuadas con anterioridad, para el Área-2 se caracterizaron por separado para el parámetro HP. Como parte de un nuevo enfoque, se propone aplicar el modelo de número de concentración (CN) y los gráficos log-log asociados con la técnica fractal para mapear el equivalente medido de uranio (eU, por sus siglas en inglés), el torio equivalente (eTh, por sus siglas en inglés) y el potasio, (K%) además del HP calculado del Área-2. El HP del Área-2 varía entre un mínimo de 0.06 y un máximo de 4.28 $\mu\text{w}/\text{m}^3$ con un promedio de 0.548 $\mu\text{w}/\text{m}^3$ y una desviación estándar de 0.27 $\mu\text{w}/\text{m}^3$. Los valores de HP más altos observados están relacionados con los ambientes fosfatados representados por dos unidades puntuadas litológicas A y B.

Palabras clave: Producción de calor radiactivo, ambientes fosfatados, espectrometría aérea de rayos gamma. Área-2, Área de Ar-Rassafeh Badyieh y Siria.

ABSTRACT

Aerial gamma-ray spectrometric technique is used to evaluate the radioactive heat production (HP) of Ar-Rassafeh Badyieh Area (Area-2), Syria. The nine already established lithological scored units of Area-2 have been separately characterized for the HP parameter. The Concentration-number (C-N) model and the log-log plots associated with fractal technique are proposed and applied as a new approach to map the measured equivalent uranium (eU), the equivalent thorium (eTh), and potassium (K%) and the computed HP of Area-2. The HP of Area-2 varies between a minimum of 0.06 and a maximum of 4.28 $\mu\text{w}/\text{m}^3$ with an average of 0.548 $\mu\text{w}/\text{m}^3$ and a standard deviation of 0.27 $\mu\text{w}/\text{m}^3$. The highest observed HP values are related to the phosphatic environments represented by two lithological scored units A and B.

KEY WORDS: radioactive heat production, hosphatic environments, aerial gamma-ray spectrometry, Area-2, Ar-Rassafeh Badyieh Area and Syria.

*Corresponding author at cscientific@aec.org.sy

¹ Geology Department, Atomic Energy Commission of Syria, P.O. Box 6091, Damascus- Syria

INTRODUCTION

Geoscientists use generally the geothermal and heat flow data to provide information on the temperature distributions within the earth and thermal evolution history of a sedimentary basin. The thermal history of a sedimentary basin is an important indicator of the organic compound maturity. The maturity of organic compound can be characterized and described as the gradual process, that includes the release of hydrocarbons from buried organic materials (Deming, 1994).

The amount of heat flow in a sedimentary basin has to be constrained with the radiogenic heat production to provide a better understanding of the total heat budget (Biicker and Rybach, 1996). Different researches have been attempted to explain the radioactive heat production distribution nature within the crust, particularly, along the exposed crustal cross sections that provided an excellent opportunity to get the various rock types constituting the crust (Ketcham, 1996; Kumar and Reddy, 2004; Brady *et al.*, 2006).

The heat production is produced in the rocks through the decay of radioactive elements such as uranium, thorium and potassium. The heat production rate of a given rock can be therefore computed based on the concentrations of those radioactive elements and the density rocks (Rybach, 1988).

This paper aimed at using aerial gamma-ray spectrometric technique and its available data of equivalent uranium (eU) in ppm, equivalent thorium (eTh) in ppm, and equivalent potassium (K) in % to compute and map the radioactive heat production (HP) of the study Area-2 as a whole. The heat production parameter HP will be also characterized separately for different environments represented by the nine lithological scored units (Asfahani *et al.*, 2018).

The airborne gamma-ray spectrometric technique has been already used in different worldwide areas to compute radioactive heat production of Gabal Duwi Area, Egypt (Salem *et al.*, 2005), of Gabal Arrubushi area, Central Eastern Desert, Egypt (Yousef, 2016), in northern Palmyrides (Area-3) (Asfahani *et al.*, 2016), and in Syrian Desert (Area-1), Syria (Asfahani, 2018-a).

The Concentration-number (C-N) model and the log-log plots related to fractal modeling technique (Hassanpour and Afzal, 2013) is proposed and applied as a new approach to map the HP parameter for Area-2, and to isolate the HP anomalies from background. In fact, the boundaries of the distinguished radioactive ranges, derived by the fractal modeling technique coincide well with the geological boundaries. This coincidence gives this multi-fractal technique its advantages in comparison with other traditional statistical techniques.

The main objective of the present paper is:

1. to compute the statistical characteristics of the nine lithological scored units of Area-2 (Min, Max, Mean, standard deviation (σ), and coefficient of variability (CV%), for the parameters of total radioactivity (T.C) in Ur, eU, eTh, and K%.
2. to evaluate the radioactive heat production HP for Area-2 as a whole.
3. to characterize separately the heat production HP for different environments represented by nine outcropped scored lithological units, already distinguished by using the factor analysis technique (Asfahani *et al.*, 2018).
4. to map the eU, eTh, K% and HP parameters for the Area-2 with the use of the proposed multi-fractal (C-N) modeling technique.

METHODOLOGY

The available data of airborne gamma-ray spectrometry is used in this paper to compute the HP of the Area-2. The fractal technique is used to map the different ranges of eU, eTh, K% and HP parameters.

AERIAL GAMMA RAY SPECTROMETRY TECHNIQUE

An airborne gamma-ray spectrometric survey for uranium exploration has been conducted in 1987 by the International Atomic Energy Agency and Riso National Laboratory during the project SYR/86/005 in Syria (Riso, 1987; Jubeli, 1990).

A nominal survey 30 m height at an average speed of 120 km/hr along parallel lines with a spacing of 3–4 km was used during this survey, in order to cover most of the interest areas in the Syrian territory. This aerial survey used a compact lightweight of four window gamma-ray spectrometer (Scintrex, GAD-6, Canada) with a 12.5 L (NaI) volume detector. The detector was maintained before the record of each mission, at a constant temperature with the gain stabilization. The system calibration took place at the calibration pads of the Dafa airport in Sweden (Riso, 1987). An efficient flight path control has been provided through using an IGI Loran-C navigation system, which defines and records automatically all waypoints and fiducials of flight tracks along the flight lines. Intervals of one second were used to record the raw data, corrected for background effects, and for the applicable inter-channel Compton corrections. Exponential attenuation factors for height corrections were established (Riso, 1987).

This airborne survey covered the following three areas shown in Fig.1(A and B):

1. The Syrian Desert (7189 line km at 4 km line spacing).
2. Ar-Rassafeh Badyieh (2240 line km at 4 km line spacing).
3. The Northern Palmyrides (1600 line km at 3 km line spacing).

During this survey, it has been observed that the highest gamma-ray anomalies measured are mainly associated with phosphate deposits encountered in Central Syria. A scored lithological map has been recently established through airborne gamma-ray spectrometric data of the Ar-Rassafeh Badyieh Area (Area-2) interpretation by using statistical factor analysis technique (FAT) (Asfahani *et al.*, 2018), as has been already done for (Area-1), (Asfahani *et al.*, 2015).

RADIOACTIVE HEAT PRODUCTION ESTIMATION

Radioactive heat production (HP) of a given rock sample was computed by using an empirical relationship, given by the following expression (Rybach, 1976):

$$HP (\mu\text{w}/\text{m}^3) = \rho (0.0952 \text{ eU} + 0.0256 \text{ eTh} + 0.0348 \text{ k}\%) \quad (1)$$

In which ρ is the dry density of rock (g/cm^3)

The densities are acquired and estimated from web sites such as (http://www.engineeringtoolbox.com/mineral-density_1555.html, http://wiki.chemprime.chemeddl.org/index.php/Density_of_Rocks_and_Soils and http://www.engineeringtoolbox.com/density-solids-d_1265.html).

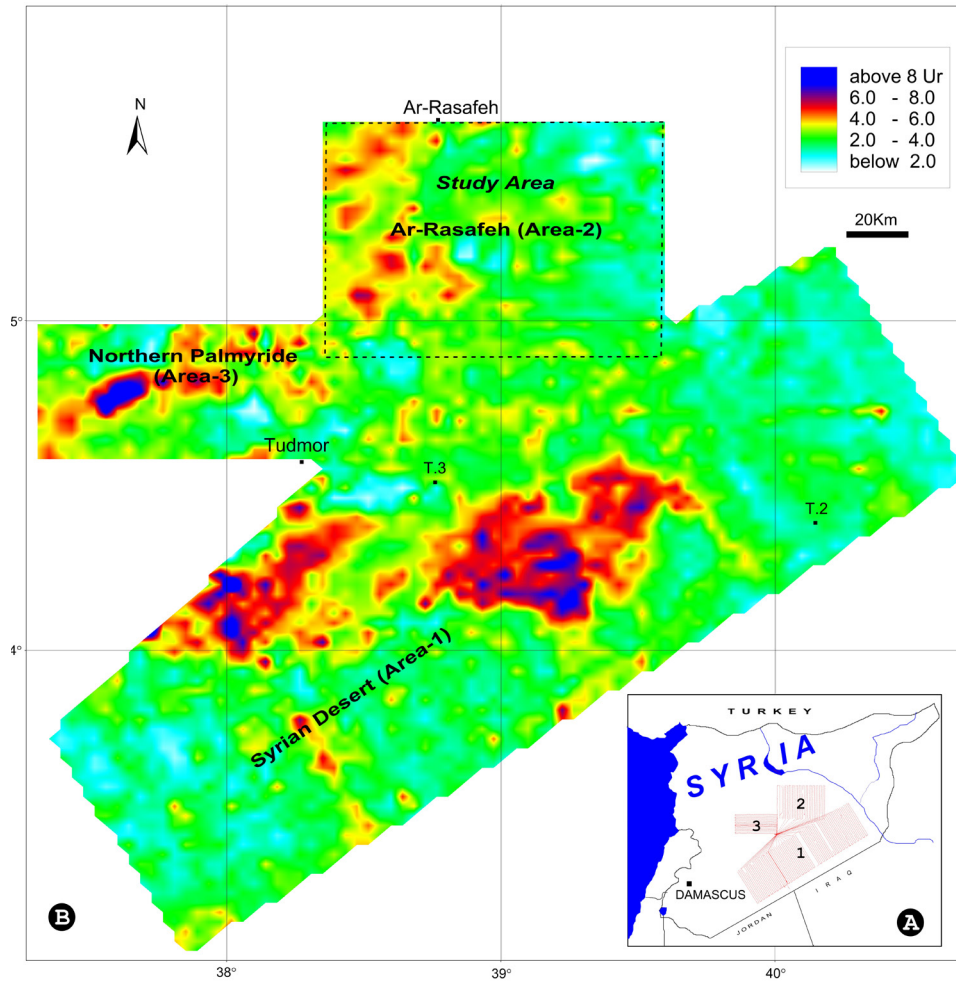


Figure 1

Figure 1. (A) Total areas covered by airborne gamma-ray spectrometric technique and (B) total radiometric map (Ur) resulting from spectrometric survey (Riso, 1987)

Equation (1) computes the energy released during alpha, beta, and gamma decay of the radioelements (Rybach, 1976 ; Birch, 1954).

The constant for uranium (0.0952) in Equation (1) is more than twice the constants for potassium (0.035) or thorium (0.026), meaning that uranium has a dominant role in producing heat compared with thorium or potassium. The dominant role of uranium is due to its alpha decay, which provides most of the radiogenic heat production (Birch, 1954).

Radioactive heat production has been also estimated from the concentrations of radioelements measured in the laboratory (Fernandez *et al.*, 1998), and directly from the gamma-ray logs (Bücker and Rybach, 1996; Asfahani, 2018-c). Besides, the radioactive heat production has been recently evaluated using the available data measurements of airborne gamma-ray spectrometric technique and applying the equation (1) (Richardson and Killeen, 1980; Thompson *et al.*, 1996; Salem *et al.*, 2005; Yousef, 2016; Asfahani *et al.*, 2016; Asfahani., 2018-a).

As indicated by the equation (1), the radioactive heat production estimation in the present case study requires the knowledge of both density of the nine treated lithological scored units (Asfahani *et al.*,

2018), and their available concentrations of eU, eTh, and K% obtained from the airborne gamma-ray spectrometric survey.

FRactal TECHNIQUE AND C-N MODEL

Models based on fractal geometry as a nonlinear mathematical science proposed by Mandelbrot (1983), have been hugely used in the recent years in different branches of earth sciences. Several fractal/ multifractal models have been recently proposed such as concentration-volume (C-V); (Afzal *et al.*, 2011), concentration-distance (C-D); (Li *et al.*, 2003), and concentration-number (C-N); (Afzal *et al.*, 2012, Hassanpour and Afzal 2013), where those fractal models have been applied on 2D and 3D geophysical data.

In fact, the classical statistical methods for delineation the different geophysical populations from background such as histogram analysis, box plot, summation of mean and standard deviation coefficients and median are not accurate. Those traditional methods consider only the frequency distribution of information, while have no attention to spatial variability since the information about the spatial correlation is not always available (Afzal *et al.*, 2010; 2012). Such classical statistical methods assume the normality or log-normality, and do not consider the shape, extent, and magnitude of the geophysical anomalous areas and disregard spatial distribution (Agterberg *et al.*, 1995; Bíró *et al.*, 2012; Shtiza and Tashko, 2009). Those inconveniences encourage the application of fractal models to isolate the geophysical anomaly from its background, as it will be done herein basically for equivalent uranium (eU) and heat production (HP) parameters.

Log-log plots are used while applying fractal models, where the straight line segments fitted the graphs have some break thresholds points (Zuo, 2011; Wang *et al.*, 2011; Mohammadi *et al.*, 2013; Afzal *et al.*, 2017; Khalajmasoumi *et al.*, 2015; Afzal *et al.*, 2018; Daneshvar and Afzal., 2017).

C-N multifractal model is proposed and applied as a new approach to map the measured parameters of eU, eTh, K, and the computed HP for the study Area-2, and to distinguish between different ranges of radioactive anomalies. The same C-N multifractal model has been recently applied on aerial gamma-ray spectrometric data of Northern Palmyrides (Area-3), where useful radioactive isolation anomalies results have been obtained (Asfahani, 2018-b).

The mathematical expression of the Concentration-number (C-N) fractal model is given by the following equation (Mandelbrot, 1983; Hassanpour and Afzal., 2013; Sadeghi *et al.*, 2012; Afzal *et al.*, 2016):

$$N(\geq\mu) = F\mu^{-D} \quad (2)$$

where μ denotes the treated geophysical parameter values, which are in the present case study including eU (ppm), eTh (ppm), K (%) and HP ($\mu\text{w}/\text{m}^3$).

$N(\geq\mu)$ denotes the cumulative number of the treated geophysical data, which are the cumulative number of the measured equivalent uranium (CNeU), the cumulative number of the measured equivalent thorium (CNeTh), the cumulative number of the measured potassium (CNK%), and the cumulative number of the computed radioactive heat production (CNHP), with the geophysical parameter values greater than or equal to μ , F is a constant and D is the scaling exponent or fractal dimension of the distribution of geophysical parameter values.

GENERAL SETTING OF THE STUDY AREA (AREA-2)

TOPOGRAPHY

The study area is considered as a transition zone between the low-mountain and the flat country. This mountain series form the northern limit of Palmyride range (Jabal AL-Bishri), the relief grades east, northeast and southeastwards flood- plains, until it declines to Al-Furat river course in the north-east direction (out of the study area). The undulate sloping flood- plains are cut by many erosional valleys, where some of them are tectono-genetic (Technoexport, 1967, JICA 1996).

STRATIGRAPHY

Cretaceous, Paleogene litho-facies crop-out, while the Neogene and Quaternary sediments cover vast area of wadis and low-lands and flood- plain terraces of the studied territory, Fig.2.

Cretaceous rocks units: The Cretaceous litho- facies are mainly represented by carbonate, marly- clayey limestone, dolomitic limestone, ferruginous sandy limestone organic limestone, phosphate with remnants of fish bones, and flint concretions and bands, sometimes bituminous limestone intercalations, Fig.2.

Paleogene rocks units: the boundary between Cretaceous and Paleogene litho-facies is not prominent. Paleogene outcrops are zonally distributed in the studied territory. It is dominated by the carbonate litho-facies such as clayey limestone, sandy limestone with bitumen occurrences, dolomite, organic limestone, chalky-like limestone, marl, glauconitic- phosphate beds and flint, which are occurred in most of the cross-sections of the studied territory. Those facies denote the palio- shoreline and deltas within littoral zone, Fig.2.

Neogene rocks units: Cover vast tracts of the marginal plains adjacent of Al- Bishri anticline. The lithofacies of Neogene (Technoexport 1967, JICA 1996) denote a continental conditions start with sandy- clayey silt, conglomerates and sandstone with carbonate cement, breccia- like limestone, organic limestone, and dolomite with bitumen and gypsum alternations, Fig.2.

Quaternary and recent rocks units: Eluviation, eolian sands, pebbles of various genetic types and evaporates (JICA 1996), Fig.2.

TECTONIC

The study area is located in the mobile part of Arabian platform slope in the northern marginal zone Palmyride folding system (Dill, 2009; Technoexport, 1967) (Fig.2).

The study area is characterized as block folds, brachy-coffer anticlines, depressions, and regional deep faults. The Palmyride folding system is complicated by deep regional faults, which take north-eastern trend (JICA 1996, Litak *et al.*, 1998). Faulted- flexures are also accompanied with coffer fold- axis.

Most of those mentioned structural features are not marked at the surface, but inferred from geophysical data.

RESULTS AND DISCUSSION

Statistical factor analysis technique was already used to interpret aerial gamma-ray spectrometric data of Area-2, and to establish a scored lithological map for the study area (Asfahani *et al.*, 2018) as

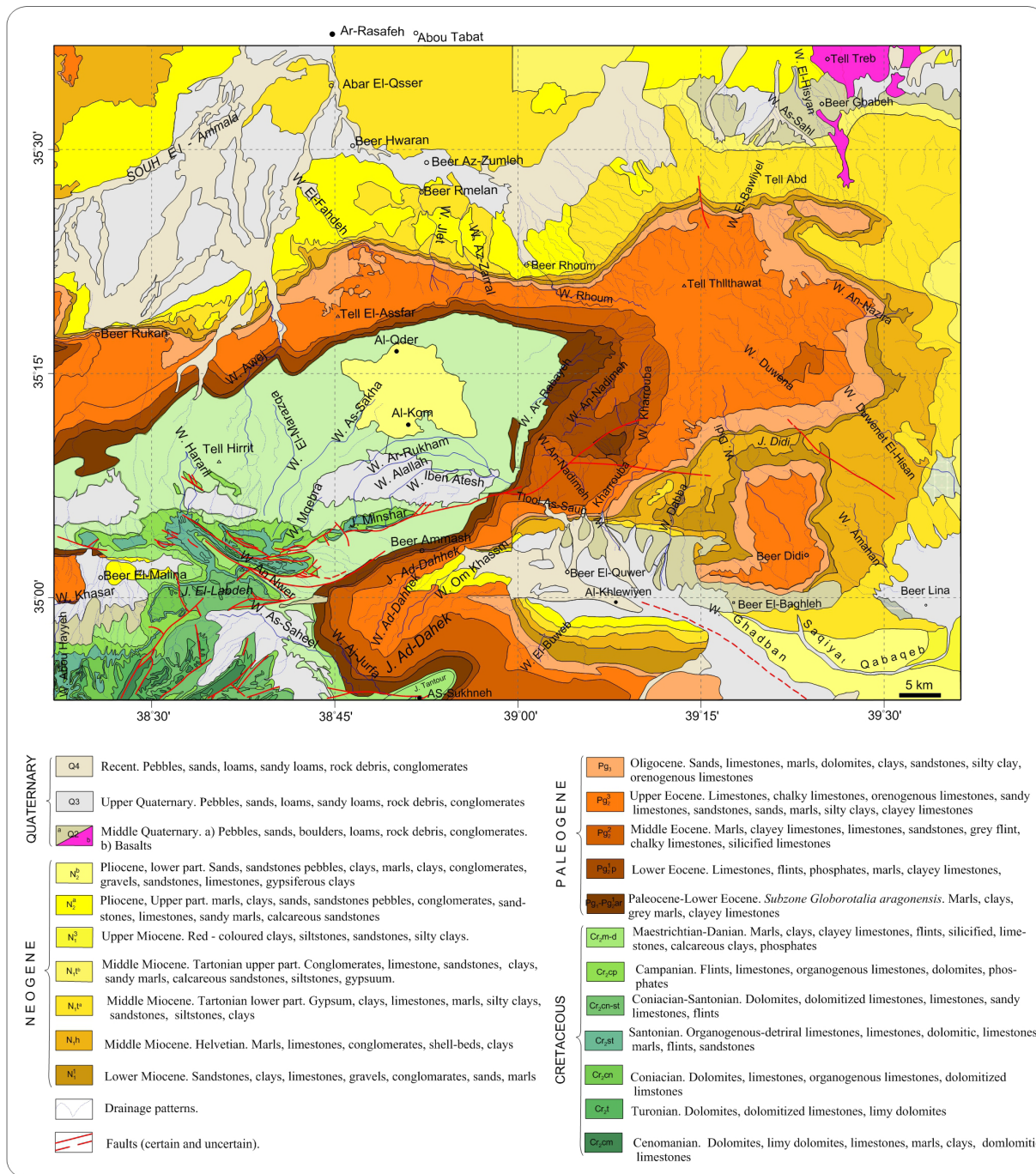


Figure 2. Geological map of Ar-Rassafeh Badyieh Area (Area-2)

shown and presented in Figure 3. The established scored map includes different geological environments, represented by nine different isolated rock units, that are regrouped mainly in three factors (F1, F2, and F3) groups.

Table 1. Characteristics of the nine lithological scored units identified on the scored map (Asfahani *et al.*, 2018).

Factor	Rock units	Environmental litho-facies description	Notices
F1	A	Granular phosphate, fragmental, brecciated-phosphate.	F1 is called as phosphate-uranium factor.
	B	Marly phosphate, calcareous- fissured phosphate covered by hydrous ferric oxide.	
	C	Calcareous glauconitic concretions, calcite-grains enclosed by glauconite.	
F2	D	Paleo-delta deposits, clayey sandstone, silty clay, sandy limestone, glauconitic sandstone.	F2 is called as littoral, paleo-delta and alluvium fans factor.
	E	Volcanic extrusions and basalt sheets.	
	F	Valley- fill deposits, alluviums, debris, clayey limestone, dolomatic limestone.	
F3	G	Detrital, alluvium, conglomerates, limestone.	F3 is called as closed seasonal basin factor.
	H	Sandy loam, fluvial sediments, lacustrine limestone, sands.	
	I	loam, clay, eluviation, eolian sand evaporates, and playa deposits.	

The lithological scored map shown in Fig.3 will be the base for estimating the radioactive heat production HP for Area-2 as a whole, and for characterizing this HP separately the nine distinguished lithological units.

The available aerial gamma-ray spectrometry data of eU, eTh, and K% for the Area-2 firstly allow the computation of the heat production HP according to equation (1) for 45935 aerial measured data points in the study area (Area-2).

According to the application of equation (1), HP varies between a minimum of $0.06 \mu\text{w}/\text{m}^3$ and a maximum of $4.28 \mu\text{w}/\text{m}^3$ with an average of $0.548 \mu\text{w}/\text{m}^3$ and a standard deviation σ of $0.27 \mu\text{w}/\text{m}^3$.

The Table 3 shows the correlation matrix between the five radiometric variables of T.C, K, eTh, eU, and HP for the study area. The high correlation of 0.89 between the eU and the HP confirms that uranium is the main responsible of such a heat production.

It is worth mentioning that the maximum HP value obtained in this paper ($4.28 \mu\text{w}/\text{m}^3$) is comparable and in a good agreement with those obtained in Area-1 and Area-3, where a maximum of HP values of $7.23 \mu\text{w}/\text{m}^3$ and $4.17 \mu\text{w}/\text{m}^3$ have been respectively already obtained (Asfahani, 2018-a; Asfahani *et al.*, 2016).

Secondly, the heat production HP is separately computed for different geological environments, represented by the nine lithological scored units shown on the scored map (Fig.3).

Table 2. Statistical characteristics of the 9 lithological units for 4 radiometric variables in the Syrian Desert area (Area-2).

Litho. units Variables	A (1246)				B (1970)				C (9977)				D (325)							
	Min.	Max.	Mean	σ	CV%	Min.	Max.	Mean	σ	CV%	Min.	Max.	Mean	σ	CV%	Min.	Max.	Mean	σ	CV%
T.C	2.30	17.11	7	1.99	28	1.93	8.89	5.47	0.96	17	0.23	8.36	4.57	1.14	25	0.89	5.18	3.1	0.80	26
K %	0.02	0.44	0.18	0.07	39	0.04	0.46	0.22	0.06	27	0.02	0.63	0.25	0.08	32	0.02	0.22	0.09	0.04	44
eU	1.77	13.6	4.7	1.54	33	1.48	4.30	2.99	0.38	13	0.16	3.29	1.67	0.56	33	0.16	3.34	0.99	0.55	55
eTh	0.19	4.95	2.12	0.82	39	0.33	5.59	2.45	0.76	31	0.17	6.94	2.97	0.102	34	0.107	6.29	3.65	0.99	27

Litho. units Variables	F (14448)				G (1170)					
	Min.	Max.	Mean	σ	CV%	Min.	Max.	Mean	σ	CV%
T.C	1.18	7.37	3.6	0.88	24	0.56	7.38	3.69	0.88	24
K %	0.04	0.41	0.17	0.05	29	0.06	0.75	0.25	0.07	28
eU	0.16	3.14	0.102	0.55	54	0.16	4	0.99	0.51	51
eTh	0.92	8.57	3.88	1	26	0.24	7.54	3.31	0.96	29

Litho. units Variables	H (3228)				I (12648)					
	Min.	Max.	Mean	σ	CV%	Min.	Max.	Mean	σ	CV%
T.C	4.38	8.35	6.17	0.60	9	0.54	7.35	4.31	0.95	22
K %	0.12	0.58	0.39	0.06	15	0.04	0.51	0.26	0.07	27
eU	0.18	04.05	1.88	0.70	37	0.16	4.58	1.48	0.65	44
eTh	2.45	7.21	4.69	0.69	15	0.16	6.62	3.25	0.91	28

The boundaries of those nine scored lithological units are well distinguished and identified, where every unit of them has its specific density and content of eU, eTh and K%. The radioactive heat productions HP are consequently computed according to the equation (1), where eU, eTh, K% and densities of lithological units are available.

The three lithological phosphatic scored units A, B, and C related to the first factor (F1) are characterized by higher values of HP as shown and indicated in Table 4.

The three lithological scored units D, E, and F related to the second factor (F2), composed of surficial washing and abrading products are characterized by prevailing of clayey facies, as marly clay, organic limestone, sandy limestone, sandy clay, sandy varieties intercalated with clayey limestone, silty clay, phosphorite and glauconite sands belonging to the Lower and Middle Paleogene (Techno-export, 1967). They are characterized by an average HP of 0.40, 0.60, and 0.45 $\mu\text{w}/\text{m}^3$ respectively (Table 4).

The three lithological scored units G, H, and I related to the third factor (F3) reflect an environment of flood-closed basins, evaporation pans, bitumen appearances, and paleo-channels of tectonic origin. They are characterized by an average HP of 0.65, 0.47, and 0.43 $\mu\text{w}/\text{m}^3$ respectively (Table 4).

Fig.4 shows the average characteristics of the heat production (HP) for the nine lithological scored units.

The analysis of the empirical relationships between uranium concentration (eU) and computed heat production (HP) for the nine scored lithological units shows strong correlations between those two parameters as shown in Fig.5, where R^2 varies between a minimum of 0.756 for unit E and a maximum of 0.979 for unit A.

Table 3. Correlation matrix of the five radiometric variables in Area-2.

Variables	T.C	K	eTh	eU	HP
T.C	1	0.59	0.48	0.68	0.67
K		1	0.59	0.03	0.03
eTh			1	-0.12	0.01
eU				1	0.89
HP					1

Table 4. The heat production HP ($\mu\text{w}/\text{m}^3$) for the nine lithological scored units.

Serial N	Rock Unit	Density $\rho(\text{g}/\text{cem}^3)$	No of points	Min ($\mu\text{w}/\text{m}^3$)	Max ($\mu\text{w}/\text{m}^3$)	Average ($\mu\text{w}/\text{m}^3$)	σ ($\mu\text{w}/\text{m}^3$)	CV%
1	A		1246	0.69	4.28	1.63	0.48	29.4
2	B	3.2	1970	0.418	1.40	0.89	0.12	13.5
3	C	2.50	9977	0.129	1.24	0.65	0.17	26.1
4	D	2.65	325	0.141	0.83	0.40	0.12	30
5	E	2.1	923	0.17	1.14	0.60	0.16	26.7
6	F	3	14448	0.011	1.14	0.45	0.13	28.9
7	G	2.4	1170	0.38	1.17	0.65	0.11	16.9
8	H	1.95	3228	0.22	0.77	0.47	0.09	19.1
9	I	1.5	12648	0.06	0.97	0.43	0.12	27.9
	Area-2	1.85	45935	0.06	4.28	0.548	0.27	49.27

σ : Standard deviation, CV%: Coefficient of variability

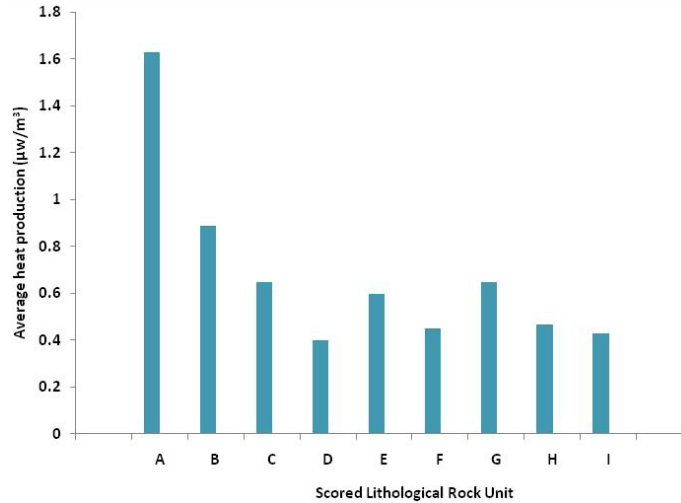


Figure 4. The average heat production (HP) for the nine lithological scored units

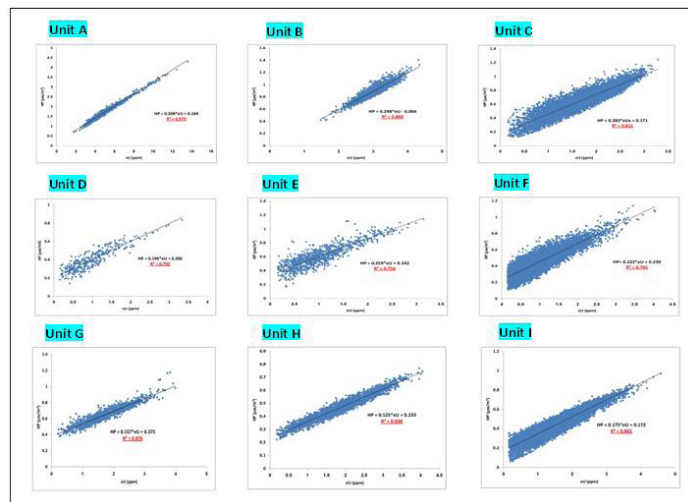


Figure 5. The relations between eU and HP for the nine lithological scored units

Weak correlations have been contrarily observed between both equivalent thorium (eTh) and potassium (K%) concentrations and the computed HP for the nine scored lithological units.

Fig.6-a shows high correlation between the average values of uranium and heat production HP ($R^2=0.885$), for the nine lithological units as compared with weaker correlations between the of thorium and HP (0.26) (Fig. 6-b) and between the averages of potassium and HP (0.025) (Fig.6-c).

The strong correlation between uranium eU and HP ($R^2=0.885$) indicates the dominance of uranium in producing heat, compared with thorium and potassium.

Multi-fractal technique with the use of concentration-number (C-N) model and log-log plots is proposed and used herein as a new approach to map and characterize the equivalent uranium (eU), the equivalent thorium (eTh), the potassium (K%), and the heat production (HP) parameters in the study Area-2. The use of this approach allows different environmental populations to be distinguished for those treated parameters.

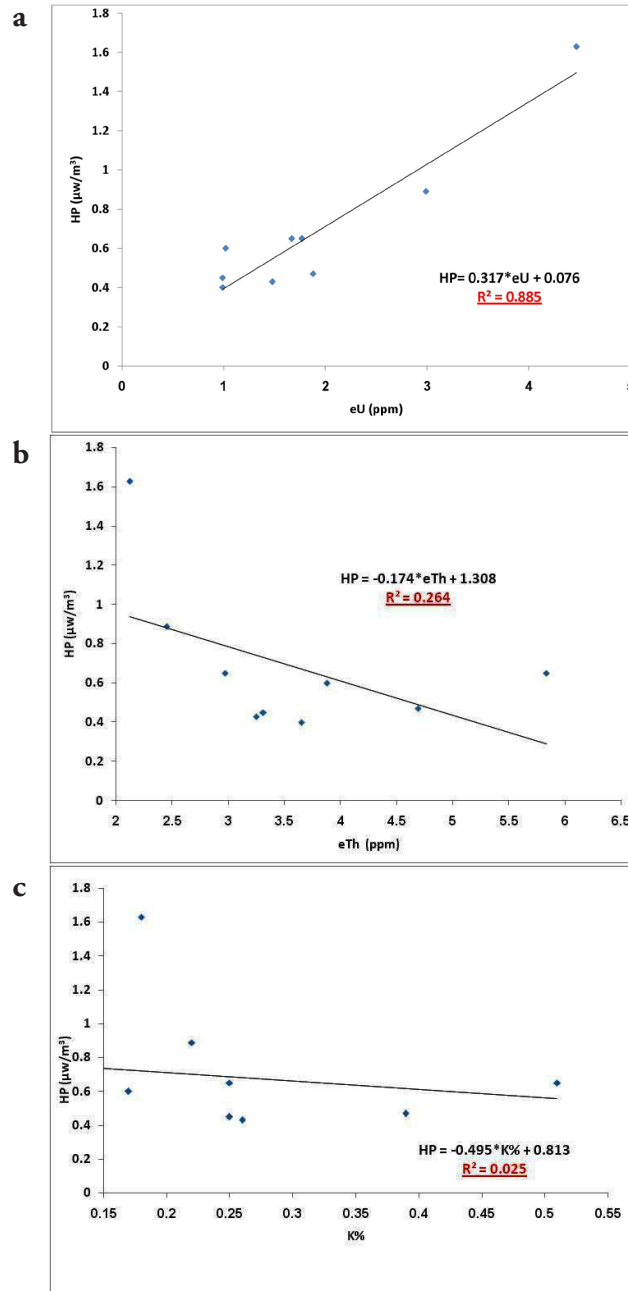


Figure 6. The relations between a: the averages of (eU and HP); b: the averages of (eTh and HP); and c: the averages of (K% and HP) for the nine lithological scored units.

The break points shown on the log-log plots for the different treated parameters are used as geological boundaries to distinguish between different kinds of environmental geology, and to show the passage from one environment to another.

Log-log plots of $N(\geq\mu)$ versus μ (eU, eTh, K% and HP) show straight line segments with different slopes-D corresponding to different radioactivity intervals.

The break points of those line segments are considered as thresholds. The geophysical populations of the treated parameters are therefore differentiated according to the linear segments and to the break points indicated in the log-log plots.

Based on the C-N log-log plot shown in Fig.8-a, the equivalent thorium log (eTh) indicates three threshold break points C1, C2, and C3 at 0.342, 0.549 and 0.793 respectively. The log (eTh) values indicate at those three locations an eTh of 2.20 ppm, 3.54 ppm, and 6.21 ppm respectively. The three indicated break points correspond to four eTh ranges as follows: The first range is less than 2.20 ppm, the second range is between 2.20 and 3.54 ppm, the third range is between 3.54 and 6.21 ppm, and the fourth range is bigger than 6.21 ppm.

According to those four eTh ranges, a map of the eTh distribution is established for the study Area-2 region as shown in Fig.8-b.

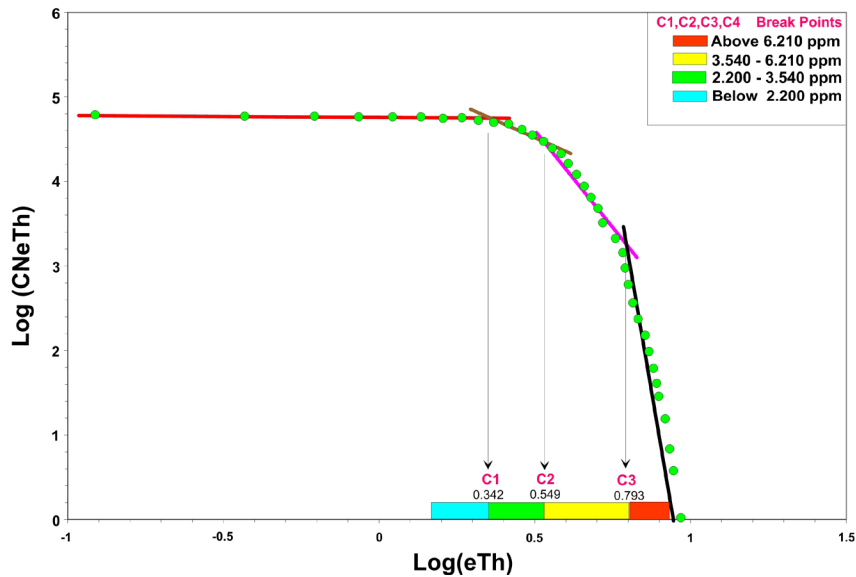


Figure 8-a. Log-log plot of eTh in the Area-2

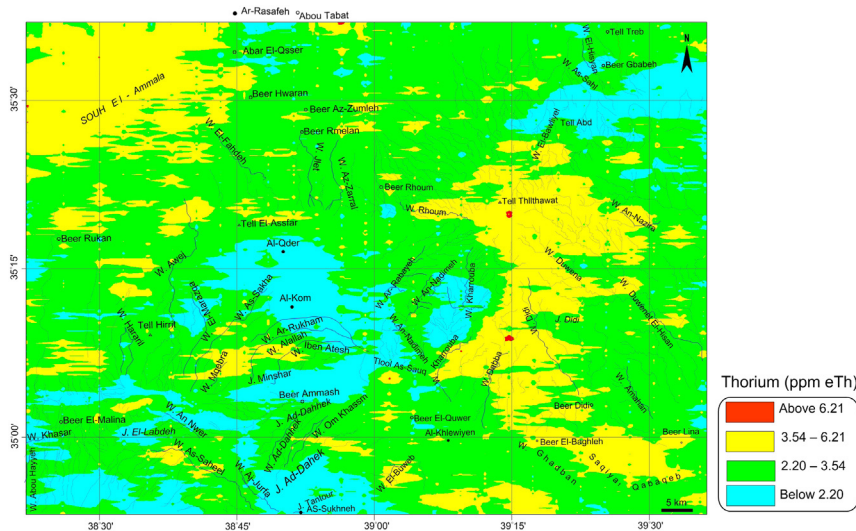


Figure 8-b. Equivalent thorium eTh map derived by C-N fractal modeling in Ar-Rassafeh Badyieh Area (Area-2), Syria

The first range represents the background, and the rest three ranges are of geological significance and could be interpreted in lithological context.

Based on the C-N log-log plot shown in Fig.9-a, the potassium log (K%) indicates four threshold break points C1, C2, C3 and C4 at -0.696, -0.59, -0.347 and -0.15 respectively. The Log (K%) values indicate at those four locations a K% of 0.20, 0.257, 0.449 and 0.710 respectively. The above four break points correspond to five K% ranges as follows: The first range is less than 0.20, the second range is between 0.20 and 0.257, the third range is between 0.257 and 0.449, the fourth range is between 0.449 and 0.710 and the fifth range is bigger than 0.710

According to those five K% ranges, a map of the K% distribution is established for the study Area-2 region as shown in Fig. 9-b.

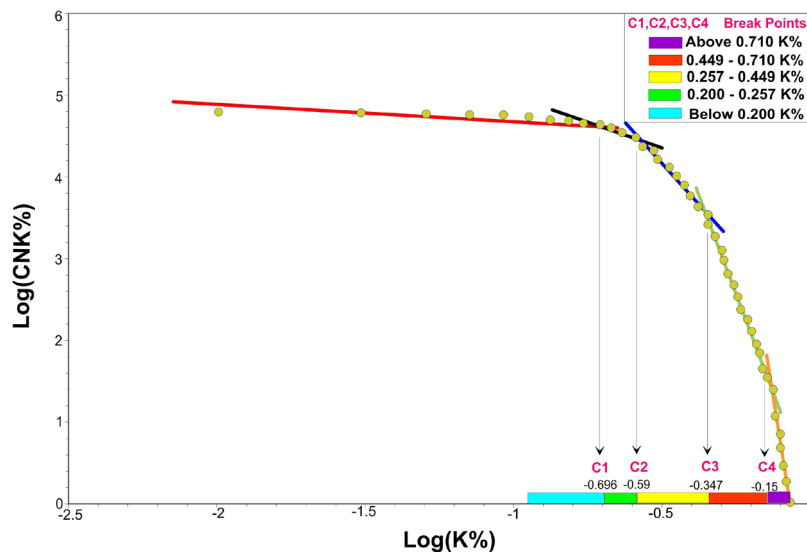


Figure 9-a. Log-log plot of K% in the Area-2

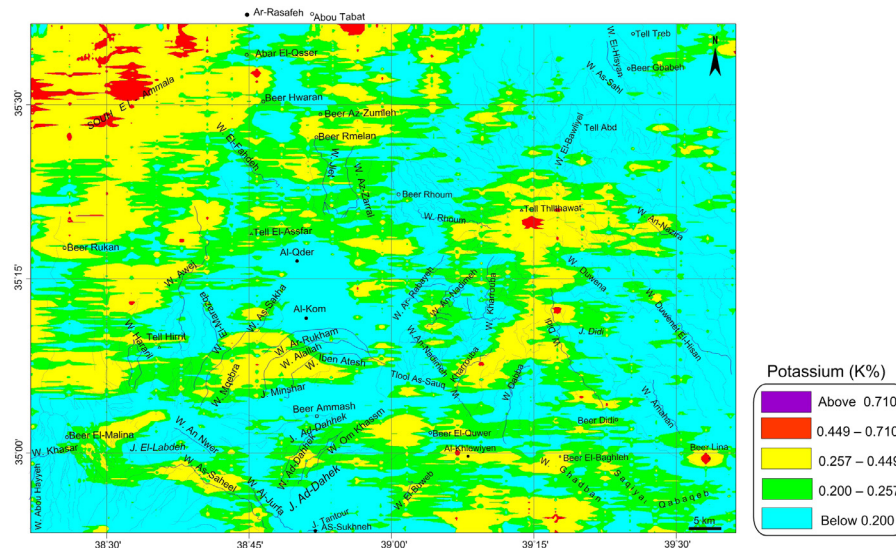


Figure 9-b. K% map derived by C-N fractal modeling in

Based on the C-N log-log plot shown in Fig.10-a, the radioactive heat production (HP) log (HP) shows four threshold break points C1, C2, C3 and C4 at -0.11, 0.19, 0.35 and 0.51 respectively.

The log (HP) values indicate at those four locations a heat production (HP) of 0.776, 1.549, 2.24 and 3.20 $\mu\text{w}/\text{m}^3$ respectively. Those four break points correspond to five radioactive heat production ranges as follows: The first range is less than 0.776 $\mu\text{w}/\text{m}^3$, the second range is between 0.776 and 1.549 $\mu\text{w}/\text{m}^3$, the third range is between 1.549 and 2.24 $\mu\text{w}/\text{m}^3$, and the fourth range is between 2.24 and 3.2 $\mu\text{w}/\text{m}^3$ and the fifth range is bigger than 3.20 $\mu\text{w}/\text{m}^3$. According to those five heat production (HP) ranges, a map of the HP distribution is established for the study Area-2 region as shown in Fig.10-b.

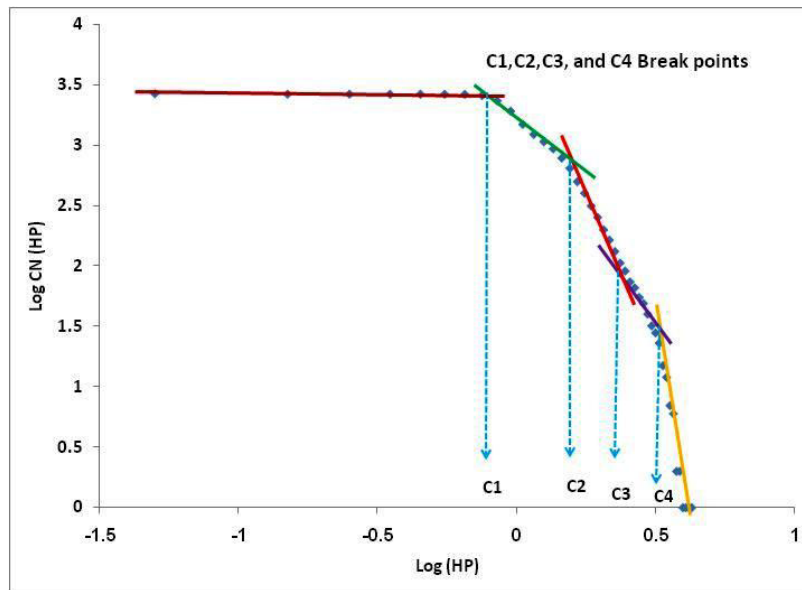


Figure 10-a. The C-N log-log plot for computed HP parameter in

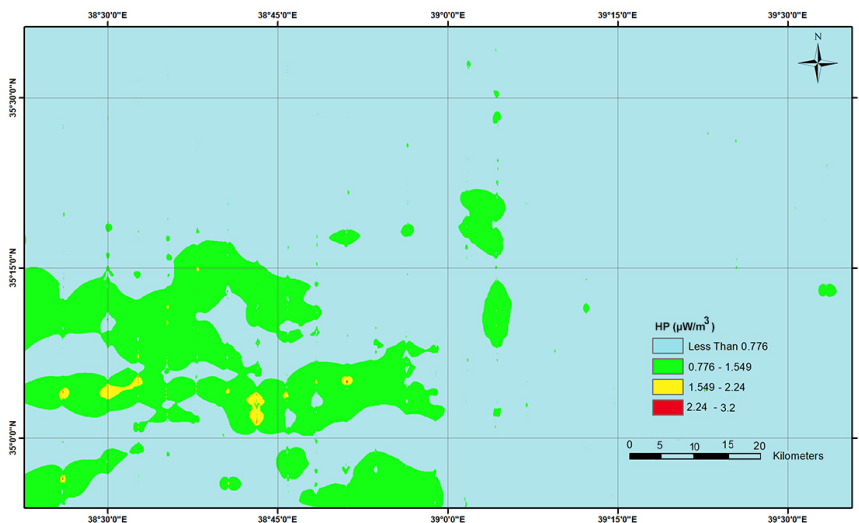


Figure 10-b. Heat production (HP) map derived by C-N fractal modeling in Ar-Rassafeh Badyieh Area (Area-2), Syria

The new heat production findings presented in the present study are important for future geothermal researches in the area study region. The mathematical multi-fractal modeling technique with C-N model and the log-log plots demonstrates its advantages in clearly distinguishing between different environmental populations for the treated parameters (eU, eTh, K% and HP).

CONCLUSIONS

The available aerial gamma-ray spectrometric data (eU, eTh, and K%) related to Area-2, Syria are used to compute and evaluate the radioactive heat production (HP) parameter in the study region. Two statistical techniques are adopted to interpret those aerial gamma-ray spectrometric data. The first one is the factor analysis technique, aimed at establishing the environmental lithological scored map of the study area. The already established scored map includes different geological environments represented by nine scored lithological units, which have been separately characterized for the heat production (HP) parameter. The second statistical analysis technique is a non linear multi fractal modeling technique, oriented towards distinguishing between different radioactive environmental populations for the treated parameters of eU, eTh, K% and HP. The C-N model and the log-log plots associated with this fractal modeling technique are proposed and applied as a new approach to map the measured equivalent uranium (eU), equivalent thorium (eTh), potassium (K%) and the computed heat production (HP) parameters. The environmental phosphatic units in the study Area-2, being the most rich in uranium concentration, have the highest heat production (HP) values, compared with other lithological units in the study area.

The new heat production findings presented in this paper are regarded as a basic and fundamental document for future geothermal and hydrocarbon researches in the study Area-2 region. The established heat production (HP) map will be used for characterizing the sedimentary basins from thermal evolution point of view and for temperature distribution modeling.

ACKNOWLEDGEMENTS

The author would like to thank Dr. I. Othman, General Director of Syrian Atomic Energy Commission, for his permission to publish this paper. The editor of *Geofisica Internacional* is cordially thanked for her revision, editing, remarks and suggestions to improve the submitted paper. The two anonymous reviewers are thanked for their critics and remarks that improve the paper quality. Mtra. Andrea Rostan, technical editor of the *Geofisica Internacional* is cordially thanked for her assistance during the different stages of this paper.

REFERENCES

- Afzal, P., Khakzad, A., Moarefvand, P., Rashidnejad Omran, N., Esfandiari, B., FadakarAlghalandis, Y., 2010. Geochemical anomaly separation by multifractal modeling in Kahang (Gor Gor) porphyry system. Central Iran. *J Geochem Explor* 104:34–46.
- Afzal, P., Fadakar Alghalandis, Y., Khakzad, A., Moarefvand, P., Rashidnejad Omran, N., 2011. Delineation of mineralization zones in porphyry Cu deposits by fractal concentration–volume modeling. *J Geochem Explor* 108:220–232.
- Afzal, P., Zia Zarifi, A., Bijan Yasrebi, A., 2012. Identification of U targets based on airborne radiometric data analysis by using multifractal modeling, Tark and Avanligh 1:50 000 sheets, NW Iran. *Nonlinear Proc Geoph* 19:283–289. doi:10.5194/npg-19-283.

Afzal, P., Mirzaei, M., Yousefi, M., Adib, A., Khalajmasoumi, M., Zia Zarifi, A., Foster, P., Yasrebi, A.B., 2016. Delineation of geochemical anomalies based on stream sediment data utilizing fractal modeling and staged factor analysis. *Journal of African Earth Sciences* 119, 139-149.

Afzal, P., Yasrebi A.B., Daneshvar Saein, L., Panahi, S., 2017. Prospecting of Ni mineralization based on geochemical exploration in Iran. *Journal of Geochemical Exploration* 181: 294-304.

Afzal, P., Jebeli, M., Pourkermani, M., Jafari Rad, A., 2018. Correlation between rock types and Copper mineralization using fractal modeling in Kushk-e-Bahram deposit, Central Iran. *Geopersia* 8: 131-141.

Agterberg, FP., 1995. Multifractal modeling of the size and grades of the giant and supergiant deposits. *Int Geol Rev* 37:1-8.

Asfahani, J., Al-Hent, R., Aissa, M., 2015. Favorable Uranium-Phosphate Exploration Trends Guided by the Application of Statistical Factor Analysis Technique On the Aerial Gamma Spectrometric Data in Syrian Desert (Area-1), Syria. *J. Earth Syst. Sci.* Indian Academy of Sciences. 125, No. 1, pp. 203-216.

Asfahani, J., Aissa, M., Al-Hent, R., 2016. Evaluation of radioactive environmental hazards in Area-3, Northern Palmyrides, Central Syria using airborne spectrometric gamma technique. *Applied Radiation and Isotopes* 107. 59-271.

Asfahani, J., Al-Hent, R., Aissa, M., 2018. Radioactive Characterization of Ar-Rassafeh Badyieh Area (Area-2), Syria By Using Statistical Factor Analysis Technique. *Contribution to Geophysics and Geodesy*, Vol. 48/2, (113-132).

Asfahani, J., 2018-a. Estimating and Mapping Radioactive Heat Production by Using Aerial Spectrometric Gamma and Fractal Modeling Techniques in Syrian Desert (Area-1), Syria. *Applied Radiation and Isotopes* 142, (194-202).

Asfahani, J., 2018-b. Multifractal approach for delineating uranium anomalies related to phosphatic deposits in Area-3, Northern Palmyrides, Syria. *Applied Radiation and Isotopes* 137, 225-235.

Asfahani, J., 2018-c. Heat Production Estimation by Using Natural Gamma Ray Well Logging Technique In Phosphatic Khneifis Deposit In Syria. *Applied Radiation and Isotopes* 145, 209-216.

Bíró, L., Polgári, M., Tóth, T., Vigh, T., 2012. Refinement of genetic and structural models of the Úrkút manganese ore deposit (W-Hungary, Europe) using statistical evaluation of archive data. *Cent. Eur. J. Geosci.* 4, 478-494. DOI: 10.2478/s13533-011-0079-2.

Birch, F., 1954. Heat from radioactivity. In *Nuclear Geology*; Wiley: New York, NY, USA, pp. 148-174.

Brady, R.J., Ducea, M.N., Kidder, S.B., Saleeby, J.B., 2006. The distribution of radioactive heat production as a function of depth in the Sierra Nevada Batholith, California. *Lithos* 86:229-244.

Bücker, C., Rybach, L., 1996. A simple method to determine heat production from gamma-ray logs. *Mar. Pet. Geol.* 13, 373-375.

Daneshvar Saein, L., Afzal, P., 2017. Correlation between Mo mineralization and faults using geostatistical and fractal modeling in porphyry deposits of Kerman Magmatic Belt, SE Iran. *Journal of Geochemical Exploration* 181: 33-343.

Deming, D., 1994. Estimation of the thermal conductivity anisotropy of rock with application to the determination of terrestrial heat flow. *J. Geophysical Research*, 99(B11), 22087:p.91.

Dill, H.G., 2009. A comparative study of uranium-thorium accumulation at the western edge of the Arabian Peninsula and mineral deposits worldwide: *Arabian Journal of Geosciences*, DOI 10.1007/s12517-009-0107-4.

Fernandez, M., Marzan, I., Correia, A., Ramalho, E., 1998. Heat flow, heat production and lithosphere thermal regime in the Iberian Peninsula. *Tectonophysics* 291, 29-53.

Hassanpour, S., Afzal, P., 2013. Application of concentration-number (CN) multifractal modelling for geochemical anomaly separation in Haftcheshmeh porphyry system, NW Iran. *Arab J Geosci* 6:957-970. doi:10.1007/s12517-011-0396-2.

JICA (Japan International Cooperation Agency), 1996. The study on water resources development the northwestern and central basins in the Syrian Arab Republic (Phase I), progress report, December 1996. NIPPON KOEI Co., LTD. SANYU CONSULTANTS INC. Tokyo, Japan.

Jubeli, Y. M., 1990. Uranium exploration in Syria SY/86/005. Final report, *Atomic Energy Commission of Syria, Damascus*.

- Ketcham, R.A., 1996. Distribution of heat-producing elements in the upper and middle crust of southern and west central Arizona: evidence from core complexes. *J Geophys Res* 101:13611–13632.
- Khalajmasoumi, M., Lotfi, M., Afzal, P., Sadeghi, B., Memar Kochebagh, A., Khakzad, A., Ziazarifi, A., 2015. Delineation of the radioactive elements based on the radiometric data using concentration–area fractal method in the Saghand area, Central Iran. *Arabian Journal of Geosciences* 8: 6047–6062.
- Kumar, P.S., Reddy, G.K., 2004. Radioelements and heat production of an exposed cross-section of Archaean crust, Dharwar craton, south India, *Earth Planet. Sci Lett* 224:309–324
- Li, C., Ma, T., Shi, J., 2003. Application of a fractal method relating concentrations and distances for separation of geochemical anomalies from background. *J Geochem Explor* 77:167–175.
- Litak, R.K., Barazangi, M., Brew, G., Sanaf, T., Al-Emam, A., 1998. Structure and evolution of the petrol ferrous Euphrates graben system, south east Syria. *Aapg belle ton*, Vol. 82, No. 6, p. 1173-1190.
- Mandelbrot, B.B., 1983. *The Fractal Geometry of Nature*, W. H. Freeman, San Fransisco, 468 pp.
- Mohammadi, A., Khakzad, A., Rashidnejad Omran, N., Mahvi, M.R., Moarefvand, P., Afzal, P., 2013. Application of number-size (N-S) fractal model for separation of mineralized zones in Dareh-Ashki gold deposit, Muteh Complex, Central Iran. *Arabian Journal of Geosciences* 6: 4387-4398.
- Richardson, K.A., Killeen, P.G., 1980. Regional radiogenic heat production mapping by airborne gamma-ray spectrometry. In: *Current Research, Part B*, Geological Survey of Canada, pp. 227-232. Paper 80-1B.
- Riso., 1987. Aerial gamma-ray in Syria SYR/87/005. *Technical report, Riso National Laboratory, Roskilde, Denmark*.
- Rybach, L., 1976. Radioactive heat production in rocks and its relation to other petrophysical parameters. *Pure Appl. Geophys.* 114, 309-318.
- Rybach, L., 1976. Radioactive heat production: A physical property determined by the chemistry of rocks. In *The Physics and Chemistry of Minerals and Rocks*; Stems, R.G.J., Ed.; Wiley-Interscience: New York, USA, pp. 309–318.
- Rybach, L., 1988. Determination of heat production rate. In: Haenel R, Rybach L, Stegena L (eds) *Handbook of terrestrial heat-flow density determination*. Kluwer, Dordrecht, pp 125–142.
- Sadeghi, B., Moarefvand, P., Afzal, P., Yasrebi, A.B., Daneshvar Saein, L., 2012. Application of fractal models to outline mineralized zones in the Zaghia iron ore deposit, Central Iran. *Journal of Geochemical Exploration* 122, 9-19.
- Salem, A., El Sirafy, A., Aref, A., Ismail, A., 2005. Mapping radioactive heat production from airborne spectral gamma-ray data of Gabal Duwi area, Egypt. In: *Proceedings World Geothermal Congress, Antalya, Turkey*, pp. 24e29.
- Shtiza, A., Tashko, A., 2009. Appropriate sampling strategy and analytical methodology to address contamination by industry: part 1 conceptual model of a sampling design and sampling types. *Cent. Eur. J. Geosci.* 1, 193–206.
- Technoexport., 1967. Explanatory notes on the geological map of Syria, mineral deposits and underground-water resources. *Ministry of Geology, USSR, 1967*.
- Thompson, P.H., Judge, A.S., Charbonneau, B.W., Carson J.M., Thomas, M.D., 1996. Thermal regimes and diamond stability in the Archean slave province, Northwestern Canadian Shield, District of Mackenzie, Northwest Territories. In: *Current Research, 96e1E*, Geological Survey of Canada, pp. 135e146.
- Wang, Q.F., Deng, J., Liu, H., Wang, Y., Sun, X., Wan, L., 2011. Fractal models for estimating local reserves with different mineralization qualities and spatial variations. *J. Geochem. Explor.* 108, 196–208. doi:10.1016/j.gexplo.2011.02.008.
- Yousef, M., 2016. Estimating and interpretation of radioactive heat production using airborne gamma-ray survey data of Gabal Arrubushi area, Central Eastern Desert, Egypt. *Journal of African Earth Sciences* 114, 67-73.
- Zuo, R., 2011. Decomposing of mixed pattern of arsenic using fractal model in Gangdese belt, Tibet, China. *Appl Geochem* 26:S271–S273 Davis JC (2002) *Statistics and data analysis in geology*, 3rd ed. John Wiley & Sons Inc, New York.

<https://doi.org/10.22201/igeof.00167169p.2022.61.1.2126>

MINERAL LITHOTYPE IDENTIFICATION ON THE ANDRILL AND-2A DRILLCORE, ANTARCTICA BY USING TERNARY MINERAL ROCK PHYSICS TEMPLATES BUILT FROM A SELF-CONSISTENT APPROACH

Jaime Meléndez-Martínez¹, Rubén Nicolás-López², Oscar C. Valdiviezo-Mijangos^{3*}

Received: February 10, 2021; accepted: October 4, 2021; published on-line: January 1, 2022.

RESUMEN

En este trabajo, los valores de densidad volumétrica húmeda ρ_{WBD} y de velocidad onda compresional V_p obtenidas a lo largo del núcleo de perforación AND-2A son graficados sobre plantillas ternarias de física de rocas (Rock Physics Templates, RPTs) construidas a partir de un modelo micromecánico autoconsistente (Self-Consistent, SC) con el fin de determinar las tendencias en las propiedades elásticas del núcleo que permitan ayudar a identificar los litotipos minerales y en consecuencia identificar también las características litológicas presentes a lo largo de los 1138 m. de longitud del núcleo. Las propiedades elásticas de los tres minerales dominantes presentes en el núcleo de perforación (arcillas mixtas, cuarzo y calcita); así como el fluido que satura su espacio poroso (salmuera) se utilizaron como insumos del modelo autoconsistente. La litología interpretada es también comparada con la que se obtiene a partir del análisis de los valores de ρ_{WBD} y V_p utilizando gráficos cruzados de densidad-velocidad de tipo Gardner. Los resultados que se obtienen usando los métodos SC y de Gardner concuerdan con las principales litologías presentes a lo largo del núcleo AND-2A reportadas en la literatura científica. Nuestros resultados también son consistentes con la descripción litológica de seis muestras de roca obtenidas a diferentes profundidades del núcleo AND-2A. Estos resultados sugieren que las predicciones del método autoconsistente podrían ser útiles para ayudar a identificar litología en perforaciones científicas en donde las propiedades elásticas a lo largo de la pared del pozo de perforación podrían existir en intervalos en los que no se recuperaron muestras del núcleo de perforación.

Además, incluso cuando las propiedades físicas elásticas se obtienen a través de mediciones en núcleos, el método autoconsistente también es útil porque la litología a veces puede ser difícil de determinar solamente a partir del análisis visual; de modo que el estudio de las propiedades físicas del núcleo puede proporcionar mayor información.

PALABRAS CLAVE: plantillas de física de rocas, método auto consistente, sedimentos antárticos, núcleo de perforación AND-2A y relación de Gardner.

*Corresponding author at ovaldivi@imp.mx

¹Instituto Mexicano del Petróleo
Eje Central Lázaro Cárdenas Norte 152, Gustavo A. Madero,
San Bartolo Atepehuacan, 07730 Mexico City, Mexico.
Jaime Meléndez-Martínez, email: jaimem@imp.mx

²Instituto Mexicano del Petróleo
Eje Central Lázaro Cárdenas Norte 152, Gustavo A. Madero,
San Bartolo Atepehuacan, 07730 Mexico City, Mexico.
División de estudios de Posgrado de la Facultad de Ingeniería,

Universidad Nacional Autónoma de México.
Ciudad Universitaria, Delegación Coyoacán, 04510, Mexico City,
Mexico.
Rubén Nicolás-López, email: rnlopez@imp.mx

³Instituto Mexicano del Petróleo
Eje Central Lázaro Cárdenas Norte 152, Gustavo A. Madero,
San Bartolo Atepehuacan, 07730 Mexico City, Mexico.
Instituto Politécnico Nacional, ESIA Ticomán
Calz. Ticomán 600, San José Ticomán, Gustavo A. Madero, 07340
México City, Mexico

ABSTRACT

In this work, wet bulk density ρ_{WBD} and compressional wave velocity V_p core log data obtained along the AND-2A drillcore are plotted on density-velocity ternary mineral Rock Physics Templates (RPTs) built from a Self-Consistent (SC) micromechanics modelling with the purpose to determine data trends that allow us to assist in identifying mineral lithotypes and lithological features throughout the 1138 m length of the drillcore. The elastic properties of the three dominant minerals present in the drillcore (mixed clays, quartz, and calcite) and the pore-filling fluid (brine) were used as input data for the SC model. The interpreted lithology is then compared to that obtained from the analysis of the AND-2A drillcore ρ_{WBD} and V_p log data using Gardner type density-velocity cross plots. Results from both the SC and Gardner methods are in good agreement with the main lithologies present in the AND-2A drillcore already reported in the scientific literature. Our findings also agree well when compared to the lithological description of six selected rock samples obtained at different depths on the AND-2A drillcore. These results suggest that the proposed SC approach could be helpful to assist to identify lithology in scientific drill holes where downhole elastic properties may exist over intervals where portions of the drillcore were not recovered. Furthermore, even when elastic property data sets come from measurements on cores, the SC approach is likewise useful because, from visual analysis alone, lithology can sometimes be difficult to determine, and additional information from the analysis of the elastic properties may provide more insight.

KEY WORDS: rock physics templates, self-consistent method, Antarctic sediments, AND-2A drillcore and Gardner's relationship.

INTRODUCTION

Antarctica has endured repeated ice sheets since the Cenozoic, while continuous glaciations have been experienced in the Northern Hemisphere since the beginning of the Pliocene (Wilson *et al.*, 2012). Therefore, broad areas are now covered with glacially deposited sediments. Populations settled in such areas, mainly in the northern hemisphere, obtain water from, and place waste in these sediments (Stephenson *et al.*, 1988). Consequently, knowledge of the different mineral lithotypes, and therefore, the lithology present in these geological materials is important for both the development of engineering projects and for geophysical assessments. Despite their significance, there is a scarcity of information about their lithological features since such sediments are frequently located in remote areas (Brink & Jarrard, 1998; Niessen & Jarrard, 1998; Niessen *et al.*, 1998) making it difficult to obtain appropriate geophysical data sets used to describe the lithology of these sediments. In this sense, we make use of the existence of density and velocity core log data obtained from the AND-2A to assist in identifying lithology using ternary Rock Physics Templates. RPTs are built using rock physics modelling with the purpose of relating the physical properties of rocks to their particular geological features and to identify fluid content (Close *et al.*, 2012). Here, we attempt to use ternary mineral RPTs to relate the AND-2A drillcore's elastic properties to mineral lithotypes (mineral assemblage facies), and then to lithology. The AND-2A drillcore was obtained by the ANtartic DRILLing project (ANDRILL) as part of the Southern McMurdo Sound Project (SMS) (Florindo *et al.*, 2008-2009). Drilling started over a sea ice platform (8.5 m thick) while lying on the surface of a 380 m seawater column and finished at 1138 meters beneath the seafloor [mbsf] (Wonik *et al.*, 2008-2009). The elastic properties corresponding to the AND-2A drillcore that are used in this contribution are the ρ_{WBD} and the V_p core log data, while the ternary mineral diagrams

are generated from a micromechanics SC modelling using the scheme implemented by Sabina and Willis (1988). This SC scheme seeks to compute the effective elastic properties of a heterogeneous isotropic rock composite assuming that the composite contains an isotropic mineral matrix embedded with n isotropic inclusions (minerals and the fluid that saturates the porous space of the rock). As such, in our case, the heterogeneous isotropic composite represents the AND-2A drillcore. This SC approach has been already implemented to calculate the elastic properties of gas-oil shale systems (Valdiviezo-Mijangos & Nicolás-Lopez, 2014; Nicolás-López & Valdiviezo-Mijangos, 2016; Lizcano-Hernández *et al.*, 2018; Nicolás-López *et al.*, 2020; López-Lena-Estrada *et al.*, 2021), to compute the elastic properties of shale rock samples from diverse geological origins (Nicolás-López *et al.*, 2019) and, to estimate attenuation effects and dispersion of velocities on sandstones saturated with brine (Valdiviezo-Mijangos *et al.*, 2020).

The ternary mineral RPTs that we used here to study the AND-2A drillcore were built in terms of the elastic properties of mixed clays, quartz, and calcite. We chose these minerals because the AND-2A drillcore mainly contains siliciclastic sediments consisting of diamictite [a poorly sorted sedimentary rock, characteristic of glacial sediments that contain clasts of various sizes ranging from clay to boulders embedded in either a sand or mud matrix], sandstones, and mudstones which are cemented by calcareous minerals (Fielding *et al.*, 2008; Hunze *et al.*, 2013; Iacoviello *et al.*, 2015). Furthermore, smectite and illite are the main clay minerals present along the drillcore with a minor presence of kaolinite and chlorite (Iacoviello *et al.*, 2012). We also consider that the rock's porous space is brine saturated. As such, brine is considered as an inclusion form.

In the next section, a summary of the SC method is first given, followed by a description of the methodology used to obtain the core logging data from the AND-2A drillcore. Results are then compared to the lithology interpreted from the implementation of Gardner-type density-velocity cross plots (Gardner *et al.*, 1974). Results from SC and Gardner methods are also compared to the lithology reported by Fielding *et al.* (2008) and with the visual description of six selected rock specimens that were trimmed off the AND-2A drillcore at different depths.

METHODS

SELF-CONSISTENT METHOD

In the SC scheme proposed by Sabina and Willis (1988), the effective elastic properties of the AND-2A drillcore such as both the bulk and the shear moduli, κ_{eff} and μ_{eff} , and the wet bulk density $\rho_{WBD_{eff}}$ can be modelled using the following equations:

$$\kappa_{eff} = \kappa_{n+1} + \sum_{r=1}^n \frac{\alpha_r (\kappa_r - \kappa_{n+1})}{1 + 3(\kappa_r - \kappa_{eff}) / (3\kappa_{eff} + 4\mu_{eff})}, \quad (1)$$

$$\mu_{eff} = \mu_{n+1} + \sum_{r=1}^n \frac{\alpha_r (\mu_r - \mu_{n+1})}{1 + 6(\mu_r - \mu_{eff})(\kappa_e + 2\mu_{eff}) / [5\mu_{eff}(3\kappa_{eff} + 4\mu_{eff})]}, \quad (2)$$

$$\rho_{WBD\text{eff}} = \rho_{n+1} + \sum_{r=1}^n \alpha_r (\rho_r - \rho_{n+1}). \quad (3)$$

In equations (1) through (3), κ_{n+1} , μ_{n+1} and ρ_{n+1} are respectively both the bulk and shear moduli and the density of the mineral matrix while the bulk modulus, the shear modulus, the density and the volume fraction for a given inclusion r are represented by κ_r , μ_r , ρ_r and α_r where $r=1,2,\dots,n$. If the volume fraction of the mineral matrix is represented by α_{n+1} , then it follows that

$$\sum_{r=1}^{n+1} \alpha_r = 1. \quad (4)$$

Later, equation (4) can be rewritten as follows: $\sum_{r=1}^{n+1} \alpha_r = \alpha_r^{\text{sol}} + \alpha_r^{\text{fl}} = \alpha_r^{\text{sol}} + \phi = 1$, where both the volume fraction of the solids (minerals) and the pore fluid are respectively represented by α_r^{sol} and α_r^{fl} . For instance, ϕ is the void fraction of the rock that is saturated with fluid. As above mentioned, in this work, the solids are represented by mixed clays, quartz, and calcite while the saturating fluid is brine. In the SC approach, the matrix can be represented by any of these three main minerals. Thus, when any one of these minerals acts as the matrix, the other two remaining minerals and the brine act as the inclusions. The physical properties of the minerals and the brine used as input data in equations (1) through (3) are shown in Table 1 (Mavko *et al.*, 2009). These equations can be easily implemented using any encoding software. However, equations (1) and (2) must be iteratively solved. Lizcano-Hernández *et al.* (2018) and López-Lena-Estrada *et al.* (2021) portray flowcharts that explain the solution of these equations using the fixed point technique. Therefore, $V_{p\text{eff}}$ can be

$$\text{simply estimated as } V_{p\text{eff}} = \left(\frac{K_{\text{eff}} + \mu_{\text{eff}}}{\rho_{WBD\text{eff}}} \right)^{1/2}.$$

Table 1. Physical properties of the minerals and the fluid used as input in the SC modelling (Mavko *et al.*, 2009): * values for mixed clays, ** values calculated at atmospheric pressure, at 20 °C and 3.5% salinity.

Mineral or fluid	ρ_r [gr/cm3]	V_p [km/s]	V_s [km/s]
Clays	2.6*	3.41*	1.63*
Quartz	2.65	6.05	4.09
Calcite	2.71	6.64	3.44
Brine	1.02**	1.52**	-----

AND-2A DRILLCORE SETTINGS: PHYSICAL CHARACTERISTICS

Core logging data includes the wet bulk densities ρ_{WBD} and the compressional wave velocities V_p that were estimated with the Geotek Multi-Sensor Core-Logger (MSCL) system [<http://www.geotek.co.uk/>].

Compressional travel times were measured across the core diameter by leading the AND-2A drillcore through a couple of pulser-receiver P-wave Acoustic Roller Contact (ARC) piezo-electric ceramic transducers (230 kHz of central frequency). The core diameter was determined by the displacement

of the acoustic rollers as they travelled over the core. This technique allows the estimation of V_p profiles by dividing the measured travel times by the measured core diameter [see Dunbar *et al.* (2009) for additional details].

Then, a pair of ^{137}Cs gamma-ray γ source and detector mounted across the drillcore provide a core wet bulk density ρ_{WBD} profile. Briefly, gamma rays travelling through the composite lose energy as they are dispersed by the electrons present in the medium. The latter leads to the detected radiation being diminished. This energy loss can be associated with the density of the electrons ρ_e that correspond to the detected gamma-ray beam as follows:

$$\rho_e = 2\rho_{WBD} \frac{Z}{A}, \quad (5)$$

where the atomic number Z and the molecular weight A of the medium can be taken as $\frac{Z}{A} = \frac{1}{2}$ with negligible error for most rocks (Keller, 1988).

RESULTS AND DISCUSSION

Figure 1(a) portrays density-velocity ternary mineral RPTs built by using the SC method. In these RPTs, the upper triangle is representative of a solid heterogeneous rock $\alpha_r^f = \phi = 0\%$ which vertices are defined as CL100% (clay), CA100% (calcite) and QR100% (quartz) while the vertices of the modelled triangles with brine (BR) filling void fractions of 20% and 40% are defined as BR20%+CL80%, BR20%+CA80% and BR20%+QR80%; and BR40%+CL60%, BR40%+CA60% and BR40%+QR60% respectively.

Figure 1(b) displays the full AND-2A drillcore log data overlapped on the ternary mineral RPTs shown in Figure 1(a). Our mineral lithotype interpretation is carried out in terms of the areas related to the elastic responses of the minerals. In this sense, we identify in Figure 1(b) the following mineral lithotypes: argillaceous lithotype, clay-rich siliceous lithotype and siliceous lithotype (Gamero-Diaz *et al.*, 2013). Note that the contribution of calcite to the observed elastic properties of the drillcore is negligible, as also pointed out by Staudigel *et al.* (2018) where calcite was found to be a rare constituent of the lithology of the AND-2A instead of occasionally appearing as veins or pore-filling cement.

Also, note that, while mineral ternary diagrams attempt to model the AND-2A drillcore's elastic response considering the presence of mixed clays, quartz and calcite, the data points lying outside the ternary mineral RPTs could indicate intervals with the presence of minerals whose elastic properties may be significantly different from mixed clays, quartz and calcite, since most rocks are made up of more than three dominant minerals. However, observed high V_p (≥ 4.5 km/s) and ρ_{WBD} (≥ 2.6 gr/cm³) in glacial sediments can also be related to the existence of large limestones (Niessen & Jarrard, 1998; Niessen *et al.*, 1998).

Figure 2 portrays a log density- log velocity cross plot showing the lithotype interpretation of the AND-2A drillcore data carried out by using the relationship between density (ρ) and compressional velocity (V_p) proposed by Gardner (Gardner *et al.*, 1974)

$$\rho = \alpha V_p^{0.25}. \quad (6)$$

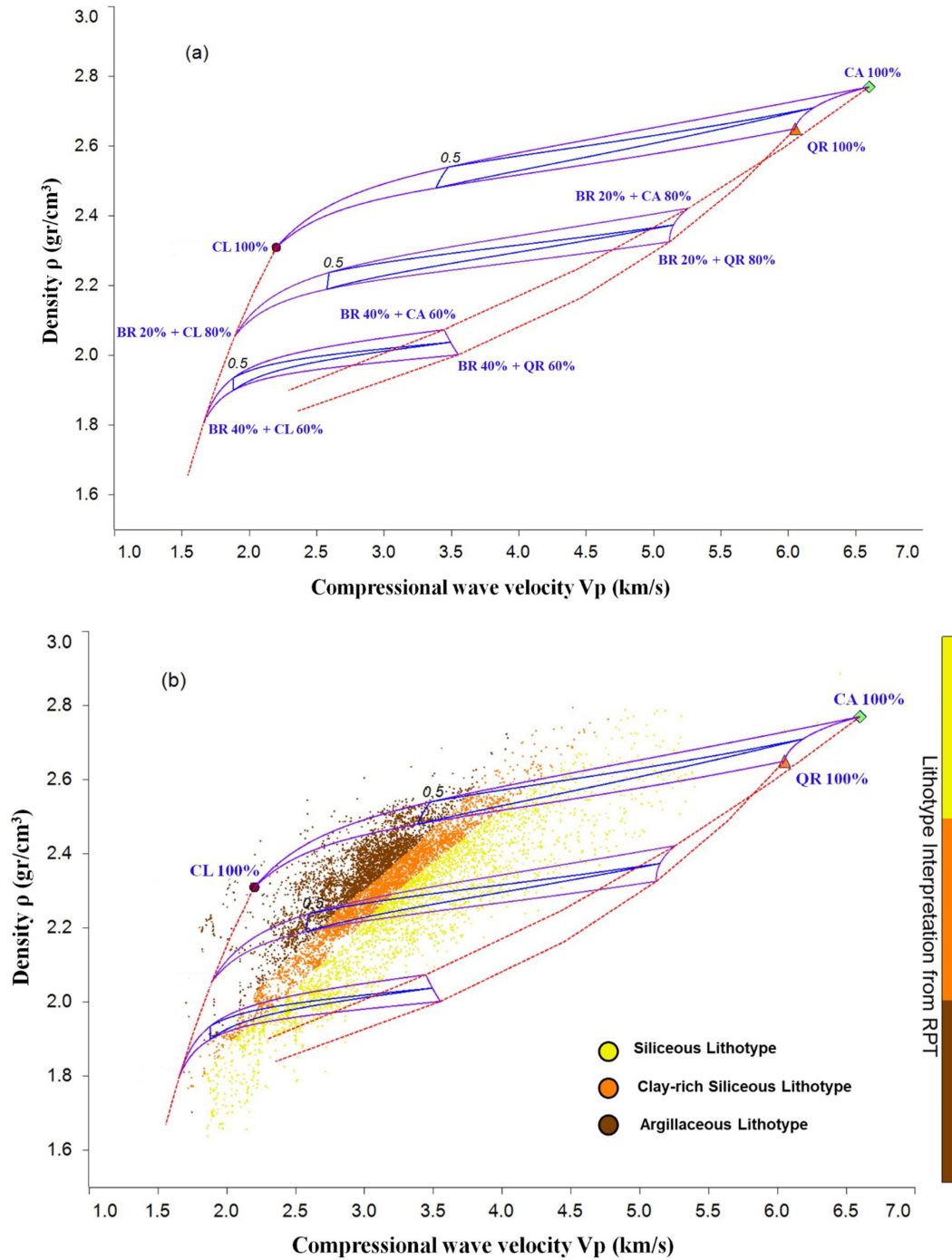


Figure 1 (a). Density - velocity ternary mineral RPTs built from the SC approach to model the AND-2A drillcore's elastic response. These RPTs integrate the mineralogy and the brine saturation at 0%, 20% and 40% void fractions resulting in vertices for the upper triangle defined as CL100% (clay), CA100% (calcite), and QR100% (quartz) while the vertices of the middle and lower triangles are defined as BR20%+CL80%, BR20%+CA80% and BR20%+QR80%; and BR40%+CL60%, BR40%+CA60% and BR40%+QR60% respectively. (b) AND-2A drillcore's mineral lithotype interpretation using the RPT portrayed in Figure 1(a). The volume fractions corresponding to the vertices of middle and lower are not shown to improve visualization of the data points. The lithotype zones are related to the mineral elastic response. Three mineral lithotypes are identified: argillaceous lithotype, clay-rich siliceous lithotype and siliceous lithotype.

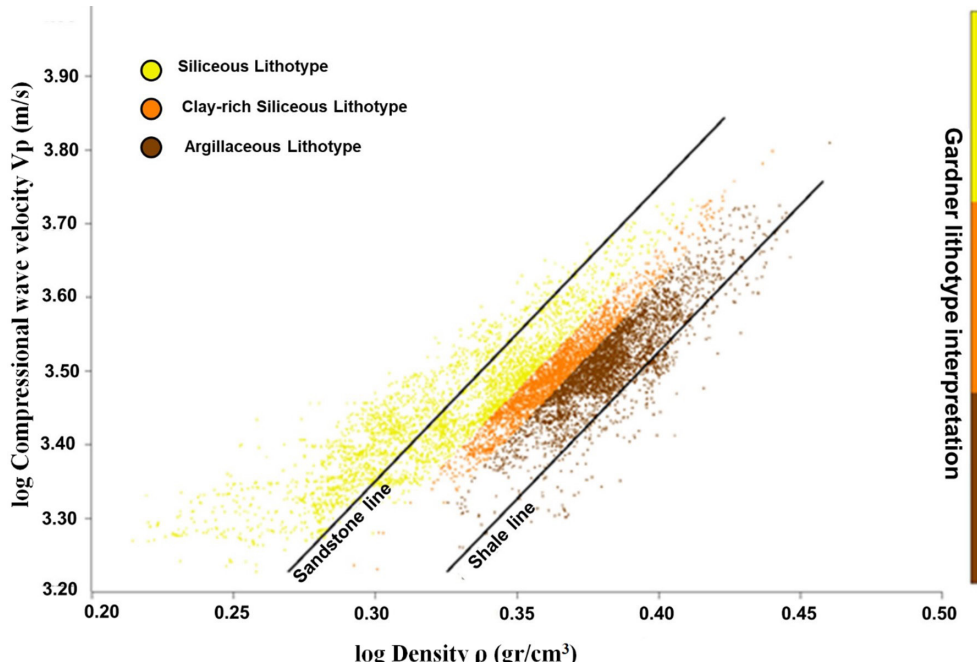


Figure 2. Lithotype interpretation of the AND-2A Drillcore by using Gardner type density-velocity cross plots. This figure shows the shale line, $\rho = 1.75V_p^{0.25}$, which defines points with high clay content, while the sandstone line, $\rho = 1.66V_p^{0.25}$ represents points with high quartz content. In this image, three mineral lithotypes are also identified: argillaceous lithotype, clay-rich siliceous lithotype and siliceous lithotype.

Typical values for coefficient α are $\alpha = 1.66$ for sandstones and $\alpha = 1.75$ for shales (Mavko *et al.*, 2009). Thus, the shale line, $\rho = 1.75V_p^{0.25}$, defines trend points for argillaceous lithotypes, while the sandstone line, $\rho = 1.66V_p^{0.25}$, represents trend points for siliceous lithotypes. Therefore, the clay-rich siliceous lithotype represents the clay to quartz content transition. Figure 3 displays the mineral lithotype sequences obtained from the interpretation of the elastic response in Figures 1(b) and 2. In the AND-2A drillcore the argillaceous lithotype indicates the presence of a variety of argillaceous rocks such as muddy diamictite, mudstone, and claystone while the clay-rich siliceous lithotype is related to clay-rich siltstones. On the other hand, the siliceous lithotype is associated with siliceous rocks, mainly including sandy diamictite, sandstone and sandy conglomerate. Table 2 shows results from Figure 3 compared to the main lithological features corresponding to the LSU's reported by Fielding *et al.* (2008). These LSUs, as portrayed in Figure 3, cover fourteen depth intervals [mbsf] along the AND-2A [also, LSU 8 is divided into four sub-units]. However, the lithological description of the first LSU [0 – 37.7 mbsf] is not included in our work due to the lack of data on this depth interval.

Figures 4 and 5 present photographs and thin sections of six selected samples obtained from the AND-2A. These samples are labelled in terms of the depth interval [mbsf] where they were located and they were chosen as being representative of the fine to coarse grain textures found along the three different geological ages of the AND-2A Drillcore (Acton *et al.*, 2008): lower Miocene (1138.54 to 800 mbsf), middle Miocene (800 to 223 mbsf), and upper Miocene to more recent intervals (223 to 0.0 mbsf). Table 3 shows the lithological visual description of these samples compared to the lithological features obtained from the SC and Gardner methods. Qualitative X-Ray Diffraction (XRD)

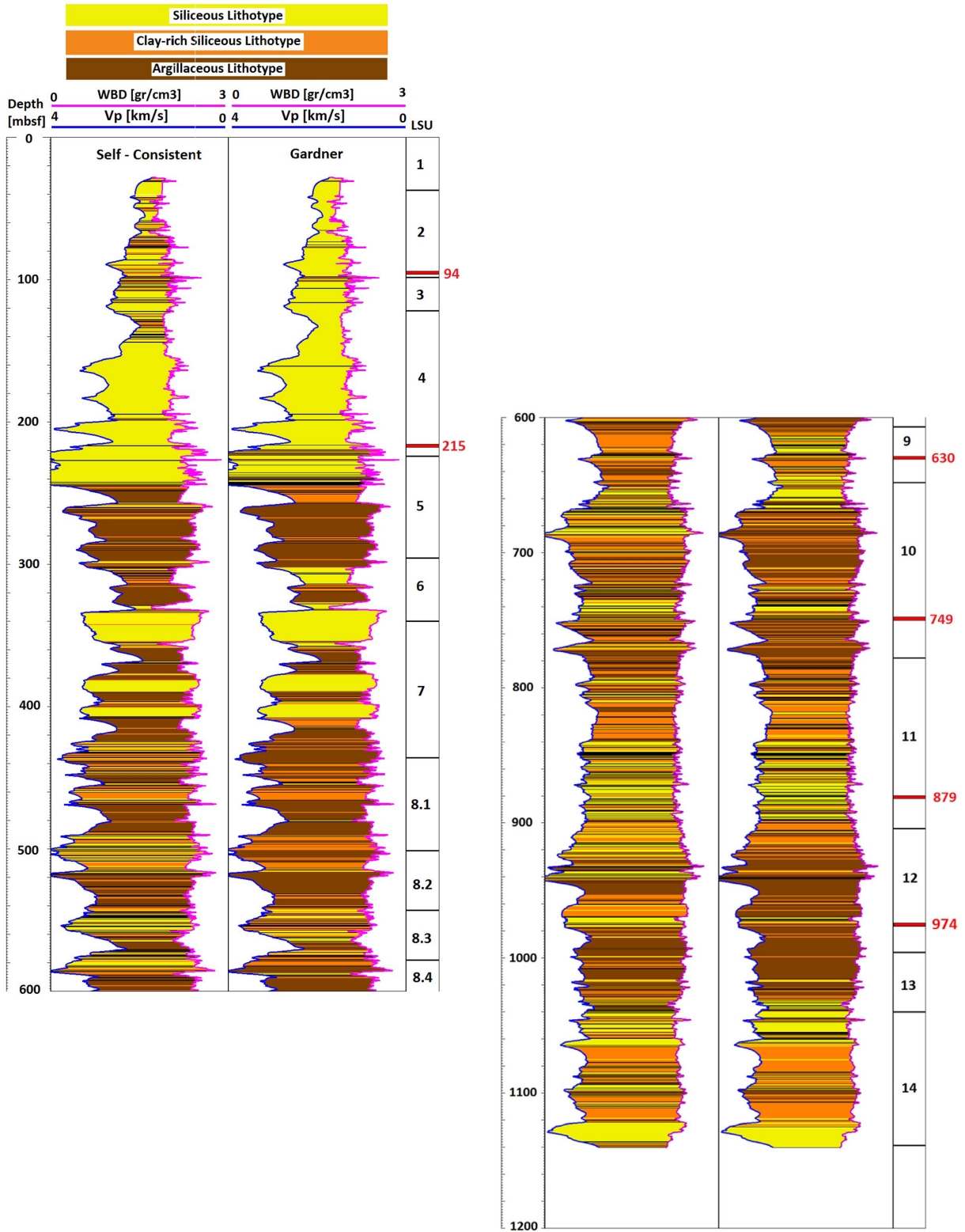


Figure 3. This figure shows the mineral lithotype sequences of the AND-2A drillcore identified from the interpretation of Figures 1 (b) and 2 along with the depth intervals related to the fourteen LSU covering the AND-2A. The red markers indicate the position in depth of the six selected samples.

Table 2. The lithological description of the AND-2A obtained from SC and Gardner methods compared to the main lithologies along the LSUs reported by Fielding *et al.* (2008).

LSU	Depth interval (mbsf)	Lithologies		
		Self-Consistent	Gardner	Fielding et al 2008
2	37.07 – 98.47	Mainly siliceous rocks with interbedded clay-rich siltstones and argillaceous rocks	Mainly siliceous rocks with the sparse presence of clay-rich siltstones and argillaceous rocks	Sandy diamictite interbedded with sandstone, siltstone and sandy conglomerate
3	98.47 – 122.86	Mainly siliceous rocks with interbedded clay-rich siltstones and argillaceous rocks	Mainly siliceous rocks with the sparse presence of clay-rich siltstones and argillaceous rocks	Sandstone and sandy conglomerate
4	122.86 – 224.82	Mainly siliceous rocks with intervals containing clay-rich siltstones and argillaceous rocks	Mainly siliceous rocks	Sandy to silty diamictite, sandstone and siltstone
5	224.82 – 296.34	Argillaceous rocks and minor siliceous rocks	Argillaceous rocks with minor siliceous rocks and clay-rich siltstones	Muddy and sandy diamictite, sandstone
6	296.34 – 339.92	Argillaceous rocks and siliceous rocks with minor clay-rich siltstones	Argillaceous rocks and siliceous rocks with minor clay-rich siltstones	Muddy diamictite, fine-grain sandstone, siltstone and claystone
7	339.92 – 436.18	Siliceous rocks and argillaceous rocks with minor clay-rich siltstones	Siliceous rocks and argillaceous rocks with minor clay-rich siltstones	VB sandy diamictite and volcanic-bearing sandstone
8.1	436.18 – 502.69	Interbedded sequences of argillaceous rocks, siliceous rocks and clay-rich siltstones	Argillaceous rocks interbedded with clay-rich siltstones	VB mudstone, sandstone and muddy diamictite
8.2	502.69 – 544.47	Interbedded sequences of argillaceous rocks, siliceous rocks and clay-rich siltstones	Argillaceous rocks interbedded with clay-rich siltstones	VB muddy diamictite, mudstone and sandstone
8.3	544.47 – 579.33	Siliceous rocks interbedded with argillaceous rocks and clay-rich siltstones	Siliceous rocks interbedded with argillaceous rocks and clay-rich siltstones	VB sandstone, mudstone and sandy diamictite
8.4	579.33 – 607.35	Siliceous rocks and argillaceous rocks interbedded with clay-rich siltstones	Argillaceous rocks with minor presence of limestone	VB muddy diamictite, siltstone and sandstone
9	607.35 – 648.74	Mainly clay-rich siltstones with minor presence of siliceous rocks and argillaceous rocks	Mainly siliceous rocks and clay-rich siltstones	VB sandstone and siltstone
10	648.74 – 778.34	Interbedded sequences of argillaceous rocks, siliceous rocks and clay-rich siltstones	Mainly argillaceous rocks, limestones and minor presence of siliceous rocks	VB sandy diamictite, silty sandstone and mudstone
11	778.34 – 904.66	Mainly siliceous rocks and clay-rich siltstones with a minor presence of argillaceous rocks	Mainly siliceous rocks and clay-rich siltstones with a minor presence of argillaceous rocks	Sandy siltstone and sandstone
12	904.66 – 996.69	Interbedded sequences of siliceous rocks and clay-rich siltstones with minor argillaceous rocks	Prevalence of argillaceous rocks interbedded with clay-rich siltstones. Minor presence of siliceous rocks	Sandy diamictite, silty sandstone and mudstone
13	996.69 – 1040.28	Mainly argillaceous rocks interbedded with siliceous rocks and clay-rich siltstones	Mainly argillaceous rocks and with minor presence of clay-rich siltstones and sands	Siltstone, sandy mudstone and muddy sandstone
14	1040.28 - 1138.54	Prevalence of clay-rich siltstones and siliceous rocks	Prevalence of clay-rich siltstones and siliceous rocks	Sandy diamictite and sandstone

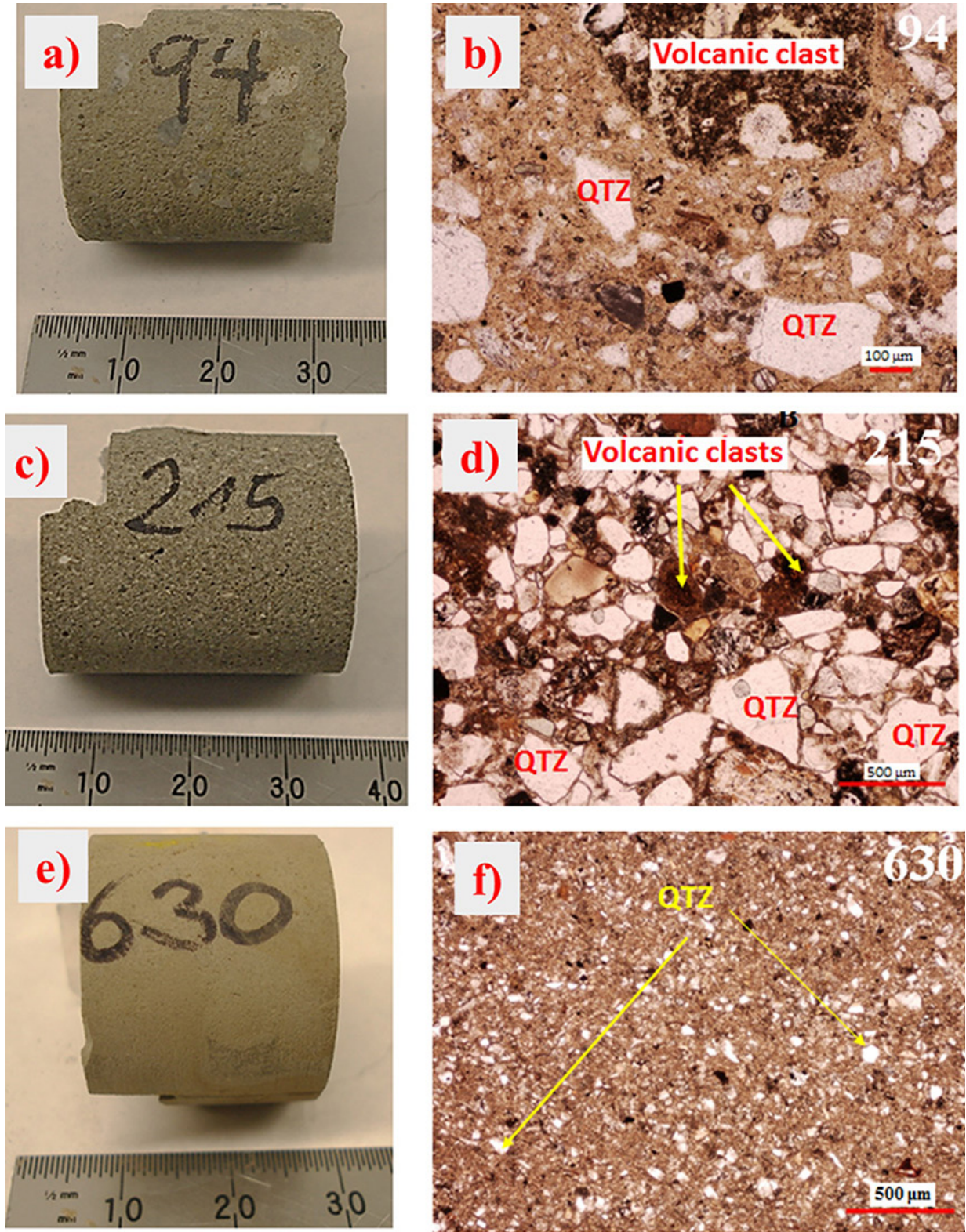


Figure 3. This figure shows the mineral lithotype sequences of the AND-2A drillcore identified from the interpretation of Figures 1 (b) and 2 along with the depth intervals related to the fourteen LSUs covering the AND-2A. The red markers indicate the position in depth of the six selected samples.

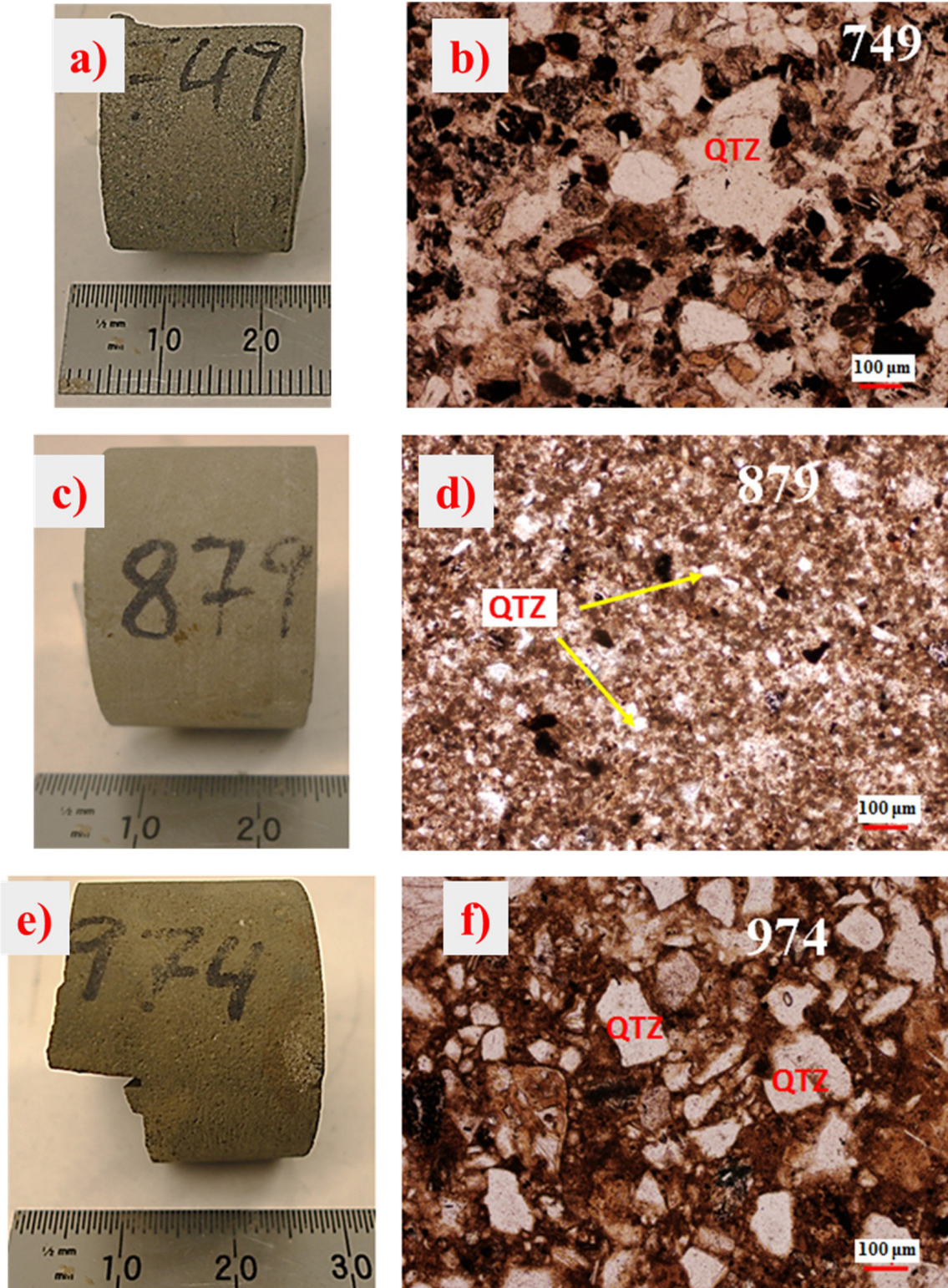


Figure 4. a) Photograph and b) thin section of sample 94: This sample is identified as a sandy diamictite. Quartz minerals (QTZ) and volcanic clasts are shown embedded in a silty matrix. c) Photograph and d) thin section of sample 215: This sample mainly contains coarse sandstone with a minor presence of finer volcanic clasts. e) Photograph and f) thin section of sample 630: identified lithology corresponds to siltstone.

analysis of these samples (see Table 4) show that their constituents minerals are quartz, clay minerals (illite and smectite), carbonates (siderite), calcium minerals (Phillipsite-Ca, Anorthite), feldspars (Orthoclase, Albite, Sanidine, Microcline) and mica (muscovite).

From Tables 2 and 3, we can note that the reported lithology from both Fielding *et al.* (2008) and the six selected samples are consistent with the mineral lithotypes obtained from the SC and Gardner methods. Thus, siliceous rocks and clay-rich siliceous rocks (sandy diamictite, sandstone, siltstone) are prevalent in LSU 2 (37.07 – 98.47 mbsf), LSU 3 (98.47 – 122.86 mbsf) and LSU 4 (122.86 – 224.82 mbsf). These mineral lithotypes are also consistent with the lithology of samples 94 (sandy diamictite with a silty matrix) and 215, (coarse sandstone). On the other hand, LSU 5 (224.82 – 296.34 mbsf) and LSU 6 (296.34 – 339.92 mbsf) represent a transition from siliceous rocks to both argillaceous rocks and clay-rich siltstones, while siliceous rocks (mainly sandstones) are characteristic of LSU 7 (339.92 - 436.18 mbsf). LSU 8.1 (436.18 – 502.69 mbsf) and LSU 8.2 (502.69 – 544.47 mbsf) are dominated by argillaceous rocks and siliceous rocks (Volcanic-Bearing VB mudstone, sandstone, and muddy diamictite). However, LSU 8.3 (544.47 – 579.33 mbsf) and LSU 8.4 (579.33 – 607.35 mbsf) are mainly comprised of siliceous rocks (sandstones, sandy diamictite). A finer lithology arises at LSU 9 (607.35 – 648.78 mbsf) consisting of clay-rich siltstone and sandstone with minor mudstones. The lithology of sample 630, a clay-rich siltstone, agrees with these findings. Then, an assemblage of argillaceous rocks, siliceous rocks, and clay-rich siltstones were found in LSU 10 (648.74 – 778.34 mbsf). Indeed, sample 749, Figures 5(a) and 5(b), a silty sandstone, is identified as a combination of clay-rich siltstone and a siliceous rock in Table 3. The LSU 11 (778.34 – 904.66 mbsf) mainly comprises siliceous rocks and clay-rich siltstones (sandy siltstone and sandstone). This lithology also agrees with the lithology of sample 879, a fine grain sandstone. LSU 12 (904.66 - 996.69 mbsf) contains interbedded sequences of clay-rich siltstones with minor mudstones. In particular, the lithology of sample 974, a silty sandstone, is related to the siliceous lithotype as portrayed in Figure 3. LSU 13 (996.69 – 1040.28 mbsf) shows a finer grain lithology than the previous LSU 12. In LSU 13, argillaceous rocks interbedded with clay-rich siltstones are prevalent. On the contrary, coarser grain lithologies such as siliceous rocks and clay-rich siltstones are present in LSU 14 (1040.28 – 1138.54 mbsf).

CONCLUSIONS

We have implemented a micromechanical SC modelling to generate density-velocity rock physics templates for the determination of mineral lithotypes on the AND-2A drillcore. Results show that calcite is an uncommon component of the lithology in the AND-2A as also reported by Staudigel *et al.* (2018). Instead, the identified mineral lithotypes correspond to the argillaceous lithotype, the clay-rich siliceous lithotype and the siliceous lithotype.

On the other hand, the mineral lithotype distribution identified by the ternary mineral RPT's along the AND-2A drillcore is consistent with the interpretation that we obtained from the implementation of Gardner's relationship. These results are also consistent with the main lithological features reported by Fielding *et al.* (2008). Furthermore, the lithology of the six selected samples can be directly correlated with the modelled mineral lithotypes. However, since these results attempt to assist in the characterization of glacial sediments, a more robust interpretation should include petrophysical and stratigraphic studies based on resistivity, neutron porosity, and gamma-ray borehole measurements which are commonly used to discriminate lithology. However, resistivity, neutron

Table 3. Lithology from visual description, SC and Gardner methods of six selected samples cut at different depths along the AND-2A.

Sample	Depth interval (mbsf)	Description	Lithology	
			Self-Consistent	Gardner
94	94.16-96.41	Sandy diamictite with a silty matrix	Siliceous rocks, clay-rich siltstone	Siliceous rocks
215	215.48-215.57	Coarse sandstone	Siliceous rocks	Siliceous rocks
630	628.81-630.89	Sandy mudstone (siltstone)	Clay-rich siltstone	Clay-rich siltstone
749	747.45-749.9	Silty Sandstone	Siliceous rocks, clay-rich siltstone	Siliceous rocks, clay-rich siltstone
879	879.41-879.58	Fine-grain sandstone	Siliceous rocks	Siliceous rocks
974	974.1-975.42	Silty sandstone	Siliceous rocks	Clay-rich siltstone

Table 4. Mineral identification from XR.

Sample (mbsf)	Mineral										
	Quartz	Illite	Smectite	Siderite	Phillipsite-Ca	Anorthite	Orthoclase	Albite	Sanidine	Microline	Muscovite
94	■	■		■	■	■		■			
215	■	■		■	■	■	■	■			
630	■	■		■	■	■		■			■
749	■	■	■	■	■	■	■	■			
879	■	■		■	■	■		■	■		
974	■	■		■	■	■		■	■	■	■

porosity, and gamma-ray data sets are less commonly available than density and velocity data sets. In this sense, the main advantage of RPT's generated from SC modelling is that this approach can be used to identify mineral lithotypes in glacial formations merely from the rock's elastic properties. In addition, any other combination of three minerals can be used. This is particularly useful since the physical properties of a variety of minerals are readily available in scientific literature.

Nevertheless, these results, as presented here, have the potential to add valuable information to the record of Antarctic glacial and geological history obtained from the AND-2A since variations in lithology can be used to describe paleoenvironmental and paleoclimatic changes as well as to identify source rocks (Iacoviello *et al.*, 2012).

ACKNOWLEDGEMENTS

The authors thank IMP (Instituto Mexicano del Petroleo) for supporting this research. Projects: H.62001 'Módulos del IWP' para presión de poro en terciario, carbonatos y simulador 3D'. This investigation was also funded by Fondo Sectorial Conacyt-Sener-Hidrocarburos, México, Project: 280097, IMP-UAlberta-PEMEX, Y.61067 'Modelos de física de rocas considerando estructura y anisotropía'. Core log data set and selected samples were obtained thanks to Doug Schmitt and Thomas Wonik as part of the AND-2A Drillcore, Southern McMurdo Sound Project, Antarctica.

REFERENCES

- Acton G., J. Crampton, G. Di Vincenzo, C. R. Fielding, F. Florindo, M. Hannah, D. M. Harwood, S. Ishman, K. Johnson, L. Jovane, R. Levy, B. Lum, M. C. Marcano, S. Mukasa, C. Ohneiser, M. Olney, C. Riesselman, L. Sagnotti, C. Stefano, E. Strada, M. Taviani, E. Tuzzi, K. L. Verosub, G. S. Wilson, M. Zattin and ANDRILL-SMS Science Team. 2008. Preliminary integrated chronostratigraphy of the AND-2A core, ANDRILL Southern McMurdo Sound project, Antarctica. *Terra Antartica*, 15, 211-220.
- Brink J. and R. D. Jarrard. 1998. Petrophysics of core plugs from CRP-1 drillhole, Victoria Land Basin, Antarctica. *Terra Antartica*, 5 (3), 291-297
- Close D., M. Perez, B. Goodway and G. Purdue. 2012. Integrated workflows for shale gas and case study results for the Horn River Basin, British Columbia, Canada. *The Leading Edge*, 31, 556-569.
- Dunbar G. B., C. Atkins, D. Magens and F. Niessen. 2009. Physical properties of the AND-2A core, ANDRILL Southern McMurdo Sound Project, Antarctica. *Terra Antartica*, 15, 49-56.
- Fielding C. R., C. B. Atkins, K. N. Bassett, G. H. Browne, G. B. Dunbar, B. D. Field, T. D. Frank, L. A. Kressek, K. S. Panter, S. Passchier, S. F. Pekar, S. Sandroni, F. Talarico and The ANDRILL-SMS Science Team. 2008. Sedimentology and stratigraphy of the AND-2A core, ANDRILL Southern McMurdo Sound Project, Antarctica. *Terra Antartica*, 15, 77-112.
- Florindo F., D. Harwood, F. Talarico, R. Levy and The ANDRILL-SMS Science Team. 2008-2009. Background to the ANDRILL Southern McMurdo sound project, Antarctica. *Terra Antartica*, 15, 13-20.
- Gamero-Diaz H., C. K. Miller and R. Lewis. 2013. sCore: A Mineralogy Based Classification Scheme for Organic Mudstones. SPE Annual Technical Conference and Exhibition. Society of Petroleum Engineers New Orleans, Louisiana, USA.
- Gardner G. H. F., L. W. Gardner and A. R. Gregory. 1974. Formation velocity and density—the diagnostic basics for stratigraphic traps. *Geophysics*, 39, 770-780.
- Hunze S., H. Schröder, G. Kuhn and T. Wonik. 2013. Lithostratigraphy determined from downhole logs in the AND-2A borehole, southern Victoria Land Basin, McMurdo Sound, Antarctica. *Geosphere*, 9, 63-73.

- Iacoviello F., G. Giorgetti, F. Nieto and I. T. Memmi. 2012. Evolution with depth from detrital to authigenic smectites in sediments from AND-2A drill core (McMurdo Sound, Antarctica). *Clay Minerals*, 47, 481-498.
- Iacoviello F., G. Giorgetti, I. Turbanti Memmi and S. Passchier. 2015. Early Miocene Antarctic glacial history: new insights from heavy mineral analysis from ANDRILL AND-2A drill core sediments. *International Journal of Earth Sciences*, 104, 853-872.
- Keller G. V. 1988. A practical introduction to borehole geophysics. *EOS Transactions*, 69, 850-851.
- Lizcano-Hernández E. G., R. Nicolás-López, O. C. Valdiviezo-Mijangos and J. Meléndez-Martínez. 2018. Estimation of brittleness indices for pay zone determination in a shale-gas reservoir by using elastic properties obtained from micro-mechanics. *J. Geophys. Eng.*, 15, 307-314.
- López-Lena-Estrada A., J. Meléndez-Martínez, O. C. Valdiviezo-Mijangos and R. Nicolás-López. 2021. Design and development of a robust computing workflow to build rock physics templates from a micromechanical self-consistent model. *J Appl Geophys*, 184, 104248.
- Mavko G., T. Mukerji and J. Dvorkin. 2009. *The Rock Physics Handbook: Tools For Seismic Analysis Of Porous Media*. New York: Cambridge University Press.
- Nicolás-López R., J. Meléndez-Martínez, A. López-Lena-Estrada, O. C. Valdiviezo-Mijangos, C. Couder-Castañeda, E. Coconi-Morales and J. A. España-Pinto. 2020. Micromechanics modelling for mineral volume fraction determination: application on a terrigenous formation. *Scientific Reports*, 10, 16629.
- Nicolás-López R. and O. C. Valdiviezo-Mijangos. 2016. Rock physics templates for integrated analysis of shales considering their mineralogy, organic matter and pore fluids. *J. Petrol. Sci. Eng.*, 137, 33-41.
- Nicolás-López R., O. C. Valdiviezo-Mijangos, J. Meléndez-Martínez and V. M. Levin. 2019. A multimineral Rock Physics Template built from the Perfectly Disordered Method for shale lithology interpretation. *J. Petrol. Sci. Eng.*, 176, 532-536.
- Niessen F. and R. D. Jarrard. 1998. Velocity and porosity of sediments from CRP-1 drillhole, Ross Sea, Antarctica *Terra Antartica*, 5 (3), 311-318
- Niessen F., R. D. Jarrard and C. Búcker. 1998. Log-based physical properties of the CRP-1 Core, Ross Sea, Antarctica. *Terra Antartica*, 5 (3), 299-310
- Sabina F. J. and J. R. Willis. 1988. A simple self-consistent analysis of wave propagation in particulate composites. *Wave Motion*, 10, 127-142.
- Staudigel P. T., S. Murray, D. P. Dunham, T. D. Frank, C. R. Fielding and P. K. Swart. 2018. Cryogenic brines as diagenetic fluids: Reconstructing the diagenetic history of the Victoria Land Basin using clumped isotopes. *Geochimica et Cosmochimica Acta*, 224, 154-170.
- Stephenson D. A., A. H. Fleming and D. M. Mickelson. 1988. Glacial deposits. In: W. Back, J. S. Rosenshein and P. R. Seabers (eds.). *Hydrogeology: The Geology of North America*. Geological Society of America pp. 301-314.
- Valdiviezo-Mijangos O. C., J. Meléndez-Martínez and R. Nicolás-López. 2020. Self-consistent and squirt flow modelling of velocity dispersion and attenuation for effective-stress dependent experimental data. *Explor. Geophys.*, 51, 248-255.
- Valdiviezo-Mijangos O. C. and R. Nicolás-Lopez. 2014. Dynamic characterization of shale systems by dispersion and attenuation of P-and S-waves considering their mineral composition and rock maturity. *J. Petrol. Sci. Eng.*, 122, 420-427.
- Wilson G. S., T. R. Naish, R. D. Powell, R. H. Levy and J. S. Crampton. 2012. Late Neogene chronostratigraphy and depositional environments on the Antarctic Margin: New results from the ANDRILL McMurdo Ice Shelf Project. *Global and Planetary Change*, 96-97, 1-8.
- Wonik T., T. Grelle, D. Handwerker, R. D. Jarrard, A. McKee, T. Patterson, T. Paulsen, S. Pierdominici, D. R. Schmitt, H. Schroeder, M. Speece and T. Wilson. 2008-2009. Downhole Measurements in the AND-2A Borehole, ANDRILL Southern McMurdo Sound Project, Antarctica. *Terra Antartica*, 15(1), 57-68.

<https://doi.org/10.22201/igeof.00167169p.2022.61.1.2188>

COMPLEJACIÓN DE METALES POR SUSTANCIAS HÚMICAS ACUÁTICAS COMO PROCESO NATURAL, TOMANDO COMO CASO DE ESTUDIO EL LAGO DE XOCHIMILCO, CIUDAD DE MÉXICO, MÉXICO.

María de Jesús González-Guadarrama¹, Silvia Elena Castillo-Blum¹ y María Aurora Armienta-Hernández².

Recibido: 26 de julio de 2021; aceptado: 29 de noviembre de 2021; publicado en línea: 1 de enero, 2022.

RESUMEN

En este trabajo se presenta la importancia de la materia orgánica, específicamente Substancias Húmicas Acuáticas (SHA) dentro de la especiación y distribución de metales y nutrientes dentro de un sistema acuático, en este caso el Lago de Xochimilco, sitio con gran importancia ecológica, el cual, es hábitat natural de la especie endémica axolotl (ajolote). En esta investigación se realizaron reacciones de complejación entre las SHA y metales (Cu, Mn, Pb y Zn) bajo diferentes condiciones de pH, la fuente de las SHA corresponde con la muestra de agua tomada en el Lago de Xochimilco, en presencia o ausencia de disolución amortiguadora de pH, además de variar la concentración de los metales. Los resultados muestran que existe una competencia directa entre los elementos mayores y oligoelementos por reaccionar con las SHA; además, que bajo las condiciones de pH del Lago de Xochimilco es muy posible que se formen los compuestos complejos.

Palabras clave: Remediación, sustancias húmicas acuáticas, metales, reacciones de complejación y Lago de Xochimilco.

ABSTRACT

This work discusses the importance of organic matter, specifically Aquatic Humic Substances (SHA) within the speciation and distribution of metals within an aquatic system, in this case Xochimilco Lake, a site with great ecological importance. This lake is the natural habitat of the endemic species “axolotl” (ajolote). In this research, complexation reactions between SHA and metals (Cu, Mn, Pb and Zn) were carried out under different reaction conditions, the source of AHS was water samples taken in Xochimilco Lake in presence and absence of pH buffer dissolution and varying the concentration of metals. The results show that there is a direct competition between the major elements and trace elements to react with the AHS. Under the pH conditions of Xochimilco Lake complexes formation is possible.

KEY WORDS: Remediation, aquatic humic substances, metals, reactions of complexation and Xochimilco Lake.

*Corresponding author at chuy41284@yahoo.com.mx¹

¹Facultad de Química, Universidad Nacional Autónoma de México, Av. Universidad 3000, Col UNAM, Coyoacán, Ciudad de México, CP 04510. Castillo-Blum Silvia Elena, email: blumearly@gmail.com.

²Departamento de Recursos Naturales, Instituto de Geofísica, Universidad Nacional Autónoma de México. Av. Universidad 3000, Col. UNAM, Coyoacán, Ciudad de México, CP 04510. Armienta-Hernández María Aurora, email: victoria@unam.mx.

INTRODUCCIÓN

La distribución de micro y macronutrientes en sistemas acuáticos se ve afectada por diversos procesos fisicoquímicos relacionados con la influencia de actividades naturales o antropogénicas, siendo las reacciones de complejación de las más importantes. Dichas reacciones pueden ocurrir entre la materia orgánica y metales (incluyen tejidos de organismos) presentes en la columna de agua (Rocha *et al.*, 2000, Chen *et al.*, 2007, Liu *et al.*, 2010).

Las sustancias húmicas acuáticas (SHA) son consideradas como el principal reservorio de carbono en medios acuáticos. Éstas son macromoléculas producto de la degradación de biomoléculas y posterior polimerización; de acuerdo con su caracterización la concentración de heteroátomos se ve disminuida a medida que aumenta el peso molecular y el grado de polimerización. Las SHA han sido clasificadas por su grado de polimerización como: ácidos fúlvicos, ácidos húmicos y huminas. El último grupo por sus características de polimerización, alto peso molecular y baja o nula solubilidad no son encontradas en la columna de agua (Camargo y Cruz, 1999, Motuzova *et al.*, 2012).

Las SHA poseen grupos funcionales como fenoles, aminas, ácidos carboxílicos entre otros, que involucran la presencia de heteroátomos como O, N y S (Camargo y Cruz, 1999, Motuzova *et al.*, 2012). Estos grupos pueden reaccionar y formar complejos con metales y metaloides, especialmente por átomos de oxígeno. Las SHA pueden formar complejos polinucleares y reaccionar simultáneamente con diferentes elementos, en función de las condiciones ambientales que prevalezcan en el cuerpo de agua. La formación de estos compuestos es muy importante para la movilidad de los elementos (Munier *et al.*, 1986, Chen *et al.*, 2007, Lippold y Lippmann-Pipke, 2009).

La movilidad de los metales en los sistemas acuáticos es relevante debido a que juegan un rol importante dentro de los procesos metabólicos. Una concentración deficiente de los metales considerados esenciales implica que las condiciones ambientales no sean favorables para el desarrollo de los organismos, pero por otro lado si las concentraciones son excesivas pueden ser tóxicos e inhibir los procesos biológicos. Por esto es muy importante la cuantificación e identificación de la presencia y especie química en la que se encuentran (Elkins y Nelson, 2001, Cabaniss, 2009).

La identificación correcta de la especie química del metal es esencial para determinar su disponibilidad, toxicidad y movilidad. La especiación depende de las condiciones fisicoquímicas del cuerpo de agua, que están relacionadas con la variación de la geología de la cuenca, tipo de cuenca, profundidad, oleaje, aportes antropogénicos o naturales, organismos que habitan ahí además del proceso fotosíntesis-respiración.

Los valores de pH de los sistemas acuáticos se encuentran en un intervalo muy amplio variando desde muy ácido (2) hasta valores superiores a 8. Las variaciones de este parámetro pueden ser temporales, por ejemplo: en un mismo día dependiendo si prevalece el proceso de respiración o fotosíntesis, de la misma forma pueden ser variaciones estacionales (estiaje o lluvias), también existe la posibilidad en sistemas profundos que se genere estratificación, evento que produce que las condiciones fisicoquímicas no sean iguales en toda la columna de agua (Margalef, 1983, Laglera y Van Den Berg, 2009, Su *et al.*, 2012).

El estudio de las posibles reacciones entre las sustancias presentes en ambientes acuáticos bajo diferentes condiciones fisicoquímicas para identificar los patrones de comportamiento es relevante

debido a que el conocimiento de esta información puede generar modelos que permitan la predicción de los posibles procesos que ocurren en el sitio a partir de un monitoreo de rutina.

La capacidad de los metales alcalinos, alcalinotérreos y de la primera serie de transición de formar compuestos con materia orgánica se ha determinado en diversos estudios, e indican que los elementos alcalinos y alcalinotérreos son menos reactivos que los de transición, estos últimos incrementan la reactividad con el número atómico (Shuman y Cromer, 1979, Davidge *et al.*, 2001, Elkins y Nelson, 2001).

Se han efectuado experimentos de complejación bajo diferentes condiciones de pH (3-6) empleando disoluciones amortiguadoras, como acetatos y boratos. Los resultados muestran ligeras modificaciones en la reacción de los elementos de transición, pero no así en los elementos alcalinos y alcalinotérreos (Shuman y Cromer, 1979, Ryan y Weber, 1982, John *et al.*, 1988, Davidge *et al.*, 2001, Elkins y Nelson, 2001). Para la extrapolación de los resultados en ambientes naturales es muy importante estudiar las reacciones bajo condiciones similares a las ambientales.

El objetivo de este trabajo es analizar las reacciones de complejación de SHA de Xochimilco con los metales Cu, Mn, Pb y Zn en condiciones de pH similares a las del sitio, así como el análisis de lo que puede ocurrir en ausencia de una disolución amortiguadora de pH.

SITIO DE MUESTREO

Las muestras de agua fueron colectadas en el Lago de Xochimilco, las cuales contienen SHA. Este cuerpo de agua se localiza en el sur de la Ciudad de México en las coordenadas 19.552' N, 99.05265 O. En la época prehispánica tenía un rol importante en agricultura y transportación. Desgraciadamente sus dimensiones se han visto disminuidas a canales debido al crecimiento poblacional y al uso excesivo del recurso agua. Sin embargo, el sitio se emplea en el desarrollo de agricultura tradicional "chinampas" y también como atracción turística. Además, cuenta con la presencia de especies endémicas como el "axolotl", por lo que se puede considerar que el Lago de Xochimilco tiene una gran importancia ecológica y preservarlo es de suma importancia.

El *axolotl* (del náhuatl cabeza de perro) es un anfibio, especie endémica de los lagos prehispánicos de la zona central de México, que posee la capacidad de regenerar los tejidos de manera natural, lo que lo ha llevado a ser empleado con propósitos médicos, fue declarado especie en peligro de extinción por La Comisión Nacional para el Conocimiento y Uso de la Biodiversidad (CONABIO) de acuerdo con la norma oficial mexicana 059-ECOL-2010. Además, estudios han mostrado el efecto de diferentes contaminantes como plaguicidas, fertilizantes, detergentes y metales pesados sobre el axolotl, de ahí que encontrar una técnica adecuada para el restablecimiento del equilibrio de dicho ecosistema se vuelva trascendental (Robles-Mendoza *et al.*, 2009, Robles-Mendoza *et al.*, 2011, Chaparro-Herrera *et al.*, 2013, Zapata-Gutiérrez y Solís-Juárez, 2013).

En el Lago de Xochimilco existen diferentes áreas de acuerdo con el tipo de actividades que se realizan, lo que se ve reflejado en la variación de condiciones fisicoquímicas. De acuerdo con López-López *et al.* (2006) zonas de alta producción primaria (alta concentración de clorofilas) se encuentran en las zonas urbana y turística (139.4 y 150 mg L⁻¹ de clorofila respectivamente) pero hay un decremento en la zona agrícola (48.9 mg L⁻¹).

METODOLOGÍA

Se colectaron muestras de agua en el canal Caltongo dentro del Lago de Xochimilco, se determinaron los parámetros fisicoquímicos, posteriormente el agua se filtró a través de malla 40 y enseguida por la de 0.45 μm , una porción de la muestra fue acidificada con ácido nítrico concentrado a un pH de 2, para poder realizar la cuantificación de cationes mayores. Las concentraciones de Ca y Mg se determinaron por valoración complejométrica con EDTA. Los contenidos de Na y K se obtuvieron por Espectroscopia de Absorción Atómica y Emisión con el equipo Perkin Elmer 2380 en las longitudes de onda de 589 nm y 768 nm respectivamente, con curvas de calibración que se encuentran en el intervalo entre 5-30 mg L^{-1} .

Se determinó la concentración de aniones por valoraciones ácido-base con HCl (0.02 N) para CO_3^{2-} y HCO_3^- , y de electrodo de ión selectivo para Cl^- y F^- con el potenciómetro Thermo Scientific Orion 5 Star con disoluciones de referencia en el intervalo 1-10 mgL^{-1} . Las concentraciones de SO_4^{2-} se analizaron por turbidimetría, con la reacción generada con BaCl_2 , con las mediciones en una longitud de onda de 420 nm y considerando la curva de calibración entre 0 y 20 mgL^{-1} .

La concentración de SHA se determinó por el método espectrofotométrico uv/vis, con el equipo Hewlett Packard 8909A0 acoplado a un sistema Peltier, en una $\lambda=240$ nm y a partir de la curva de calibración con valores de concentración entre 0 y 80 mgL^{-1} , elaborada con SHA de Xochimilco aisladas previamente bajo la técnica de Thurman y Malcom (1981).

Una vez caracterizada el agua se procedió a realizar 3 diferentes experimentos que se desarrollaron por triplicado. En general las series de reacciones se llevaron a cabo colocando 30 mL de agua de Xochimilco previamente filtradas, 5 mL de disolución amortiguadora de pH (6.5) de acuerdo con el valor determinado originalmente en las muestras y 1 ó 3 mL de disolución del metal, dependiendo de la serie (a partir de una concentración de 500 mgL^{-1} para cada metal) o dependiendo de la serie de reacciones que se haya desarrollado. Se establecieron dos secuencias de reacciones modificando la concentración de metales adicionada (13 mgL^{-1}), una vez establecida la mejor concentración se desarrolló otra fase de la experimentación en la que se monitoreó la variación de pH producto de la reacción entre las SHA y los diferentes metales.

La cuantificación de cada uno de los metales fue determinada por medio de Espectroscopía de Absorción Atómica, con el equipo Perkin Elmer AAnalyst 200 bajo las condiciones analíticas a continuación descritas en la tabla 1.

Las reacciones procedieron en condiciones ambientales de la Ciudad de México, temperatura promedio de 20°C con una agitación de 1 h, para posteriormente ultrafiltrar, el precipitado corresponde al

Tabla 1. Las condiciones analíticas de operación del equipo para determinar las concentraciones de Cu, Mn, Pb y Zn que no fueron complejados y se encuentran en las aguas madres de la reacción.

Elemento	LD (mgL^{-1})	Concentraciones de la curva de calibración (mgL^{-1})	R ²
Cu	0.25	0.5, 1.5, 3 y 4	0.9999
Mn	0.10	0.2, 0.6, 1.2 y 2.5	0.9989
Pb	0.5	1, 3 y 6	0.9998
Zn	0.05	0.1, 0.3, 0.6 y 1	0.9998

complejo formado y en la fase líquida permanece el metal que no reaccionó, por lo que cuantificarlo nos permite determinar la capacidad de complejación, la cual se determina mediante la siguiente ecuación:

$$CC = \frac{[M]}{[L]}$$

En donde

CC= Capacidad de complejación.

[M]= cantidad del metal que reaccionó, expresada en mmol.

[L]= cantidad del ligante, expresada en g.

Los productos aislados se caracterizaron por medio de Espectroscopia de Infrarrojo, desarrollado en la USAII (Unidad de Servicios de Apoyo a la Investigación y a la Industria), mediante la técnica de Reflectancia Total Atenuada (ATR por sus siglas en inglés) con el equipo Perkin Elmer FT-IR SPECTRUM 400 y observados por la técnica de Microscopia Electrónica de Barrido (MEB) con el equipo TM3030 Plus Hitachi Tabletop Microscope A en los laboratorios de Petrografía y Microscopía y de Sedimentología Volcánica del Instituto de Geofísica de la UNAM.

RESULTADOS

La caracterización del agua de Xochimilco nos muestra que es bicarbonatada sódica, con un pH de 6.8 e indica que se cuenta con la presencia de los cationes mayores Mg^{2+} , Ca^{2+} y Na^+ , iones que pueden competir con los oligoelementos en ocupar los sitios de complejación en las SHA. En cuanto a los aniones como ya se indicó el principal es el HCO_3^- , seguido de Cl^- y SO_4^{2-} , como se aprecia en la figura 1.

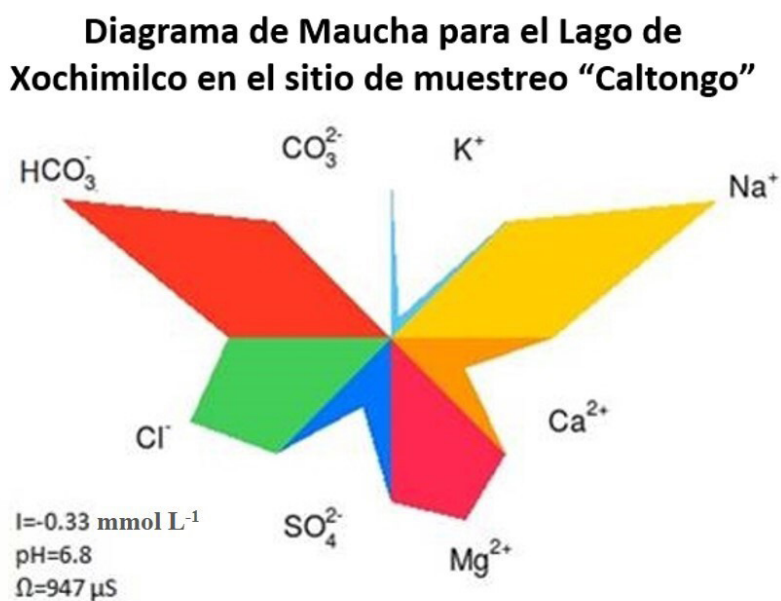


Figura 1. Diagrama de Maucha (Public license GPL-3, GNU) correspondiente al agua del Lago de Xochimilco.

Se determinó la concentración de las SHA y fue de 120 mg L^{-1} , después se realizaron las diferentes reacciones, para lo cual como se indicó en la metodología se emplearon 2 concentraciones para los metales (13 y 32 mgL^{-1}) y se observan pequeñas variaciones en la capacidad de complejación, lo que explica que si aumenta la concentración puede haber más sitios sustituidos por los metales oligoelementos, claro llegando a un equilibrio y es muy importante destacar que ésta también variará en función del pH.

Para identificar las diferentes condiciones de reacción se acotará de la siguiente manera XT que significa la reacción de la muestra de Xochimilco con todos los metales, acompañado de S/A significa sin disolución amortiguadora, XT3 corresponde a la reacción con disolución amortiguadora de pH, con concentración para los metales de 32 mgL^{-1} y XT1C/A es cuando la reacción procedió con disolución amortiguadora de pH y la concentración para cada metal fue de 13 mgL^{-1} .

La principal diferencia de complejación se encuentra en el caso XT, (Figura 2) en el cual se monitoreó el cambio del pH ya que no hay una disolución reguladora de pH o algún proceso que pueda amortiguar el pH como es el de respiración- fotosíntesis. El pH inicial fue de 6.8, al incorporar los metales fue de 5.8 y al finalizar la reacción fue de 6.3, muestra clara de una reacción ácido-base. En esta secuencia, el elemento que presenta una disminución en cuanto a la reactividad se refiere es el Mn, muy probablemente por la competición con los elementos mayores y porque los bicarbonatos ayudan a estabilizar el compuesto que forman.

Como ha sido descrito por Xue *et al.* (1995), Davidge *et al.* (2001), Bryan *et al.* (2002), Goveia *et al.* (2010) y otros el Cu tiene una gran afinidad hacia la materia orgánica, especialmente con las SHA. Indican que la reacción es muy afectada por el pH y la reacción más cuantitativa procedió en un $\text{pH}=6$, decreciendo en valores superiores de pH, muy probablemente por la formación de los hidróxidos del metal.

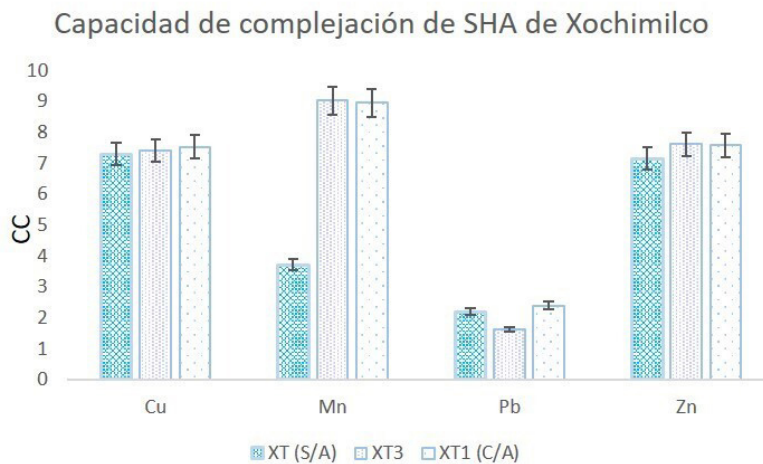


Figura 2. Gráfico que muestra la capacidad de complejación de las SHA de Xochimilco, hacia cada uno de elementos objeto de estudio bajo las diferentes condiciones de reacción, descritas previamente.

DISCUSIÓN

Al considerar los cationes mayores en la competencia para reaccionar con las SHA, se percibió que de acuerdo con experimentos previos desarrollados por González-Guadarrama *et al.* (2018) la ca-

pacidad de complejación hacia los oligoelementos se ve disminuida en su valor; sin embargo, no la anula, y sigue teniendo un gran potencial para reaccionar y modificar la especiación de los metales potencialmente tóxicos.

Al tener una mezcla de metales con posibilidad de reaccionar con las SHA es importante identificar si se puede formar el compuesto polinuclear y poliatómico, ya que sería muy interesante saber la repercusión de la formación de estos compuestos en la distribución de nutrientes dentro de los sistemas acuáticos. Un factor muy importante por considerar es el cambio de solubilidad de las especies metálicas y las SHA al reaccionar, lo cual podemos observar en la figura 3, en donde se aprecia que antes de la reacción todo se encuentra en disolución y una vez finalizada la reacción y agitación el producto formado precipita, clara evidencia de su baja solubilidad.

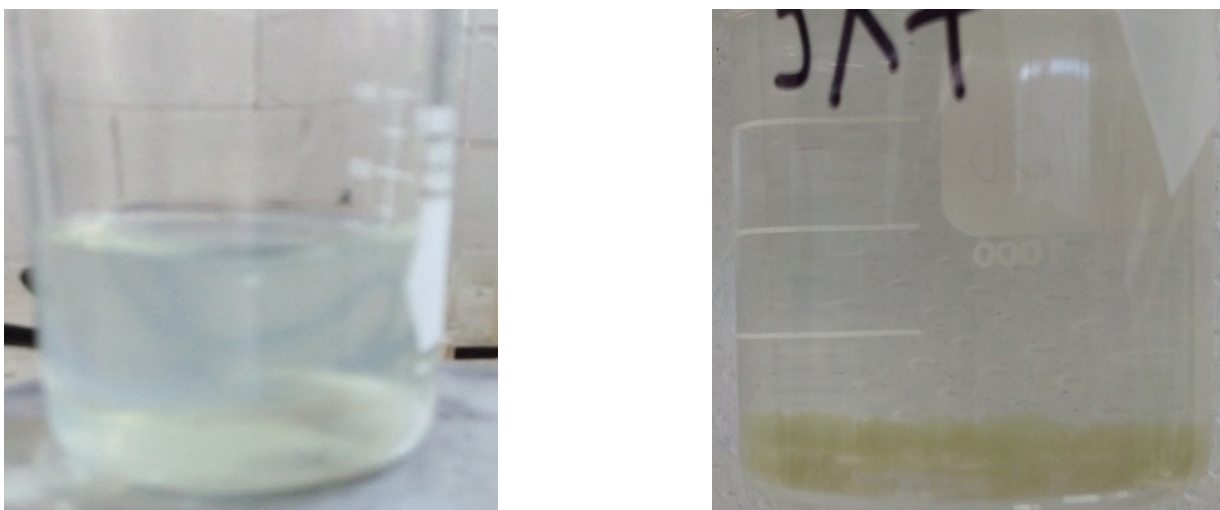


Figure 3. A la izquierda se puede observar la imagen del periodo de reacción entre las SHA y los metales y a la derecha se observa como precipitan los productos de la reacción y la disolución queda traslúcida.

La evidencia de la precipitación de los compuestos formados es muy importante, porque se evidencia un cambio en la biodisponibilidad de los metales, ya que al formar el complejo se espera que disminuya, incluso de las SHA, que van a presentar un cambio en la ubicación dentro del sistema acuático, es decir, se encontrarán en la columna de agua, en los sedimentos o en la superficie, de ahí que es preciso considerar si se trata un sistema lótico o léntico, polimíctico o monomíctico, además de características como la profundidad, si es época de estiaje o lluvias, características que también condicionan las reacciones al determinar los posibles valores de pH y Eh (Margalef, 1983).

El caso específico de Xochimilco es muy interesante, porque en gran parte de su área se ha visto reducido a canales, lo que disminuye la movilidad y la mezcla, lo que se puede reflejar de dos formas, la primera que la reacción de complejación no se lleve a cabo debido a la poca interacción entre los reactivos, la segunda es que si proceda la reacción y que por la baja solubilidad los compuestos sean precipitados hacia los sedimentos.

En el segundo panorama es preciso verificar las condiciones de pH, ya que puede ser una región anóxica lo que genera una disminución considerable en el pH, y puede provocar que el compuesto sea disociado y reincorporar los metales a la columna de agua, al igual que las SHA (John *et al.*, 1988, Lagier *et al.* 2000).

En trabajos previos dentro del grupo de trabajo se determinó la capacidad de complejación de cada uno de los elementos propuestos en este trabajo con las SHA de Xochimilco (González-Guadarrama *et al.* 2018) y permite realizar una comparación con los encontrados en este trabajo al tener la mezcla de todos ellos reaccionando al mismo tiempo, recordando que la capacidad de complejación muestra la relación de la cantidad de metal expresada en mmol, con respecto de la cantidad de ligante expresada en gramos. Dicho comparativo se puede ver en la tabla 2.

Tabla 2. Capacidad de complejación de las SHA de Xochimilco hacia Cu, Mn, Pb y Zn en soluciones individuales y en presencia simultánea de todos ellos en los experimentos realizados en esta investigación.

Elemento/ C. C.	Reacción individual	Reacción multielemental	
1 mL/3 mL			
Cobre	9.00±0.03	6.24±0.01	5.66±0.04
Manganeso	8.30±0.20	7.60±0.03	6.73±0.03
Plomo	2.3±0.01	1.37±0.01	1.78±0.008
Zinc	11.00±0.01	6.41±0.003	5.71±0.008

C.C. Capacidad de complejación ($\text{mmol}\cdot\text{g}^{-1}$)

Se aprecia que los valores de complejación se ven disminuidos como es lógico al tener todos los elementos presentes; sin embargo, los valores para el caso del Mn no presentan una disminución considerable a diferencia de los otros elementos, al considerar que el Cu presenta una disminución de $34\pm 4\%$, el Mn de $14\pm 5\%$, el Pb de $32\pm 8\%$ y el Zn de $46\pm 4\%$. Lo que es muy importante ya que corrobora que la capacidad de complejación total de las SHA, no es muy cambiante, y que existe la competencia entre los metales para ocupar los sitios de reacción en las SHA.

Otro factor para considerar es que al incrementar la concentración de los metales en la reacción multielemental la capacidad de complejación se ve abatida, salvo para el Pb, elemento para el cual se observa un incremento del 29%. Los resultados pueden ser un indicador de que las SHA son el reactivo limitante y que la concentración de los metales puede ser un inhibidor de la reacción.

En las reacciones *in situ* no se puede despreciar la presencia de los cationes mayores, ya que guardan una gran afinidad para ocupar los sitios activos en las SHA, tal es el caso que una de las formas comunes para encontrarlas es en forma de sales con Na principalmente. Un aspecto por destacar es por lo tanto que va a existir una competencia en las reacciones de complejación con las SHA entre los elementos mayores y oligoelementos, generando así complejos con los diferentes metales simultáneamente.

A través del análisis del espectro de infrarrojo (IR) de los complejos aislados se aprecia que los enlaces se producen entre el metal y los grupos carboxilo de las SHA, para todos los metales, lo cual es muy lógico al considerar que dentro de las moléculas precursoras de las SHA se encuentran principalmente estos grupos funcionales. El espectro de IR se puede observar en la figura 4.

Además, el análisis realizado con el Microscopio electrónico de barrido, acoplado a EDS corrobora que se forman compuestos complejos, ya que la estructura de la muestra de las SHA de Xochimilco es uniforme y podría parecer limolita a través de la imagen microscópica; sin embargo, una vez que reaccionan se aprecia el cambio morfológico como se puede apreciar en la figura 5.

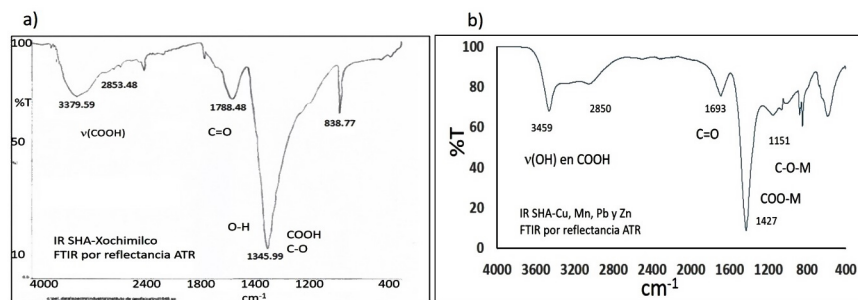


Figura 4. Espectros de IR realizados a las SHA de Xochimilco antes (a) y después de la reacción (b) para monitorear el cambio en las señales y a partir del cambio en la señal de los enlaces O-H se puede observar la interacción entre el oxígeno con enlace sencillo al carbono con los metales.

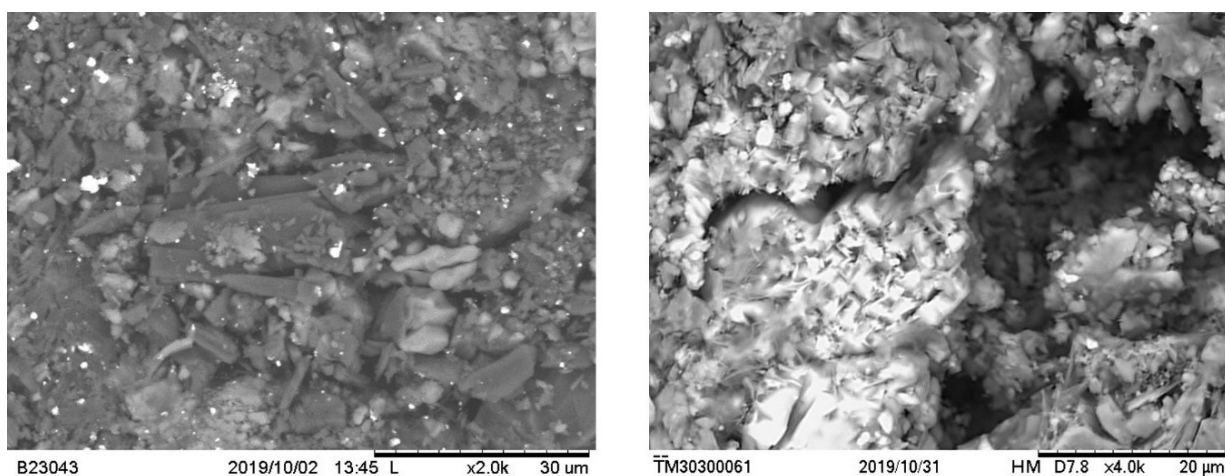


Figura 5. Imagen de las SHA antes y después de la reacción, en donde se aprecia la modificación física del ligante después de la reacción.

CONCLUSIONES

Las condiciones fisicoquímicas de los canales del Lago de Xochimilco favorecen la formación de los compuestos complejos entre las SHA y los metales Cu, Mn, Pb y Zn.

Los compuestos formados presentan poca solubilidad, por lo que, si no hay un flujo turbulento considerable en el lago de Xochimilco, los compuestos precipitarán.

La capacidad de complejación indica que las SHA presentan una gran afinidad hacia los metales de transición, aunque se debe de considerar la competencia con los elementos mayores Na, K, Mg y Ca.

AGRADECIMIENTOS

Se agradece la beca posdoctoral otorgada por parte de la Dirección General de Asuntos de Personal, UNAM, al apoyo técnico por parte de la Dra. Karla Patricia Salas Martin, a la Biol. Patricia Fierro, a la QFB Olivia Cruz Ronquillo, a la M. I. Alejandra Aguayo Ríos.

REFERENCIAS

- Bryan S. E., Tipping E., Hamilton-Taylor J. (2002) Comparison of measured and modeled copper binding by natural organic matter in freshwaters. *Comparative Biochemistry and Physiology*, 133;37-49.
- Cabaniss S. E. (2009) Forward modeling of metal complexation by NOM: I. A priori prediction of conditional constants and speciation. *Environ Sci. Technol.* 43; 2838-2844.
- Camargo V M., Cruz T L E., (1999) Sustancias húmicas en aguas para abastecimiento. *Revista Ingeniería e Investigación.* 44; 63-72.
- Chaparro-Herrera D. J., Sarma N., Sarma SSS (2013) Effect of water quality on the feeding ecology of axolotl *Ambystoma mexicanum*. *J Limnol*; 72;3: 555-563. DOI: 10.4081/jlimnol.2013.e46
- Chen C., Wang X., Jiang H., Hu W., (2007) Direct observation of macromolecular structures of humic acid by AFM and SEM. *Colloids and surface A: Physicochem. Eng. Aspects*, 302; 121-125.
- Davidge J., Thomas C. P. Williams D. R. (2001) Conditional formation constants or chemical speciation data? Chemical speciation and Bioavailability, 13, 4; 129-134.
- Elkins K. M., Nelson D J. (2001) Fluorescence and FT-IR spectroscopic studies of Suwanne river fulvic acid complexation with aluminum, terbium and calcium. *Journal of Inorganic Biochemistry*, 87; 81-96.
- González-Guadarrama M.J., Armenta-Hernández MA., Rosa A. H. (2018) Aquatic Humic Substances: Relationship Between Origin and Complexing Capacity. *Bull Environ Contam Toxicol*, 100: 627-633. Doi.org/10.1007/s00128-018-2318-4.
- Goveia D., Aparecida L. F., Burba P., Fernandes F., Dias F., Rosa A. H. (2010) Approach combining on-line metal exchange and tangential-flow ultrafiltration for in-situ characterization of metal species in humic hydrocolloids. *Anal. Bioanal Chem*, 397; 851-860.
- John J., Salbu B., Gjessing E. T., Bjornstad H. E. (1988) Effect of pH, humus concentration and molecular weight on conditional stability constants of cadmium. *Wat. Res.*, 22, 11; 1381-1388.
- Lagier T., Feuillade G., Matejka G. (2000) Interactions between copper and organic macromolecules: determination of conditional complexation constants. *Agronomie*, 20; 537-546.
- Laglera, L M., Van den Berg C. M. G. (2009) Evidence for geochemical control iron by humic substances in seawater. *Limnology and. Oceanography*, 54 (2) 610-619.
- Lippold H., Lippmann-Pipke J. (2009) Effect of humic matter on metal adsorption onto clay material: Testing the linear additive model. *J. of Contaminant Hidrology*, 109; 40-48.
- Liu J., Wang J., Chen Y., Lippold H., Lippman-Pipke J. (2010) Comparative characterization of two natural humic acids in the Pearl River Basin, China and their environmental implications. *J. of environmental Sciences*, 22, 11; 1695-1702.
- López-López E., Sedeño -Díaz J., Perozzi F. (2006) Lipid peroxidation and acetylcholinesterase activity as biomarkers in the black Sailfin Goodeid, *Girardinichthys viviparous* (Bustamonte) exposed to water from Lake Xochimilco (Mexico). *Aquatic Ecosystem Health & Management*, 9;3; 379-385.
- Margalef, R. (1983) *Limnología*. Ediciones Omega S. A., España, pp 39-76
- Motuzova G., Makarychev I., Dergham H., Stepanor A., Barsora N. (2012) *Soil Organic Matter and its interactions with metals processes, factors ecological significance*. NOVA Science Publishers Inc., New York USA. 136pp.
- Munier-Lamy C., Adrian P H., Berthelin J., Rouiller J. (1986) Comparison of binding abilities of fulvic and humic acids extracted from recent marine sediments with UO₂²⁺. *Org Geochem* 9, 6; 258-292.
- Robles-Mendoza C., García Basilio S., Cram-Heydrich S., Hernández- Quiroz M., Vanegas -Pérez C. (2009) Organophosphorus pesticides effect on early stages of the axolotl *Ambystoma mexicanum* (Amphibia Caudata) *Chemosphere*, 74; 5: 703-710

- Robles-Mendoza C., Zúñiga-Lagunes SR., Ponce de León-Hill CA., Hernández-Soto J., Vanegas-Pérez C. (2011) Esterases activity in the axolotl *Ambystoma mexicanum* exposed to chlorpyrifos and its implication to motor activity. *Aquatic Toxicology*, 105; 3-4: 728-734. Doi.org/10.1016/j.aquatox.2011.09.001
- Rocha, J. C., De Sene J. J., Dos Santos A., Toscano I., Zara L. F. (2000) Aquatic humus from an unpolluted Brazilian dark-brown stream: general characterization and size fractionation of bound heavy metals. *J. Environ Monit.* 2; 39-44.
- Ryan D K., Weber J H. (1982) Fluorescence Quenching titration for determination of complexing capacities and stability constants of fulvic acid. *Anal Chem*, 54; 986-990.
- Shuman M. S., Cromer J. L. (1979) Copper association with aquatic fulvic and humic acids. Estimation of conditional formation constants with a titrimetric anodic stripping. *American Chemical Society*, 13, 5; 543-545.
- Su, Y., Liu H., Yang J., (2012) Metals and Metalloids in the Water-Bloom-Forming Cyanobacteria and Ambient Water from Nonquan Coast of Taihu, China. *Bull Environ Contam Toxicol*, 89: 439-443. Doi:10.1007/s00128-012-0666-z
- Thurman E. M. Malcom R. L. (1981) Preparative isolation of aquatic humic substances. *Environ. Sci. Technol*, 15, 4, 463-466. Doi.org/10.1021/es000086a012
- Xue H., Kistler D., Sigg L. (1995). Competition of copper and zinc for strong ligands in a eutrophic lake. *Limnol. Oceanogr*, 40, 6; 1142-1152.
- Zapata G. M C., Solís J LG., (2013) Axolotl: El auténtico monstruo del lago de Xochimilco. *Kuxulkab*. 19, 36:41-46.

<https://doi.org/10.22201/igeof.00167169p.2022.61.1.2189>

PROJECTION OF LAND USE TO 2030 AND ITS IMPACTS ON WATER AVAILABILITY IN A BRAZILIAN SUB-BASIN: A LCM AND SWAT APPROACH

Adriana Paulo de Sousa Oliveira^{1*}, Rafaela Ribeiro Gracelli¹, Arthur Amaral e Silva¹, Vitor Juste dos Santos¹, Jackeline de Siqueira Castro¹ and Maria Lúcia Calijuri¹.

Received: August 2, 2021; accepted: December 13, 2021; published on-line: January 1, 2022.

RESUMEN

Los cambios en el uso y la cobertura del suelo pueden resultar en cambios significativos en el régimen del flujo de una cuenca hidrográfica. Los estudios predictivos sobre el uso del suelo y su interferencia con la disponibilidad del agua ayudan a identificar eventos extremos con anticipación a fin de proponer medidas de gestión adecuadas. De esta forma, este estudio tuvo como objetivo realizar la predicción del uso del suelo para el año 2030 para la subcuenca del Alto Río Grande (ARG), ubicada en el sureste de Brasil. Esta región fue elegida por el uso intenso de los recursos hídricos y por haber enfrentado, recientemente, escasez de agua como resultado de sequías prolongadas y una gestión inadecuada de los recursos hídricos. Para la predicción del uso del suelo en 2030 se utilizó el Land Change Modeler (LCM), el mapa obtenido se insertó en el modelo Soil and Water Assessment Tool (SWAT) previamente calibrado y validado para las condiciones ambientales y climáticas de la región. La subcuenca ARG fue afectada por fuertes lluvias en 2011 que resultaron en cambios en el paisaje debido a deslizamientos de tierra. Esta particularidad de la región contribuyó para que la predicción del uso del suelo para el año 2030 presente un aumento de bosques y pastos en detrimento de las áreas agrícolas. Al evaluar los impactos de estos cambios en la disponibilidad del agua, se observó que el modelo SWAT presentó, para las mismas condiciones de precipitación, una reducción en los caudales pico de hasta 59% y una reducción en el caudal promedio mensual de hasta 63% en 2030 en relación con el uso del suelo observado en 2017. Es decir, este estudio hace un aporte importante al identificar una reducción considerable en la disponibilidad del agua. Estos resultados ayudarán a formular estrategias para la gestión de los recursos hídricos y la adopción de medidas para promover la seguridad hídrica en la región.

PALABRAS CLAVE: Modelamiento de cambio de uso del suelo, predicción del escurrimiento, modelamiento de cuencas hidrográficas y recursos hídricos.

*Corresponding author at adrianasousaesa@hotmail.com

¹Federal University of Viçosa, Department of Civil Engineering, Advanced Environmental Research Group – nPA, 36570-900, Brazil

ABSTRACT

Changes in land use and land cover (LULC) can result in significant changes in a hydrographic basin flow regime. Future projections about LULC and its interference with water availability help to identify extreme events in advance and help propose appropriate management measures. Thus, this study aimed to make the LULC projection for the year 2030 for the Alto Rio Grande (ARG) sub-basin, located in Southeastern Brazil. This region was chosen because of its intense water resources use and for having recently faced water scarcity as result of prolonged droughts and inadequate water resources management. To identify the LULC trend for the year 2030, the Land Change Modeler (LCM) was used, the map obtained was inserted in the Soil and Water Assessment Tool (SWAT) model previously calibrated and validated for the region' environmental and climatic conditions. The ARG sub-basin was affected by heavy rains in 2011, which resulted in changes in the landscape due to landslides. This particularity of the region contributed to the projection of LULC for the year 2030 to present an increase in forest and pastures to the agricultural areas detriment. When evaluating the impacts of these changes in water availability, it was observed that the SWAT model presented, for the same rainfall conditions, a reduction in peak streamflows of up to 59% and a reduction in the average monthly flow of up to 63% in 2030 in relation to the LULC observed in 2017. Thus, this study provides an important contribution by identifying a considerable reduction in water availability. These results will help to formulate strategies for water resources management and the adoption of measures to promote water security in the region.

KEY WORDS: land change modeler, projection flow, watershed modelling and water resources.

INTRODUCTION

Land use and land cover (LULC) changes are factors that alter the hydrological processes in river basins, with adverse effects on flow regime and water balance. Studies carried out in different regions of the world have shown that forested areas to pastures or urban areas conversion decreases evapotranspiration, increases runoff, reduces infiltration and groundwater recharge (Anand *et al.*, 2018; Gabiri *et al.*, 2019; Jodar-Abellan *et al.*, 2019; Natkhin *et al.*, 2015; Zhang *et al.*, 2020). These changes can result in biodiversity losses, in addition to threatening socioeconomic development (Andrade *et al.*, 2019; FAO, 2011; Joly *et al.*, 2019; Marques *et al.*, 2019). Since half-billion people around the world face severe water scarcity throughout the whole year (Hoekstra, 2016), predicted flow rate has been a key driver to appropriate management measures. In this context, it is essential to project future scenarios to identify possible LULC and their consequences in flow regimes.

This is not a trivial task and requires sophisticated techniques application that take into account the LULC dynamic and the hydrological processes complexity. The integration of LULC prospecting and hydrological simulation models closely related to Geographic Information Systems (GIS) are indicated for this function. This integration allows the definition of LULC scenarios considering a pattern of changes and the simulation of current and future interferences in the water resources flow in response to these changes (Anand *et al.*, 2018; Van Cauwenbergh *et al.*, 2018).

The Land Change Modeler (LCM) is a tool for land planning (Eastman and Toledano, 2018). In LCM, the LULC is modelled empirically as a function of a set of explanatory spatial variables (whether constraints or incentives) and an observed rate of change between two distinct periods

(Kafy *et al.*, 2020; Mas *et al.*, 2014). To assess LULC hydrological impacts, process-based hydrological models, such as the Soil and Water Assessment Tool (SWAT) are being applied in different scales hydrographic basins, in countries with varied climatic and topographic conditions and with limited data quantity and quality (Bieger *et al.*, 2013; Jodar-Abellan *et al.*, 2019; Joorabian Shooshtari *et al.*, 2017; Krysanova and White, 2015; Marhaento *et al.*, 2018; Natkhin *et al.*, 2015; Piniewski *et al.*, 2019; Saha *et al.*, 2019; Zhang *et al.*, 2020, 2018).

By considering the hydrographic basin characteristics (such as soil type, topographic data, climate information and land use maps), the model is able to adequately represent water availability (Krysanova and White, 2015). This capacity together with the possibility of inserting land use maps allows SWAT to be used to project the impact of changes in LULC on the flow of a water body. However, this multi-model approach through the joint use of LCM and SWAT is developing and there are few studies reporting this interaction.

On the other hand, the results obtained so far reveal the great potential of this application. Joorabian Shooshtari *et al.* (2017) elaborated a prospective LULC map for 2050 using LCM and identified the changes in interferences observed in runoff using SWAT. Authors found that the projected change for land use is relatively small, so the impact on discharges is also modest (annual increase of 3%), but not negligible. Abbasi *et al.* (2021) in a similar study, applied the LCM to the 2032 LULC projection and determined the impacts on green water safety using SWAT. The results obtained by the authors showed an increase in pastures and urban area while forests and agricultural area reduced. These changes, associated with the most critical climate change scenario, resulted in a reduction of about 9% in green water flow and 44% in green water storage for the study region.

In tropical regions, such as Brazil, hydrological processes differ from other regions due to higher energy inputs and rates of change (Wohl *et al.*, 2012). The consequences of these changes and the knowledge of the main hydrological interactions is limited (Wohl *et al.*, 2012), which makes it difficult to adopt effective measures to guarantee water availability in the future. Brazil's economy is heavily dependent on water resources. The country stands out in agricultural production and has almost 7 million hectares of irrigated area with an expected increase of 3 million hectares by 2030 (ANA, 2017). Additionally, about 90% of Brazilian energy is supplied by hydroelectric plants (Pineiro *et al.*, 2019).

Thus, the main motivation of this work is to advance in research regarding the joint use of the LCM and SWAT models to project water availability, contributing, together with society and the scientific community, in increasing the database related to the application of these two models. For this assessment, the ARG sub-basin located in South-eastern Brazil was chosen, a region that has an intense water resources use and that recently faced one of the biggest water crises in its history. In addition, mass movements providing significant changes in the landscape affected the region.

MATERIALS AND METHODS

1. STUDY AREA

The study area comprises the ARG sub-basin (Figure 1), located in the western portion of Nova Friburgo county, in the mountain region of Rio de Janeiro state, Brazil. ARG sub-basin has an area of 236 km², which corresponds to 25% of Nova Friburgo county total area, with Rio Grande as its main watercourse. It is composed of forest remnants (62%), pastures and agricultural areas, which

represents 36% of the total area. There are no urban areas in the basin and the Nova Friburgo municipality is about 12 km away (MapBiomias, 2018). ARG sub-basin has mainly Cambisol soils, which is usually associated with undulating mountain relief areas (Zaroni and Santos, 2018).

The municipality, inserted in the Atlantic Forest biome, rated as Montane Ombrophilous Dense Forest. This region presents rugged topography and high slopes, reaching 2,300 m. According to the Köppen classification, the climate is tropical altitude (Cwb). The average annual minimum and maximum temperatures are respectively 14.5°C and 25.10°C and annual rainfall average is around 2,000 mm, with November to March being the rainiest period and April to October the driest months (Baptista, 2009; INMET, 2021). This study site was chosen because the region has been affected by critical water scarcity events resulting from prolonged droughts and inadequate water resource management (Britto *et al.*, 2018).

ARG sub-basin is responsible for meeting the demand in the metropolitan region of Rio de Janeiro, with agricultural crops such as vegetables. Those cultures demand frequent irrigation (through abstractions in Rio Grande River), which places the municipality in a prominent position in relation to the total irrigated area, being the fourth largest in the State. Rio Grande River's source is still used for animal consumption, sand extraction, distilled beverages manufacture and aquaculture (AGEVAP, 2014, 2013; IBGE, 2017; INEA, 2020). Since the Rio Grande River is also used for public water supply estimated at 185 thousands of inhabitants (IBGE, 2017), population growth expectations

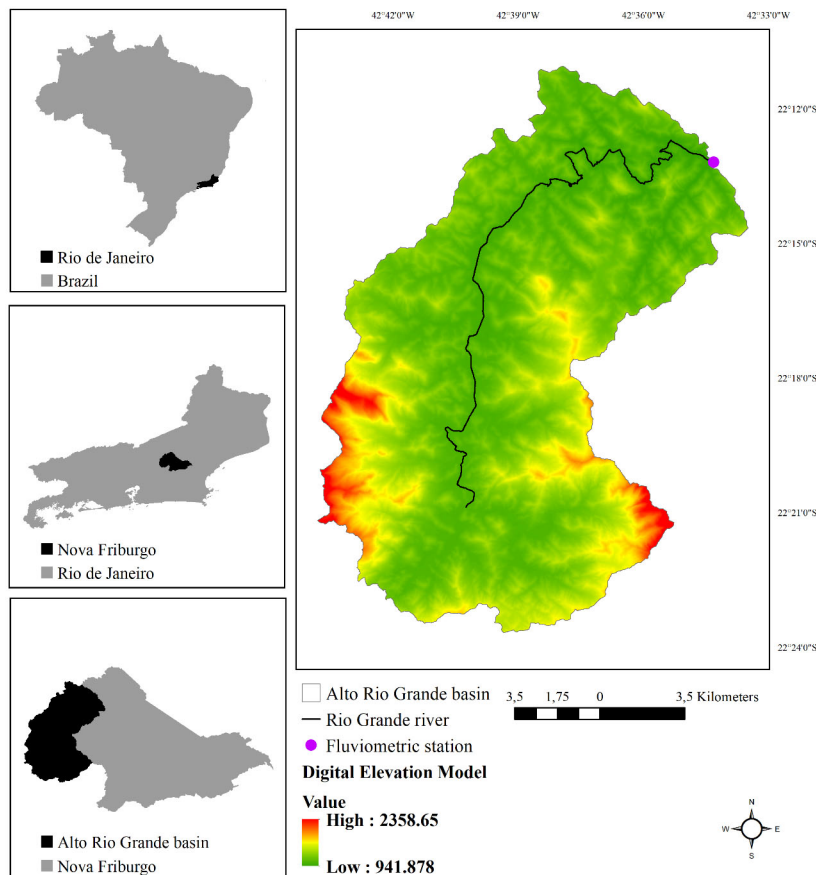


Figure 1. Study area location

and agricultural and industrial expansion call attention to water availability, with the risk of a considerable reduction, not only due to the increase in water demand, but also due to LULC.

This work aimed to determine water availability in the ARG sub-basin for the year 2030 in response to LULC. To achieve these objectives, the LCM tool was applied to identify possible LULC in 2030. The image for 2030 obtained was inserted in the SWAT model to obtain flow regime in Rio Grande (Figure 2). At this stage, it was considered that the lowest rainfall observed in the ARG sub-basin will occur again, simulating a critical scenario in terms of water availability. For this analysis, LULC in 2030 used for all years in the future. Year 2030 was adopted because the national and regional agencies, responsible for water resources management, use this range for some demand projections (ANA, 2017; INEA, 2014), therefore, determining water availability for 2030 consists, among others, in an opportunity to assist decision makers.

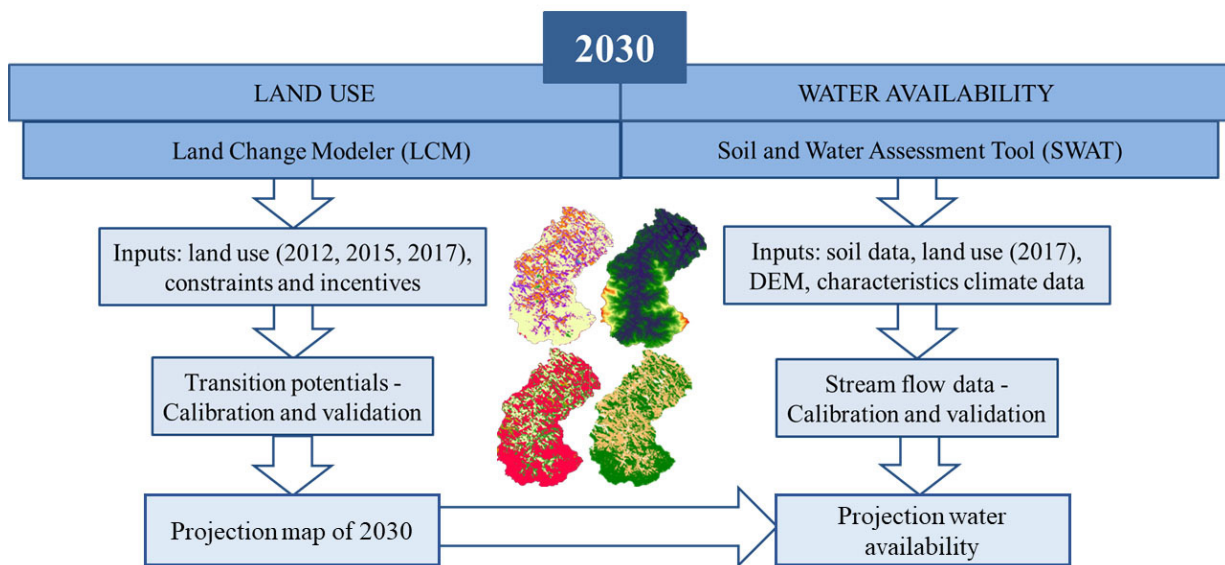


Figure 2. Flowchart of the methodology used in this study

2. LAND CHANGE MODELER (LCM)

LCM is an Idrisi Selva software (currently TerrSet) tool developed by Clark Labs of Clark University and consists of a spatially explicit dynamic model, based on an inductive pattern. The LCM is a LULC projection tool that uses historical land cover change to model the relationship between land cover transitions and explanatory variables to map future scenarios (Eastman and Toledano, 2018). This process of LULC modelling is organized into major stages that include: change analysis; transition predictions; validate and future projection.

Change analysis: LCM models LULC considering a rate of change observed between two different periods and a set of explanatory variables. In this study, the rate of change was defined using land cover maps for the years 2012 and 2015. These years were selected because on January 11 and 12, 2011, an anomalous precipitation (253 mm in 37 h) triggered mass movements in the region where Nova Friburgo is located. These mass movements caused significant changes in the landscape, great

social and economic damage that gave a new dynamic of LULC in the region which must be known and projected for proper management.

The ARG sub-basin LULC map used as input data into the LCM were obtained from the Annual Land Cover and Land Use Mapping Project of Brazil (MapBiomias). Produced by a pixel-by-pixel classification of Landsat satellite images. The LULC classes were adapted to “Forest” which includes planted and native forests, being the second most present land cover; “Pasture”; “Waterproofed areas” which include rural dwellings and rocky outcrops; and the “Mosaic of agriculture and pasture”. The last category results from the difficulty in differentiating between certain agricultural crops and the grasses that compose the pastures, allowing possible spatial inconsistencies in the classifications (MapBiomias, 2018).

After inserting the LULC images in the LCM, on the Change Analysis tab it is possible to identify the changes that occurred between the evaluated years (2012 and 2015), such as the gains and losses for each LULC class.

Transition potential: at this stage, the model is structured and the areas with the greatest potential for transition are identified. For this, the variables that can act as LULC drivers are selected and tested according to their explanatory power and include incentives and constraints. In this study, roads and highways digital maps were used, since the distances from them are factors that may favour or limit the expansion of a given land use category. Federal and state conservation units’ maps were included in the modelling as constraints, especially the agriculture and pasture expansion. Table 1 presents the data used in the models and their source, which were pre-processed using the ArcGis™ 10.5 software from ESRI®.

Other variables used in LCM were predictors and consisted of elevation, slope and distance to Rio Grande River, distance to conservation areas, distance to mosaic of agriculture and pasture and distance to roads. These variables were adopted because, in a previous analysis (Cramer V), they were the most relevant and reached a minimum accuracy of 75% when tested in the multilayer perceptron (MLP), an artificial neural network model as can be seen in section 3.2. Cramer V determines the

Table 1. Digital maps used in LCM

Variables	Data source	Scale
Land use	MapBiomias Project, 3 rd collection (http://mapbiomas.org)	spatial resolution: 30m
Topography	Brazilian Institute of Geography and Statistics - IBGE (https://downloads.ibge.gov.br/downloads_geociencias.htm)	1:25000
Hydrography	National Water Agency - ANA (http://metadados.ana.gov.br/geonetwork/srv/pt/main.home)	1:25000
Roads and highways	Department of Roads and Roadways of the State of Rio de Janeiro (http://www.der.rj.gov.br/mapas_n/index.htm)	1:450000
Conservation units	State Institute of Environment (http://www.inea.rj.gov.br/cs/groups/public/@inter_dibap/documents/document/zeww/mtiz/-edisp/inea0123058.pdf)	1:1100000

association between two variables with a value of 0 representing no association (complete independence) and a value of 1 representing complete association (dependence) (Boylan *et al.*, 2018).

Validation and future projection: the 2012 and 2015 maps were used for model calibration. After calibration, the 2017 forecast was made and the map obtained was compared with the real 2017 map to validate the model. Markov Chain analysis is used to generate prediction maps for the year specified. The Markovian process is a method in which a predicted system can be estimated by finding its previous state and the probability of conversion from one state to another (Nelson *et al.*, 2010).

The test accuracy or overall performance was assessed through the Area Under the Curve (AUC) index. The AUC value ranges between 0 to 1 and was calculated by the Receiver Operator Characteristic (ROC) which is used to compare the probability of an occurrence against a boolean map which shows the actual occurrences (Eastman, 2012). In the ROC curve, the horizontal axis represents the false positive rate and the vertical axis the true positive rate. AUC connects the points obtained by the various thresholds. If the true events coincide perfectly with the higher ranked probabilities, then the AUC is equal to 1 (ideal model) (Eastman, 2012; Mas *et al.* 2013). Once the model was validated, the next step was to generate the LULC map for 2030. The Change Prediction tab concludes the analysis, by defining a prediction year (Magalhães *et al.* 2020).

This work used a MLP methodology. MLP extracts samples from areas that underwent change or not from the two land cover maps provided. This method runs on automatic, making decisions on how to best use data provided to model transitions (Eastman, 2012). Decisions on the number of training samples size, number of iterations, and learning rates can be made by the user. All values used here were IDRISI’s default.

3. SOIL AND WATER ASSESSMENT TOOL (SWAT)

The Soil and Water Assessment Tool (SWAT) was developed by the US Department of Agriculture and A&M University of Texas. The steps to obtain the streamflow regime using SWAT included the insertion of the data used in the modelling (Table 2), followed by the discretization of 32 parameterized sub-basins in 271 hydrological response units (HRUs). A HRU is the basic unit where the hydrological components were simulated, aggregated for each sub-basin and routed to the basin outlet throughout the channel network (Arnold *et al.*, 2012). For data standardization, this work used downscaling (Zhou *et al.*, 2015).

Table 2. Input data entered in SWAT

Variables	Data source	Scale
DEM	Obtained from topography and hydrography from the tool Topo to Raster application on ArcGis 10.5 software.	1:25000
Precipitation	National Water Agency – ANA (http://metadados.ana.gov.br/geonetwork/srv/pt/main.home) (stations 02242009 e 02242022)	-
Air temperature, solar radiation and relative humidity	Global Weather Database (https://swat.tamu.edu/media/99082/cfsr_world.zip)	-
Soil map	Brazilian Institute of Geography and Statistics – IBGE (ftp://geoftp.ibge.gov.br/informacoes_ambientais/pedologia/vetores/brasil_5000_mil)	1:5000000
Land use	MapBiomias (http://mapbiomas.org/)	spatial resolution: 30m

The subsequent steps were warm-up, sensitivity analysis, model parameters calibration, validation and future scenarios simulation. In this phase was applied the software SWAT-Calibration and Uncertainty Programs (SWAT-Cup) and the algorithm Sequential Uncertainty Adjustment (SUF12). SUF12 function performs the sensitivity analysis that minimizes the uncertainties imposed by the model parameters variations (Abbaspour *et al.*, 2007; Narsimlu *et al.*, 2015). The algorithm was adopted because it needs a minimum number of model simulations to obtain high quality calibration and uncertainty results (Narsimlu *et al.*, 2015).

In order to obtain data with high percentages for calibration, as Andrade *et al.* (2012) and Narsimlu *et al.* (2015) did, were used in this stage the data related to 70% of the historical series (1966-2003), the remaining (30%) was applied in validation (2004-2018). The first 5 years of the model were set aside for the warm-up period required by the system stabilization to reduce systematic error. The time scale used in all stages was monthly because the daily-simulated data may be less accurate and in an analysis with a longer period, the hydrological processes tend to be more stable (Pontes *et al.*, 2016).

In the calibration and validation results evaluation, the Nash and Sutcliffe (NS) model efficiency coefficient, the coefficient of determination (R^2) and the percent bias (PBIAS) were used. NS values vary from infinity to 1, PBIAS evaluates the tendency of the simulations as being higher or lower than the observed data, positive PBIAS indicates an overestimation while a negative value indicates an underestimation (Zhang *et al.*, 2020). PBIAS is defined as satisfactory when obtaining values lower than ± 10 (Moriassi *et al.*, 2007). R^2 and NS values greater than 0.5 classify as satisfactory and equal of 1 corresponds to a perfect match (Moriassi *et al.*, 2007; Sao et al, 2020). NS, PBIAS, and R^2 were calculated as follows (Equation 1, 2 and 3):

$$PBIAS = 100 \left(\frac{\sum_{i=1}^N (Q_{sim,i} - Q_{obs,i})}{\sum_{i=1}^N (Q_{obs,i})} \right) \quad \text{Equation 1}$$

$$NSE = 1 - \frac{\sum_{i=1}^N (Q_{obs,i} - Q_{sim,i})^2}{\sum_{i=1}^N (Q_{obs,i} - Q_{obs}^-)^2} \quad \text{Equation 2}$$

$$R^2 = \frac{\left[\sum_{i=1}^N (Q_{obs,i} - Q_{obs}^-) (Q_{sim,i} - Q_{sim}^-) \right]^2}{\sum_{i=1}^N (Q_{obs,i} - Q_{obs}^-)^2 \sum_{i=1}^N (Q_{sim,i} - Q_{sim}^-)^2} \quad \text{Equation 3}$$

Where Q_{obs} and Q_{sim} are the observed and SWAT simulated streamflow (m^3/s), and Q_{obs}^- and Q_{sim}^- are the mean observed and SWAT simulated streamflow (m^3/s), respectively; N is the number of samples, and i is the *ith* sample (Zhang *et al.*, 2020).

After model calibration and validation, a new simulation to identify streamflow data, for the period of 2019 to 2030, were carried out. An increase in precipitation is expected for the region where the ARG sub-basin is inserted as a consequence of climate change (Magrin *et al.*, 2014), with an increase of 6% until 2039 (Barata *et al.* 2020). So, this study does not consider climate projections to inform future precipitation as the expected increase is low for the near future (2030). Instead, the historical precipitation data used was the same of 2007 to 2018 (measured by rain gauge), because this period recorded some of the lowest annual accumulated precipitation values, thus representing the most critical scenario in water availability terms.

To obtain LULC maps applied in the new simulation, authors used the LCM tool for 2030. The other parameters such as the DEM and the soil type map were the same as those entered in the first modelling because there are not significant changes on surface relief and soil typology occurred within the analysed time series. In other words, in order to achieve the objectives of this study, simplification was necessary by fixing some parameters (soil type, relief, precipitation) and only LULC was varied.

RESULTS

1. CURRENT LULC AND WATER AVAILABILITY

In 2017, forest category predominates in the ARG sub-basin occupying 62% of the total area, mainly in higher altitude sites where the conservation units are located predominantly. Unlike the mosaic of agriculture and pasture (19% of the total area) and pasture (16% of the total area) were located in the flattest sites such as the Rio Grande River and its tributaries.

Regarding water availability, Figure 3A illustrates the annual minimum flows registered at least once in Rio Grande between 1966 and 2018. From this time series, it is possible to observe that smaller flows occurred in the 70s and in the recent years of 2014, 2015, 2017 and 2018, where values lower than average (2.5 m³/s) were found. The lowest flow recorded in the entire historical series was in 2015 (1.00 m³/s, occurring only once), followed by 2017 (1.24 m³/s, flow recorded during three consecutive days). In these years, one of the lowest annual accumulated precipitation since 1995 was recorded, reaching 856.5 mm in 2014 (Figure 3B).

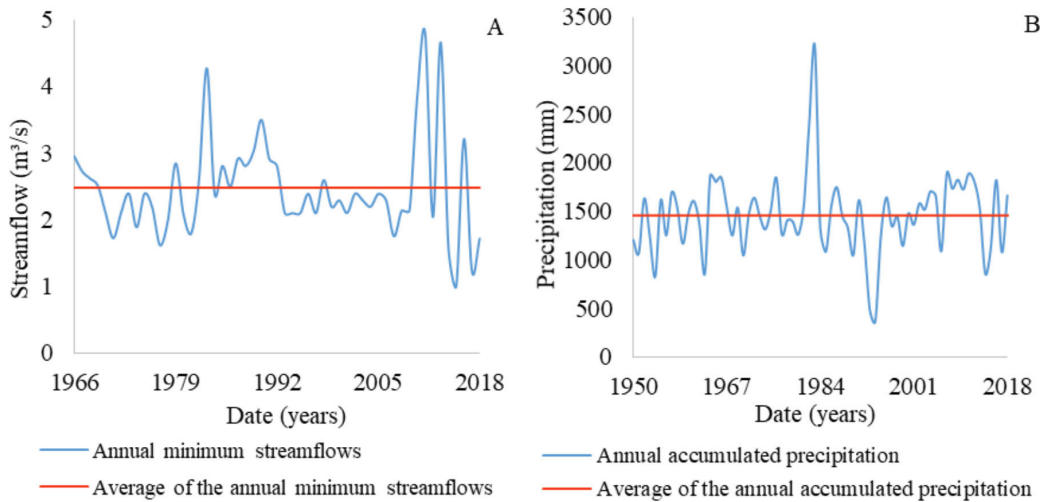


Figure 3. Minimum flows observed in Rio Grande between 1966 and 2018 (A) and annual accumulated precipitation between 1950 and 2018 (B).

3.2 PROJECTION OF LULC AND WATER AVAILABILITY FOR THE YEAR 2030

All the variables were tested, using Cramer V’s analysis (Table 3) and selected for the transition sub-model, that is, the transition probability between LULC categories. To determine the transition potential, a neural network was used, as this is the method that presented the best performance (Lin

et al., 2011; Sangermano *et al.*, 2012). According to Akoglu (2018), Cramer V is used to measure association strength between two or more variables. It varies between 0 and 1, a value close to 0 means no association between variables and values close to one indicates a strong association between the variables.

Table 3. Predictor variables used in LCM and Cramer's V values

Variables predictors	Cramer V
Elevation	0.1692
Slope	0.1961
Distance to Rio Grande river	0.1386
Distance to conservation areas	0.2037
Distance to mosaic of agriculture and pasture	0.2793
Distance to roads	0.1948

Cramer V's analysis does not limit the use of a given variable. The values obtained in this analysis only indicate the association degree between the variables, however, even having a value considered low, since the variable is determined to be important for the studied transition, it can be used regardless of the Cramer V value obtained (Akoglu, 2018). Thus, in addition to considering the Cramer's V values, the selection of variables considered the minimum accuracy of 75% (Magalhães *et al.* 2020) using MLP.

The methods applied for LCM validation presented high values, with AUC equal to 0.85. AUC values between 0.7 and 0.8 are considered acceptable, 0.8 to 0.9 is considered excellent, and more than 0.9 is considered outstanding (Mandrekar 2010). The excellent performance of the LCM can be observed in Table 4, where the greatest difference between the projected and observed LULC for 2017 was 1.1 km² and occurred for the forest category. From the digital maps and the LCM application, it was possible to obtain the LULC map for 2030 (Figure 4) and losses and gains for each category (Figure 5). There was a decrease of only 0.3 km² in area for the waterproofed areas category between 2017 and 2030. In contrast, there was an increase in area for the forest category (7.6 km²) followed by the pasture (3.9 km²). Mosaic of agriculture and pasture was the category that most contributed to the expansion of forests and pastures, with a reduction from 45.4 km² in 2017 to 34.2 km² in 2030.

Table 4. Areas in km² for the LULC observed in the Alto Rio Grande sub-basin

Land use categories	2012	2015	2017 observed	2017 projected	2030
Forest	145.1	143.3	147.3	146.2	154.9
Pasture	44.2	38.5	38.6	39.6	42.5
Agriculture and pasture	41.4	49.8	45.4	45.8	34.2
Waterproofed areas	5.3	4.4	4.7	4.4	4.4
Total	236.0	236.0	236.0	236.0	236.0

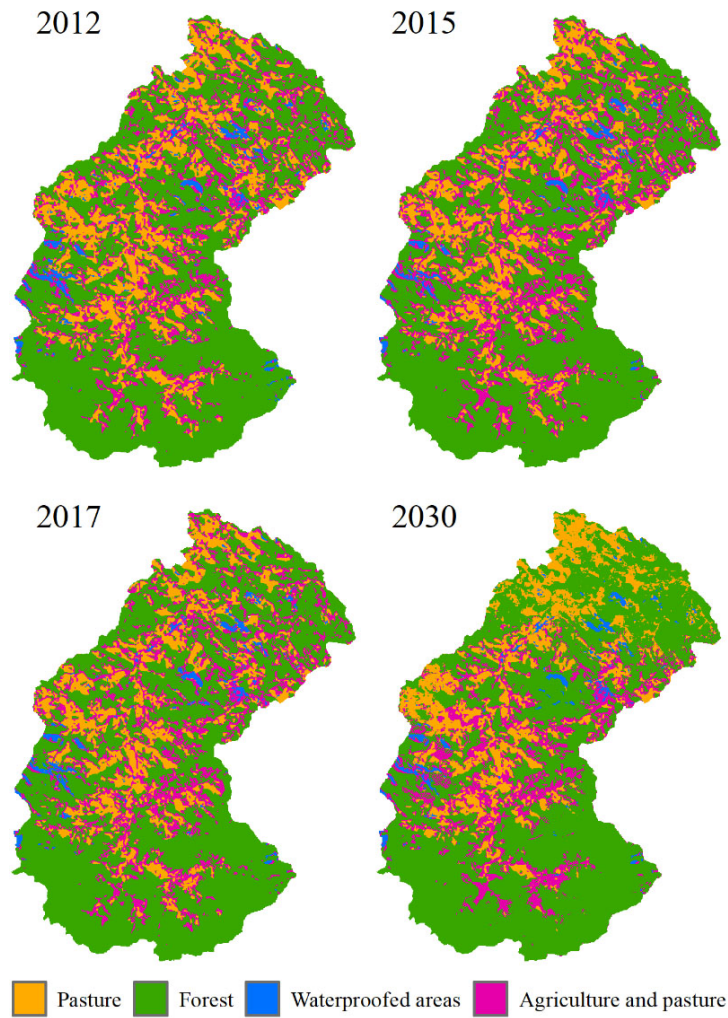


Figure 4. Land use and land cover for Alto Rio Grande sub-basin considering the years 2012, 2015, 2017 and the projection for 2030

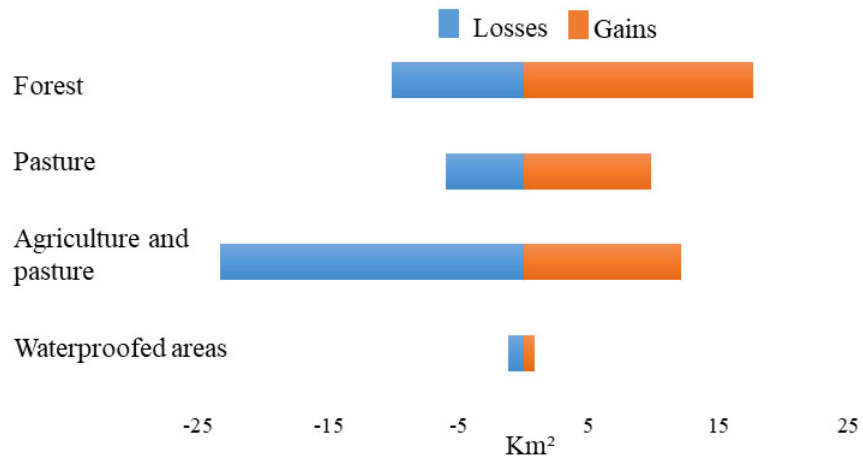


Figure 5. Land use and land cover transition matrix from 2017 - 2030 with losses and gains

Figure 6 shows the expected changes between 2017 and 2030 for each LULC category. The south of the ARG sub-basin is the region where some conservation units are located and therefore no changes are expected since this location was included in the modeling as a restriction of anthropogenic use. For the other categories, it is possible to observe that the most significant changes actually occurred with the conversion of agricultural areas to pasture and forests. It is also possible to observe a displacement of agricultural areas that moved from the north of the sub-basin to the central region.

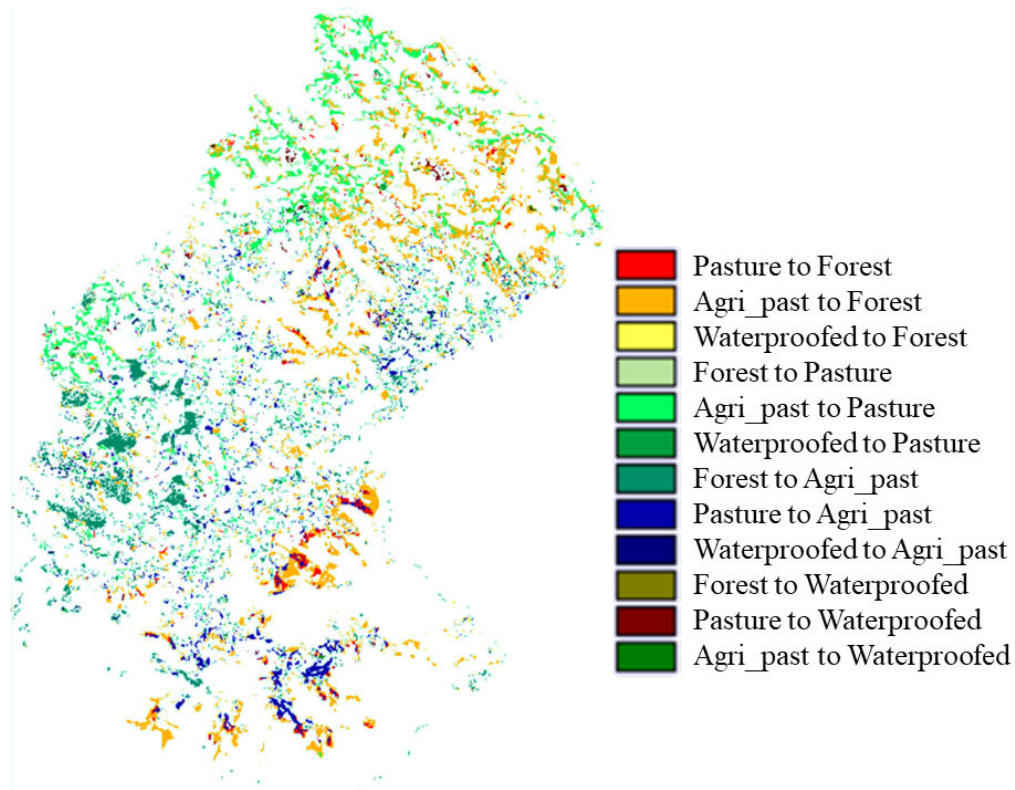


Figure 6. Trend of land use and land cover dynamics for 2017 - 2030

Table 5 presents the hydrological modelling performance executed in SWAT and Figure 7 shows the observed versus simulated streamflow for the validation and simulation steps and R^2 values. The rates of NS and R^2 values were greater than 0.5, being considered satisfactory in both the calibration and validation steps (Moriassi *et al.*, 2007; Sao et al, 2020). PBIAS value is considered very good for calibration step ($< \pm 10$) and unsatisfactory for validation step ($\geq \pm 25$) (Moriassi *et al.*, 2007) which indicates that 37.6% of the monthly values flow rates were underestimated.

In Figure 8 it is possible to observe this behaviour in the validation step (2004 - 2018). The periods where the flow rates in Rio Grande were lower; there was a greater discrepancy between the observed and simulated values. It is also possible to observe the difficulty of the model in simulating flow peaks, presenting underestimated values. It is possible to observe also that the biggest discrepancies between the observed and simulated values occurred in the years 2011 to 2013.

In this study, only LULC was varied in the SWAT model while the other variables were fixed. Thus, it is possible to counteract, for example, the same rainfall conditions and the flow in Rio Grande

Table 5. Monthly performance assessment indices of the SWAT model

Parameters	Calibration (1966-2003)	Validation (2004-2018)
R ²	0.64	0.82
NS	0.63	0.54
PBIAS (%)	2.1	37.6

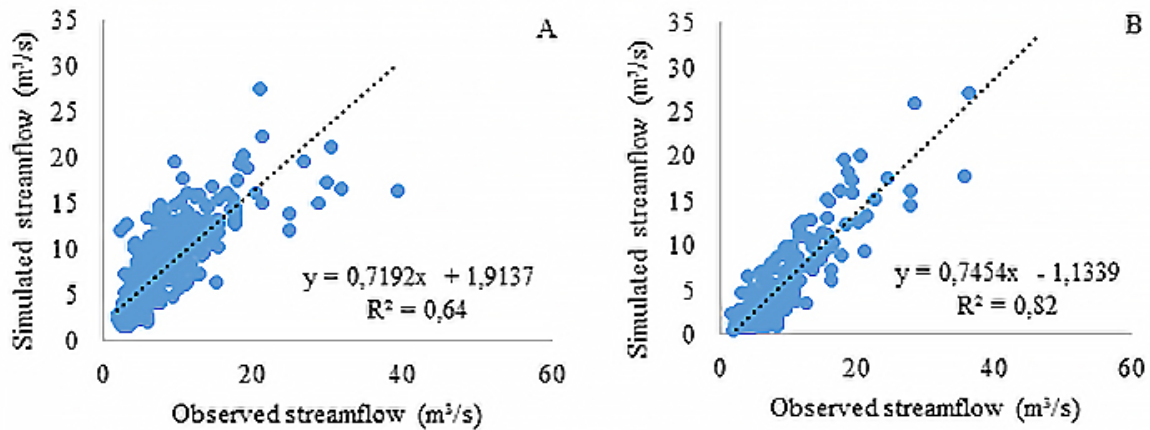


Figure 7. Observed versus simulated monthly streamflow for calibration (A) and validation step (B)

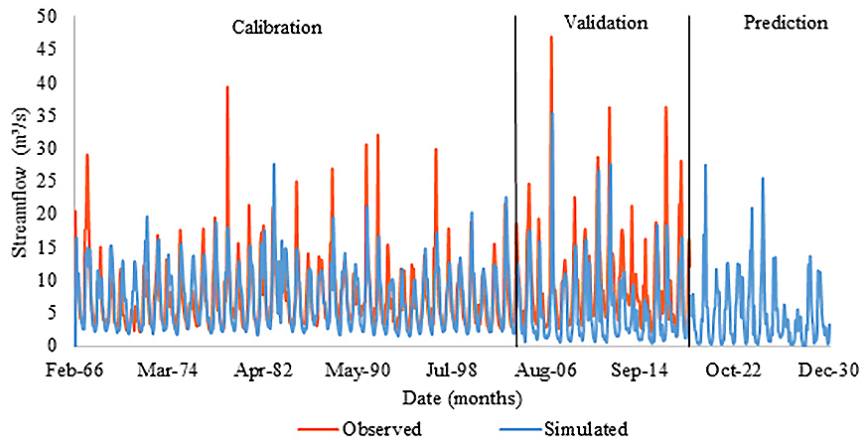


Figure 8. Monthly-simulated streamflows observed (blue) and simulated (red) in Rio Grande

considering the land use observed in 2017 and projected for 2030. By making this comparison, it was possible to observe a reduction in peak stream-flows of up to 59% in 2030. Moreover, it was found that for the land use projected for 2030 there would be a reduction in the average monthly flow of up to 63% in relation to the observed flow considering the land use of 2017. Another characteristic was the lower variation in flow over the year when comparing the estimated flows for land use projected for 2030 with the land use observed in 2017. For the same annual accumulated precipitation of 1661.6 mm, the monthly flows observed considering the land use of 2017 and 2030 varied

between 2.4 and 27.7 m³/s (amplitude of 25.3 m³/s) and between 0.4 and 11.3 m³/s (amplitude of 10.9 m³/s) respectively.

These results are accompanied by a reduction in flow in Rio Grande for the next 10 years, both in the dry and rainy season. The most critical condition will occur if the precipitations observed in 2014 are repeated (lowest annual accumulated precipitation, 856.5 mm). In this scenario, minimum flows have reached values close to zero while maximum flow will be below 6.0 m³/s. It is important to note that an underestimation may have occurred because the model underestimated the flows in the validation step.

DISCUSSION

The ARG sub-basin is inserted in the Atlantic Forest biome, which suggests that, before colonization, the region's main land cover was forests. After colonization, there were changes to other uses, such as pastures and agriculture, which occurred in the smallest slopes observed in the ARG sub-basin. The steeper areas present limitations on agricultural mechanization because they affect the machines stability and the movement speed. It also does not indicate high declivities for raising animals, and may adversely affect growth and production. This characteristic restricts the anthropogenic use of conservation areas, which are predominantly located in higher altitude regions, and favour the maintenance of forests.

The LULC contributed to reducing water availability in recent years in the ARG sub-basin. The increase in potentially agricultural areas in 2015 probably resulted in an increase in the water consumption applied to irrigation activities which, added to the reduction in precipitation in the previous year, caused the decrease of groundwater stocks (decrease in the amount of groundwater) and a significant reduction in flow levels in the ARG sub-basin (Figure 3). In this way, the LULC associated changes in precipitation contributed to reducing water availability this year. This scenario highlights the need to identify future water availability considering the changes that will occur in LULC.

The LCM was applied in the elaboration of a prospective LULC map for the year 2030 (Figure 4). The statistical indice obtained in the validation stage indicated that the model showed excellent projection capability. For example, there was little variation in area for the waterproofed areas category between 2017 and 2030 (Table 4), which is consistent, as this category includes rocky outcrops that are less sensitive to anthropogenic actions compared to other uses.

On the other hand, an increase in the forests category was observed. It is possible to list three main factors that explain this behaviour. First (i), there were significant changes in the region's landscape after the 2011 disaster. Some affected sites have been converted from forests to exposed soil. In the following years, a gradual forest restoration was observed. Precisely the land use maps for that period were used as inputs in the LCM. LCM calculates rates of change in the change analysis step as well as transition potential maps to establish the LULC projection (Shade and Kremer 2019). In other words, one of the features of the LCM is to extrapolate the rate of change in LULC observed in previous years to a future scenario, for this reason an increase in forest areas was observed for the year 2030 once this increase occurred over the years used in the modelling (2012-2015).

This aspect consists of a LCM limitation, where all the events of change, extreme or not, that occur before and after the time interval adopted for calibration and validation, are not counted in the image produced (Amaral e Silva *et al.*, 2020; Marques *et al.*, 2021). In addition, LULC involves com-

plex and dynamic processes of human nature, such as social, institutional and economic processes, which can be difficult to detect for the variables and algorithms available in the models (Olmedo *et al.*, 2015).

Second explanatory factor (ii) is the inclusion of protected areas in the LCM. A study developed by the environmental agency of Rio de Janeiro showed that ARG sub-basin region has high potential for natural regeneration due to forest remnants and connectivity between them (INEA, 2018). This hypothesis is reinforced by observing one of the most significant changes projected to occur between 2017 and 2030, which will happen close to the conservation area, with the conversion of agricultural areas into forest (Figure 6). In addition, the predictor variable “distance to conservation areas” presented the second highest of Cramer’s V value (0.2037), which indicates that this predictor has a higher correlation with LULC compared to others such as ‘slope’ and ‘distance to roads’. Furthermore, a recent survey conducted in South-eastern Brazil found an increase in forest areas between 2001 and 2015 that was attributed to two main factors: change in Brazilian legislation, with New Forest Code (Law 12.651/2012) implementation and silviculture expansion (Moraes *et al.*, 2018).

A third justification (iii) refers to changes in the region's economic activities. Agriculture developed in the ARG sub-basin is practiced by family farmers, the landslides that occurred in 2011 resulted in soil fertility loss, agricultural equipment and other inputs losses and product flow pathways obstruction. The high cost associated with soil recovery and the structure existing before the disaster (Freitas *et al.*, 2012) are factors that can motivate the development of other economic activities and induce changes in the economic structure of the region. The distance from agricultural areas presented the highest Cramer’s V value (0.2793) among all the variables evaluated (Table 2), in addition it was possible to observe that the reduction of agricultural areas occurred in several places in the basin, that is, not were concentrated in a single region (Figure 6). All these characteristics are indications that reinforce the hypothesis of a change in the economic activity developed in the region (agriculture) to other practices (such as silviculture and cattle breeding). When projecting LULC for 2050 in a watershed located in China, Wu *et al.* (2018) also observed an increase in forest and pasture areas to the detriment of agricultural regions. The authors attributed these results to environmental protection policies and changes in the local economy.

Considering the main LULC changes expected for the ARG sub-basin in 2030 (reduction in the mosaic of agriculture and pasture category, which was accompanied by an increase in forests and pasture areas) (Table 4 and Figure 4), it is possible to make some inferences in hydrological components. For example, the decrease in the potentially quantified agricultural areas does not necessarily represent a reduction in the water demand in this activity because there is expected an increase in irrigation in Brazil (Cunha *et al.*, 2014).

The conversion of agricultural areas into pasture can provide greater surface runoff as there is less infiltration due to soil compaction by cattle, which can result in flow peaks. Conversely, the conversion of agricultural areas to forest can reduce runoff due to interception, presence of litter and infiltration. Therefore, an increase in base flow and a decrease in flow peaks can be observed, this behaviour is accompanied by an intensification of evapotranspiration, which may also reflect a lower flow in rivers. It is important to note that although pastures or agricultural crops increase the supply of readily available water in a basin, this is not an environmental benefit, as forests act in the maintenance of the minimum flow, in protecting the soil against erosion and transport of sediments. The effects

of LULC on hydrological components is a complex issue as the variables that control hydrological behaviour are many and interdependent, for this reason the SWAT model was applied.

As for the hydrological model, it is common for the statistical validation period indexes to be less satisfactory compared to the values obtained in calibration. This is because parameters are optimized specifically for calibration period and the period used in validation may present different conditions (Fukunaga *et al.*, 2015). This is the case in this study (Table 5), the lower performance in the validation stage can be attributed to the precipitation data used. When calibration and validation periods are similar, better results can be obtained. In this study, this did not occur because the period of less precipitation was accumulated in the final years of the historical series (2007 a 2018). Other ARG sub-basin particularities, such as changes in relief resulting from landslides, might also have interfered with validation performance. As shown in Figure 8, the biggest discrepancies between the observed and simulated values corresponds to the year of the disaster and the following two years.

Furthermore, ARG sub-basin has only one fluviometric station, so any inconsistency in recorded data may compromise the comparison between observed and simulated flows. Anaba et al (2017) obtained PBIAS of 23% at the validation stage of the SWAT model for a basin in Uganda. These results occurred since the use of poor observed data quality and to the possible occasional effluents discharge that could not be accounted for during the simulation. Lotz *et al.* (2018) also mention that the divergences between calibrated and validated values may be the result of localized precipitation not recorded in monitoring stations. However, this does not seem to be the case for the ARG sub-basin as the precipitation values available in the two pluviometric stations are similar, being that 65% of the data showed a coefficient of variation of less than 30% when compared. Another factor that can change the flow regime in a water body and compromise the performance of the SWAT model is the presence of reservoirs (Anaba *et al.*, 2017), which was not observed in the ARG sub-basin.

ARG sub-basin is located in a region characterized by the monsoon system, where a rainy and a dry period are well defined. However, it is expected that for the coming years (considering that the rainfall observed between 2007 and 2018 will be repeated), a reduction in the amplitude of the flows observed between the months of drought and rain will be reduced if compared with the land use observed in 2017. This behaviour was accompanied by a decrease in both the maximum and minimum flow observed with the identified LULC for 2030 compared to 2017 (Figure 8).

The increase in forest areas projected for 2030 plays an important role in these changes in the hydrological regime. In forested areas, an initial portion of precipitation is intercepted by vegetation; another portion reaches the ground and infiltrates what reduces surface runoff and flow peaks. On the other hand, forest vegetation also consumes water by evapotranspiration. In tropical forests, 67.6% of the precipitation was lost to the atmosphere through evapotranspiration (Leopoldo *et al.*, 1995). This water loss affects water availability. Saddique *et al.* (2020) observed a reduction in water yield of 48.32% and an increase in evapotranspiration of 51.93% in Upper Jhelum sub-basin between 2001 and 2018. The authors attributed these results to forest cover gain.

It is important to highlight that forests play an important role in promoting water infiltration into the soil and recharge of aquifers. However, this capacity can be affected by the relief and the stage of vegetation development. For the ARG sub-basin, which has more accentuated slopes, a higher flow velocity is expected which can reduce water infiltration and evapotranspiration possibly prevailed. In addition, Mendonça *et al.* (2009) mentions that for deforested regions there can be an increase

in flows in the first three years, followed by a decrease that can last from 15 to 20 years with the regeneration of the vegetation. Only after 40 to 50 years, when the plants are already mature, does the flow recover. These flow variations were attributed to greater evapotranspiration in the growth phase and to a subsequent drop with the ripening of the vegetation.

The comparative analysis of previously published work on future water projection shows that the magnitudes of LULC and their impacts on the hydrological regime are different because each region has its own characteristics. However, the behaviour trend is similar. For example, Marhaento *et al.* (2018) evaluated the future hydrological response to changes in land use in the Samin basin (Indonesia) using Markov chain, multi-criteria evaluation and SWAT. According to the authors, in 2000, 42.3% of the total area was forest. In a more conservative scenario, it is expected that by 2050 forested areas will occupy 30% and agricultural areas 52.1%. The future hydrologic response indicates a reduction in evapotranspiration which was accompanied by an increase in streamflow of up to 20%.

Another example, a study made by Abe *et al.* (2018) identified the potential future LULC impacts on the hydrological regime of the Upper Crepori River basin (Brazil) using the SWAT model. The authors considered two land use scenarios for 2050, one less conservative (50.67% of the area will be forest while 46.39% will be pasture) and another more conservative (76.22% forest and 20.84% pasture). They found that the changes expected for 2050 in the flow regime showed that the less and more conservative scenario presented increases of up to 11% and 22%, respectively, during the rainy season, and reductions of up to 19% and 32%, respectively, during the dry season. Percentages were calculated in relation to land use before the anthropic changes where the forests corresponded to 99.63% of the area.

Regional studies of LULC and water availability should be conducted in order to consider local particularities. In this context, the present research presents a worrying result, because in the case of a rainfall of less than 856.5 mm, the streamflow in Rio Grande will be close to zero. With the possibility of reducing water availability in the ARS sub-basin, adopting preventive measures is extremely necessary in order to promote water security in the region.

It is important to highlight that additional studies are needed because the aim of this study was to determine the projection of LULC for 2030 and the consequences of the projected changes on water availability considering a low rainfall scenario, as this is the most critical condition. The impacts of LULC alone on the stream flow of Rio Grande for the year 2030 was determined. Climate changes were not considered and this should be the focus of future research.

CONCLUSIONS

The changes in landscape that occurred in the ARG sub-basin in 2011 probably affected the results obtained in this study. Limitations such as LCM extrapolating the rate of forested areas recovery to the year 2030 and the changes in flow that occurred between 2011 and 2013 compromised the SWAT validation stage. Despite the limitations, results obtained in this study indicate an increase in forested areas and pastures to the detriment of agricultural areas. Due to these changes, a decrease in water availability was projected, reaching values close to zero during drought periods and a smaller amplitude between the peaks of maximum and minimum flow rates.

These results, despite presenting possible inconsistencies, will help to formulate strategies for water resources management and the adoption of measures to promote water security in the region. In

addition, the combination of the LCM and the SWAT proved to be a highly valuable tool in terms of the management and monitoring of the water availability of the regions, as it makes possible the modelling of extreme events, allowing for greater adequacy and precision to the characteristic conditions of the studied area.

ACKNOWLEDGMENTS

Coordenação de Aperfeiçoamento de Pessoal de Nível Superior - Brasil (CAPES) [Finance Code 001], supported this work.

DECLARATION OF INTEREST STATEMENT

The authors declare that they have no conflict of interest.

REFERENCES

- Abbasi A, Amirabadizadeh M, Afshar AA, Yaghoobzadeh M, 2021. Potential influence of climate and land-use changes on green water security in a semi-arid catchment. *J Water Clim Chang*. <https://doi.org/10.2166/WCC.2021.055>
- Abbaspour, K.C., Yang, J., Maximov, I., Siber, R., Bogner, K., Mieleitner, J., Zobrist, J., Srinivasan, R., 2007. Modelling hydrology and water quality in the pre-alpine/alpine Thur watershed using SWAT. *J. Hydrol.* 333, 413–430. <https://doi.org/10.1016/j.jhydrol.2006.09.014>
- Abe, C.A., Lobo, L.F., Dibike, Y.B., Costas, M.P.F., Santos, V., Novo, E.M.L.M., 2018. Modelling the Effects of Historical and Future Land Cover Changes on the Hydrology of an Amazonian Basin. *Water*, 10, 932. <https://doi:10.3390/w10070932>
- AGEVAP, 2013. Integrated Environmental Assessment of the Pomba, Muriaé, Piabanha, Paraíbuna and Preto Rivers - Paraíba do Sul River Basin – I ECOBRJ.
- AGEVAP, 2014. Elaboration of the state plan for water resources in the State of Rio de Janeiro: R2-F - Environmental characterization.
- AGEVAP, 2017. Situation Report 2017 - Rio Dois Rios Committee [WWW Document]. URL <http://cbhriodoisrios.org.br/downloads/relatorio-de-situacao-2017.pdf> (accessed 6.15.20).
- Akoglu, H., 2018. User's guide to correlation coefficients. *Turkish J. Emerg. Med.* 18 (3): 91–93. <https://doi.org/10.1016/j.tjem.2018.08.001>
- Amaral e Silva, A., Braga, M.Q., Ferreira, J., Juste dos Santos, V., do Carmo Alves, S., de Oliveira, J.C., Calijuri, M.L., 2020. Anthropogenic activities and the Legal Amazon: Estimative of impacts on forest and regional climate for 2030. *Remote Sens. Appl. Soc. Environ.* 18, 100304. <https://doi.org/10.1016/j.rsase.2020.100304>
- ANA, 2017. Atlas Irrigation [WWW Document]. URL <http://atlasirrigacao.ana.gov.br/> (accessed 6.15.20).
- Anaba, L.A., Banadda, N., Kiggundu, N., Wanyama, J., Engel, B., Moriasi, D., 2017. Application of SWAT to Assess the Effects of Land Use Change in the Murchison Bay Catchment in Uganda. *Comput. Water, Energy, Environ. Eng.* 06, 24–40. <https://doi.org/10.4236/cweee.2017.61003>
- Anand, J., Gosain, A.K., Khosa, R., 2018. Prediction of land use changes based on Land Change Modeler and attribution of changes in the water balance of Ganga basin to land use change using the SWAT model. *Sci. Total Environ.* 644, 503–519. <https://doi.org/10.1016/j.scitotenv.2018.07.017>
- Andrade, B.D.S., Singh, C.L., Santos, J.A., Gonçalves, V.V.C., Siqueira-Souza, F.K., Freitas, C.E. de C., 2019. Efeitos das mudanças climáticas sobre as comunidades de peixes na Bacia Amazônica. *Rev. Ciências da Soc.* 2, 107. <https://doi.org/10.30810/rcs.v2i4.905>

- Andrade, M.A., de Mello, C.R., Beskow, S., 2012. Hydrological simulation in a watershed with predominance of Oxisol in the upper Grande river region, MG - Brazil. *Rev. Bras. Eng. Agric. e Ambient.* 17, 69–76. <https://doi.org/10.1590/S1415-43662013000100010>
- Arnold, J.G., Moriasi, D.N., Gassman, P.W., Abbaspour, K.C., White, M.J., Srinivasan, R., Santhi, C., Harmel, R.D., Van Griensven, A., Liew, M W Van, Kannan, N., Jha, M.K., Harmel, D., Member, A., Liew, Michael W Van, Arnold, J.-F.G., 2012. SWAT: model use, calibration, and validation. *Trans. ASABE* 55, 1491–1508.
- Barata, M.M.L., Bader, D.A., Dereczynski, C., *et al.* 2020. Use of Climate Change Projections for Resilience Planning in Rio de Janeiro, Brazil. *Front Sustain Cities.* 2, 1-10. <https://doi.org/10.3389/FRSC.2020.00028>
- Baptista, A.C., 2009. Assessment of susceptibility to mass movements, erosion and runoff in Nova Friburgo, RJ. Viçosa Minas Gerais. Universidade Federal de Viçosa. URL <https://www.locus.ufv.br/handle/123456789/820> (accessed 6.15.20).
- Bieger, K., Hörmann, G., Fohrer, N., 2013. The impact of land use change in the Xiangxi Catchment (China) on water balance and sediment transport. *Reg. Environ. Chang.* 15, 485–498. <https://doi.org/10.1007/s10113-013-0429-3>
- Boylan, M., Suchman, K., Vigdorchik, J., Slover, J. & Bosco, J. (2018) Technology-Assisted Hip and Knee Arthroplasties: An Analysis of Utilization Trends. *J. Arthroplasty*, 33, 1019–1023. doi:10.1016/j.arth.2017.11.033
- Britto, A.L., Maiello, A., Quintslr, S., 2018. Water supply system in the Rio de Janeiro Metropolitan Region: Open issues, contradictions, and challenges for water access in an emerging megacity. *J. Hydrol.* <https://doi.org/10.1016/j.jhydrol.2018.02.045>
- Cunha, D.A., Coelho, A.B., Féres, J.G., Braga, M.J., 2014. Effects of climate change on the adoption of irrigation in Brazil [in Portuguese]. *Acta Sci. - Agron.* 36, 1–9. <https://doi.org/10.4025/actasciagron.v36i1.15375>
- Eastman, J.R., 2012. IDRISI selva manual version 17. Worcester, Mass. Clark Labs, Clark University, USA, pp. 322.
- Eastman, J.R., Toledano, J. 2018. A Short Presentation of the Land Change Modeler (LCM). 499–505. https://doi.org/10.1007/978-3-319-60801-3_36
- FAO, 2011. The state of the world's land and water resources for food and agriculture managing systems at risk.
- Freitas, C.M., de Carvalho, M.L., Ximenes, E.F., Arraes, E.F., Gomes, J.O., 2012. Vulnerabilidade socioambiental, redução de riscos de desastres e construção da resiliência - lições do terremoto no Haiti e das chuvas fortes na região serrana, Brasil. *Cienc. e Saude Coletiva* 17, 1577–1586. <https://doi.org/10.1590/S1413-81232012000600021>
- Fukunaga, D.C., Cecílio, R.A., Zanetti, S.S., Oliveira, L.T., Caiado, M.A.C., 2015. Application of the SWAT hydrologic model to a tropical watershed at Brazil. *Catena* 125, 206–213. <https://doi.org/10.1016/j.catena.2014.10.032>
- Gabiri, G., Leemhuis, C., Diekkrüger, B., Näschen, K., Steinbach, S., Thonfeld, F., 2019. Modelling the impact of land use management on water resources in a tropical inland valley catchment of central Uganda, East Africa. *Sci. Total Environ.* 653, 1052–1066. <https://doi.org/10.1016/j.scitotenv.2018.10.430>
- IBGE, 2017. IBGE Cities - Panorama [WWW Document]. URL <https://cidades.ibge.gov.br/brasil/rj/nova-friburgo/panorama> (accessed 6.15.20).
- INEA, 2018. Rio de Janeiro public supply water atlas - subsidies for territorial organizing and planning [WWW Document]. URL http://www.inea.rj.gov.br/wp-content/uploads/2019/01/Livro_Atlas-dos-Mananciais-de-Abastecimento-do-Estado-do-Rio-de-Janeiro.pdf (accessed 6.15.20).
- INEA, 2020. Licenses issued [WWW Document]. URL <http://200.20.53.7/listalicencas/views/pages/lista.aspx> (accessed 6.15.20).
- INEA, 2014. Elaboration of the state plan for water resources of the state of rio de janeiro R8-B - Demand scenarios and water balance [WWW Document]. URL <http://www.agevap.org.br/downloads/Relatorio-Cenarios-Demandas.pdf> (accessed 6.15.20)
- INMET, 2021. Brazilian climatological standards 1981-2010. [WWW Document]. URL https://clima.inmet.gov.br/NormaisClimatologicas/1961-1990/precipitacao_acumulada_mensal_anual (accessed 09.25.21)

- Jodar-Abellan, A., Valdes-Abellan, J., Pla, C., Gomariz-Castillo, F., 2019. Impact of land use changes on flash flood prediction using a sub-daily SWAT model in five Mediterranean ungauged watersheds (SE Spain). *Sci. Total Environ.* 657, 1578–1591. <https://doi.org/10.1016/j.scitotenv.2018.12.034>
- Joly, C.A., Scarano, F.R., Bustamante, M., Gadda, T.M.C., Metzger, J.P.W., Seixas, C.S., Ometto, J.P.H.B., Pires, A.P.F., Boesing, A.L., Sousa, F.D.R., Quintão, J.M.B., Gonçalves, L.R., Padgurschi, M. de C.G., de Aquino, M.F.D.S., de Castro, P.F.D., Dos Santos, I.L., 2019. Brazilian assessment on biodiversity and ecosystem services: Summary for policy makers. *Biota Neotrop.* 19. <https://doi.org/10.1590/1676-0611-bn-2019-0865>
- Joorabian Shooshtari, S., Shayesteh, K., Gholamalifard, M., Azari, M., Serrano-Notivoli, R., López-Moreno, J.I., 2017. Impacts of future land cover and climate change on the water balance in northern Iran. *Hydrol. Sci. J.* 62, 2655–2673. <https://doi.org/10.1080/02626667.2017.1403028>
- Kafy, A-Al, Hasan, M.M., Faisal, A.-A.-, Islam, M., Rahman, M.S., 2020. Modelling future land use land cover changes and their impacts on land surface temperatures in Rajshahi, Bangladesh. *Remote Sens. Appl. Soc. Environ.* 18, 100314. <https://doi.org/10.1016/j.rsase.2020.100314>
- Krysanova, V., White, M., 2015. Advances in water resources assessment with SWAT—an overview. *Hydrol. Sci. J.* 60, 1–13. <https://doi.org/10.1080/02626667.2015.1029482>
- Kumar, N., Tischbein, B., Beg, M.K., 2019. Multiple trend analysis of rainfall and temperature for a monsoon-dominated catchment in India. *Meteorol. Atmos. Phys.* 131, 1019–1033. <https://doi.org/10.1007/s00703-018-0617-2>
- Lin, Y.-P., Chu, H.-J., Wu, C.-F., Verburg, P.H., 2011. Predictive ability of logistic regression, auto-logistic regression and neural network models in empirical land-use change modeling – a case study. *Int. J. Geogr. Inf. Sci.* 25, 65–87. <https://doi.org/10.1080/13658811003752332>
- Lotz, T., Opp, C., He, X., 2018. Factors of runoff generation in the Dongting Lake basin based on a SWAT model and implications of recent land cover change. *Quat. Int.* 475, 54–62. <https://doi.org/10.1016/j.quaint.2017.03.057>
- Magalhães I.B., Pereira A.S.A.P., Calijuri M.L, *et al.* 2020. Brazilian Cerrado and Soy moratorium: Effects on bi-ome preservation and consequences on grain production. *Land use policy* 99:105030. <https://doi.org/10.1016/J.LAN-DUSEPOL.2020.105030>
- Magrin, G.O., Marengo, J.A., Boulanger, J.-P., *et al.* 2014. 27 Central and South America Coordinating Lead Authors: Lead Authors: Contributing Authors: Review Editors: to the Fifth Assessment Report of the Intergovernmental Panel on Climate Change.
- Mallett, S., Halligan, S., Matthew Thompson, G.P., Collins, G.S., Altman, D.G., 2012. Interpreting diagnostic accuracy studies for patient care. *BMJ.* <https://doi.org/10.1136/bmj.e3999>
- Mandrekar, J.N. 2010. Receiver Operating Characteristic Curve in Diagnostic Test Assessment. *J Thorac Oncol* 5:1315–1316. <https://doi.org/10.1097/JTO.0B013E3181EC173D>
- MapBiomass, 2018. MapBiomass - Annual Coverage and Land Use Mapping Project in Brazil [WWW Document]. URL <http://plataforma.mapbiomas.org/map> (accessed 12.17.19).
- Marhaento, H., Booij, M.J., Hoekstra, A.Y., 2018. Hydrological response to future land-use change and climate change in a tropical catchment. *Hydrol. Sci. J.* 63, 1368–1385. <https://doi.org/10.1080/02626667.2018.1511054>
- Marques, A., Martins, I.S., Kastner, T., Plutzer, C., Theurl, M.C., Eisenmenger, N., Huijbregts, M.A.J., Wood, R., Stadler, K., Bruckner, M., Canelas, J., Hilbers, J.P., Tukker, A., Erb, K., Pereira, H.M., 2019. Increasing impacts of land use on biodiversity and carbon sequestration driven by population and economic growth. *Nat. Ecol. Evol.* 3, 628–637. <https://doi.org/10.1038/s41559-019-0824-3>
- Marques JF, Alves MB, Silveira CF, *et al.* (2021) Fires dynamics in the Pantanal: Impacts of anthropogenic activities and climate change. *J Environ Manage* 299:113586. doi: 10.1016/j.jenvman.2021.113586
- Mas, J.F., Filho, B.S., Pontius, R.G., *et al.* 2013. A Suite of Tools for ROC Analysis of Spatial Models. *ISPRS Int J Geo-Information* 2013, Vol 2, Pages 869–887 2:869–887. <https://doi.org/10.3390/IJGI2030869>

- Mas, J.F., Kolb, M., Paegelow, M., Camacho Olmedo, M.T., Houet, T., 2014. Inductive pattern-based land use/cover change models: A comparison of four software packages. *Environ. Model. Softw.* 51, 94–111. <https://doi.org/10.1016/j.envsoft.2013.09.010>
- Mello, C.R., Lima, J.M., Da Silva, A.M., 2007. Surface runoff and peak discharge simulation in ephemeral watershed. *Rev. Bras. Eng. Agric. e Ambient.* 11, 410–419. <https://doi.org/10.1590/S1415-43662007000400011>
- Mendonça, L.A.R., Vásquez, M.A.N., Feitosa, J.V., *et al.* 2009. Evaluation of the infiltration capacity of soils under ferent types of management. *Eng Sanit e Ambient* 14:89–98. <https://doi.org/10.1590/S1413-41522009000100010>
- Moraes, T.C., dos Santos, V.J., Calijuri, M.L., Torres, F.T.P., 2018. Effects on runoff caused by changes in land cover in a Brazilian southeast basin: evaluation by HEC-HMS and HEC-GEOHMS. *Environ. Earth Sci.* 77, 1–14. <https://doi.org/10.1007/s12665-018-7430-6>
- Moriasi, D.N., Arnold, J.G., Liew, M.W. Van, Bingner, R.L., Harmel, R.D., Veith, T.L., 2007. model evaluation guidelines for systematic quantification of accuracy in watershed simulations, *Transactions of the ASABE*.
- Narsimlu, B., Gosain, A.K., Chahar, B.R., Singh, S.K., Srivastava, P.K., 2015. SWAT Model Calibration and Uncertainty Analysis for Streamflow Prediction in the Kunwari River Basin, India, Using Sequential Uncertainty Fitting. *Environ. Process.* 2, 79–95. <https://doi.org/10.1007/s40710-015-0064-8>
- Natkhin, M., Dietrich, O., Schäfer, M.P., Lischeid, G., 2015. The effects of climate and changing land use on the discharge regime of a small catchment in Tanzania. *Reg. Environ. Chang.* 15, 1269–1280. <https://doi.org/10.1007/s10113-013-0462-2>
- Olmedo, M.T.C., Pontius, R.G., Paegelow, M., Mas, J.F., 2015. Comparison of simulation models in terms of quantity and allocation of land change. *Environ. Model. Softw.* 69, 214–221. <https://doi.org/10.1016/j.envsoft.2015.03.003>
- Pinheiro, E.P., Marques, E.E., Lolis, S.F., 2019. Monitoramento de empreendimentos hidrelétricos na bacia do rio Tocantins, Brasil: o que aprendemos com os estudos das macrófitas aquáticas. *Biotemas* 32, 11–22. <https://doi.org/10.5007/2175-7925.2019v32n3p11>
- Piniewski, M., Bieger, K., Mehdi, B., 2019. Advancements in Soil and Water Assessment Tool (SWAT) for ecohydrological modelling and application. *Ecohydrol. Hydrobiol.* <https://doi.org/10.1016/j.ecohyd.2019.05.001>
- Pontes, L.M., Viola, M.R., Silva, M.L.N., Bispo, D.F.A., Curi, N., Pontes, L.M., Viola, M.R., Silva, M.L.N., Bispo, D.F.A., Curi, N., 2016. Hydrological Modeling of Tributaries of Cantareira System, Southeast Brazil, with the Swat Model. *Eng. Agrícola* 36, 1037–1049. <https://doi.org/10.1590/1809-4430-eng.agric.v36n6p1037-1049/2016>
- Saha, P.P., Zeleke, K., Hafeez, M., 2019. Impacts of land use and climate change on streamflow and water balance of two sub-catchments of the Murrumbidgee River in South Eastern Australia, in: *Extreme Hydrology and Climate Variability: Monitoring, Modelling, Adaptation and Mitigation*. Elsevier, pp. 175–190. <https://doi.org/10.1016/B978-0-12-815998-9.00015-4>
- Sao, D., Kato, T., Tu, L.H., *et al.* 2020. Evaluation of Different Objective Functions Used in the SUFI-2 Calibration Process of SWAT-CUP on Water Balance Analysis: A Case Study of the Pursat River Basin, Cambodia. *Water* 12, 2901. <https://doi.org/10.3390/W12102901>
- Sangermano, F., Toledano, J., Eastman, R., 2012. Land cover change in the Bolivian Amazon and its implications for REDD+ and endemic biodiversity. *Landsc. Ecol.* 27, 571–584. <https://doi.org/10.1007/s10980-012-9710-y>
- Shade, C., Kremer, P. 2019. Predicting Land Use Changes in Philadelphia Following Green Infrastructure Policies 8, 28. <https://doi.org/10.3390/LAND8020028>
- Van Cauwenbergh, N., Ballester Ciuró, A., Ahlers, R., 2018. Participatory processes and support tools for planning in complex dynamic environments: A case study on web-GIS based participatory water resources planning in Almeria, Spain. *Ecol. Soc.* 23. <https://doi.org/10.5751/ES-09987-230202>
- Wohl, E., Barros, A., Brunzell, N., Chappell, N.A., Coe, M., Giambelluca, T., Goldsmith, S., Harmon, R., Hendrickx, J.M.H., Juvik, J., McDonnell, J., Ogden, F., 2012. The hydrology of the humid tropics. *Nat. Clim. Chang.* <https://doi.org/10.1038/nclimate1556>

Wu, L., Liu, X., Ma, X., 2018. Prediction of land-use change and its driving forces in an ecological restoration watershed of the Loess hilly region. *Environ. Earth Sci.* 77. <https://doi.org/10.1007/s12665-018-7413-7>

Zaroni, M.J., Santos, H.G. dos, 2018. Solos Tropicais - Cambissolos [WWW Document]. URL https://www.agencia.cnptia.embrapa.br/gestor/solos_tropicais/arvore/CONTAG01_8_2212200611538.html (accessed 12.19.19).

Zhang, H., Wang, B., Liu, D.L., Zhang, M., Leslie, L.M., Yu, Q., 2020. Using an improved SWAT model to simulate hydrological responses to land use change: A case study of a catchment in tropical Australia. *J. Hydrol.* 585, 124822. <https://doi.org/10.1016/j.jhydrol.2020.124822>

Zhang, L., Nan, Z., Yu, W., Zhao, Y., Xu, Y., 2018. Comparison of baseline period choices for separating climate and land use/land cover change impacts on watershed hydrology using distributed hydrological models. *Sci. Total Environ.* 622–623, 1016–1028. <https://doi.org/10.1016/j.scitotenv.2017.12.055>

Zhou, J., He, D., Xie, Y., Liu, Y., Yang, Y., Sheng, H., ... Zou, R. (2015). Integrated SWAT model and statistical downscaling for estimating streamflow response to climate change in the Lake Dianchi watershed, China. *Stochastic Environmental Research and Risk Assessment*, 29(4), 1193–1210. doi:10.1007/s00477-015-1037-1